March 2019

A Multiline Anchor Concept for Floating Offshore Wind Turbines

Casey Fontana

A MULTILINE ANCHOR CONCEPT FOR FLOATING OFFSHORE WIND TURBINES

A Dissertation Presented

by

CASEY M. FONTANA

Submitted to the Graduate School of the
University of Massachusetts Amherst in partial fulfillment
of the requirements for the degree of

DOCTOR OF PHILOSOPHY

February 2019

Civil Engineering

A MULTILINE ANCHOR CONCEPT FOR FLOATING OFFSHORE WIND TURBINES

A Dissertation Presented

by

CASEY M. FONTANA

Approved as to style and content by:

_____
Sanjay R. Arwade, Co-Chair

_____
Don J. DeGroot, Co-Chair

_____
Matthew A. Lackner, Member

_____
Richard N Palmer, Department Head
Civil and Environmental Engineering

DEDICATION

To my endlessly supportive parents, Mark and Tina Fontana,

who have been fervently cheering for me since my first set of Lincoln Logs

To my loving and patient boyfriend, Philip Demers,

who has cared for me during the ups and downs of graduate school

And to all of my brilliant friends and colleagues who have helped me along the way

ACKNOWLEDGMENTS

This work has been generously funded by U.S National Science Foundation grants IGERT-1068864, CMMI-1463273, CMMI-1463431, and CMMI-1462600, and the Massachusetts Clean Energy Center. The UMass IGERT program was immensely accommodating throughout this work, and the other IGERT fellows offered extensive and valuable collaboration.

This work would not have been possible without the support and guidance of my research team, namely my primary academic advisors Professor Sanjay Arwade and Professor Don DeGroot. The final member of my doctoral committee was Professor Matthew Lackner, who provided significant support and guidance as well. Additional advising was provided by Andrew Myers, Chi Qiao, Andrew Summerfield, and Vahid Valamanesh of Northeastern University, Melissa Landon of the University of Maine, and Charles Aubeny and Brian Diaz of Texas A&M University. Industry guidance by Senol Ozmutlu and Leo Bello of Vryhof Anchors was also of great value to the work on this novel concept.

Lastly, a great deal of support, problem solving, essential insight on this project came from my incredibly talented UMass offshore wind colleagues - Wystan Carswell, Kai Wei, Spencer Hallowell, Ning Luo.

ABSTRACT

A MULTILINE ANCHOR CONCEPT FOR FLOATING OFFSHORE WIND TURBINES

February, 2019

CASEY FONTANA, B.S., THE COLLEGE OF NEW JERSY

Ph.D., UNIVERSITY OF MASSACHUSETTS AMHERST

Directed by: Professor Sanjay R. Arwade and Don J. DeGroot

Floating offshore wind energy is holds great potential for the essential industry of renewable energy, but the high capital cost associated with the substructure of a floating offshore wind turbine (FOWT) is a significant barrier in development. In efforts to increase FOWT substructure efficiency and effectively reduce its cost, this thesis investigates a novel multiline anchor concept, in which FOWTs share anchors instead of being moored separately. The goal of this work is to evaluate the force dynamics, design, and potential cost reduction of the system. Anchor forces are simulated using the NREL 5 MW reference turbine and OC4-DeepCwind semisubmersible platform, and multiline anchor force is computed as the vector sum of the contributing mooring line tensions.

The use of a multiline anchor configuration in large scale farms would result in reductions in the number of anchors approaching 67% and 83% for 3-line and 6-line anchor systems, respectively. Due to the cancellation and addition of the different contributing line tension components, maximum anchor force is up to 16% smaller in 3-line anchors systems and up to 20% larger in 6-line anchors systems, compared to the conventional single-line anchor. Direction of the multiline anchor force generally aligns with the wind, wave, and current (WWC) direction, and direction reversal within a single force cycle occurs in extreme load cases.

Spatial coherence of the wave fields is considered due the interconnectedness of the system, revealing that spatial correlation of the waves decays to insignificant levels within several hundred meters. Given that FOWT spacing is greater than 500 m, it is asserted that the assumption of independent wave fields at different FOWT locations is sufficient for obtaining multiline anchor load characterizations.

The site characteristics of the first and only floating offshore wind farm as of writing this thesis are used to evaluate the multiline anchor concept in the context of a real farm. Very little difference in the mooring layouts and anchor weights exists between the installed single-line anchor system and the novel multiline anchor system, but the multiline system results in a 40% reduction in the number of anchors, and in effect a 41% reduction in the total anchor weight required.

A capital cost analysis of the mooring lines, anchors, anchor installation, and geotechnical site investigation is carried out over a range of water depths, turbine spacings, and farm sizes. This analysis reveals that the multiline concept may result in cost reductions of 8-16% for a 100-turbine wind farm, and that mooring systems configuration with smaller ratios of depth to spacing achieve larger reductions in the combined line & anchor cost.

TABLE OF CONTENTS

Page

LIST OF TABLES

Table Page

LIST OF FIGURES

CHAPTER 1

INTRODUCTION

1.1 Background & Motivation

The development of clean, renewable energy is an essential task in the face of climate change, and offshore wind energy is key player in the fight to reduce damaging greenhouse gas emissions. The growth of the offshore wind industry has been accelerating since its start in the early 1990s – 3.3 GW of offshore wind capacity was commissioned globally in 2017, resulting in a cumulative installed global capacity of 16.3 GW. The United States now has a project pipeline of 25.5 GW of offshore wind, and developers have announced that roughly 2 GW of new offshore wind capacity is expected to be operational by 2023 [1]. This growth in the U.S. is incentivized by aggressive offshore wind goals set forth by many east coast states. New Jersey increased the state's 2030 offshore wind commitment from 1,100 MW to 3,500 MW [2], Massachusetts has mandated the procurement of 1,600 MW of offshore wind by 2027 [3], Rhode Island aims to add 1,000 MW of renewables by 2020 [4], and New York has identified a 2,400-MW offshore wind target to reach their goal of 50% renewable energy by 2030 [5].

As the offshore wind industry continues its growth, several trends have developed that guide the industry towards floating technology. These trends include larger turbine size as shown in Figure 1, and deeper water installation and further offshore sites as shown in Figure 2.

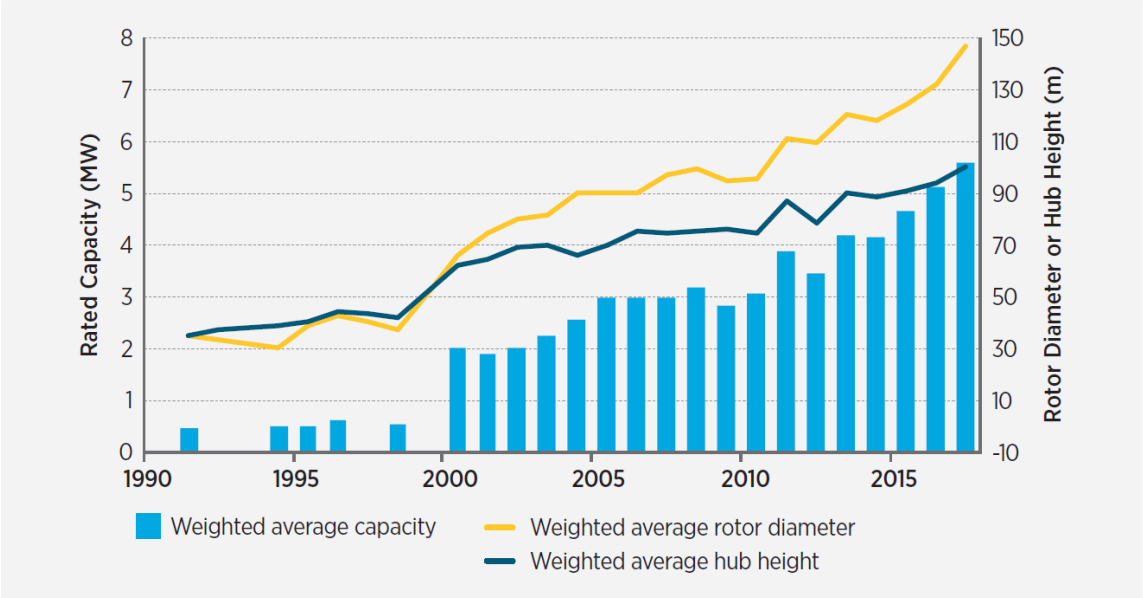

Figure 1: Average turbine size, rotor size, and hub height for commercial offshore wind plants [6]

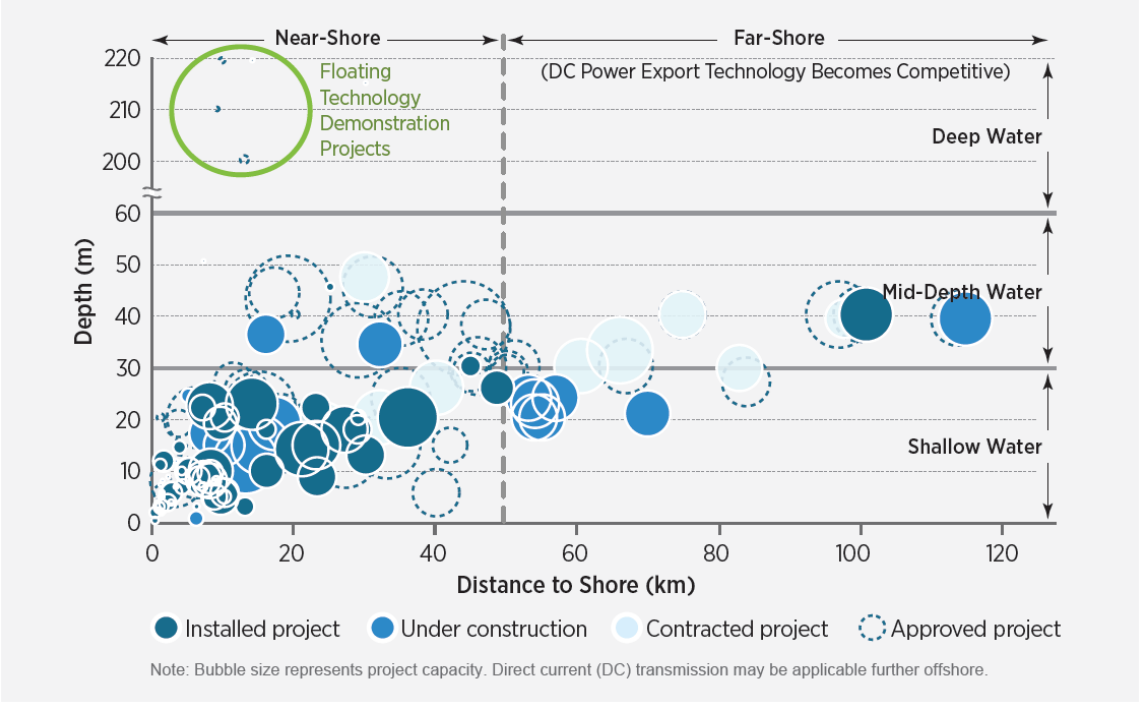

Figure 2: Characteristics of offshore wind projects in Europe, 2013 [6]

Many of these new potential areas of offshore wind development offer access to higher, more consistent wind resources, and allow for increased power production. These

further offshore locations also eliminate the issue of coastline aesthetics that has proved a significant barrier of offshore wind development, namely in the proposed and failed Cape Wind project [7]. This movement towards floating wind energy in these new sites is further displayed in terms of the announced global project pipeline, which reveals increasing penetration for floating substructures, as shown in Figure 3.

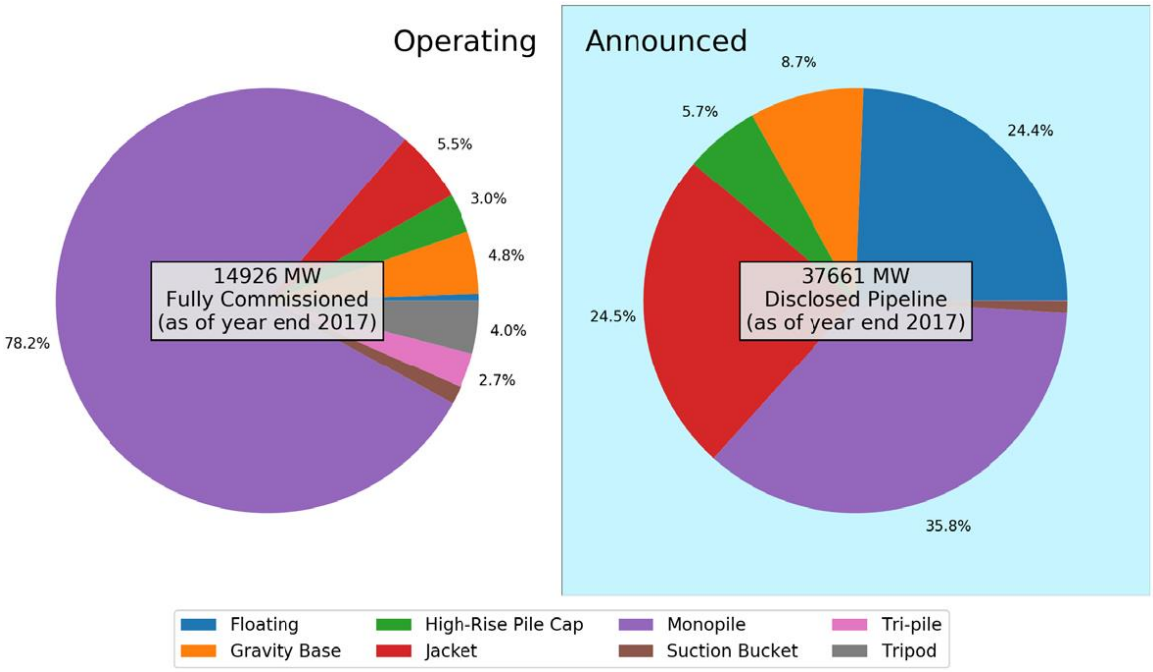

Figure 3: Global offshore wind substructure market share by type [1]

The trend towards deeper waters is highly compatible with the development of floating wind turbines, as fixed-bottom support structures are not economically feasible in water depths exceeding 60 m [8]. Floating wind technology is critical for accomplishing the aforementioned offshore wind energy goals set forth by the U.S., given that 59% of the U.S. technical wind resource area is in deep water [9], as shown in Figure 4.

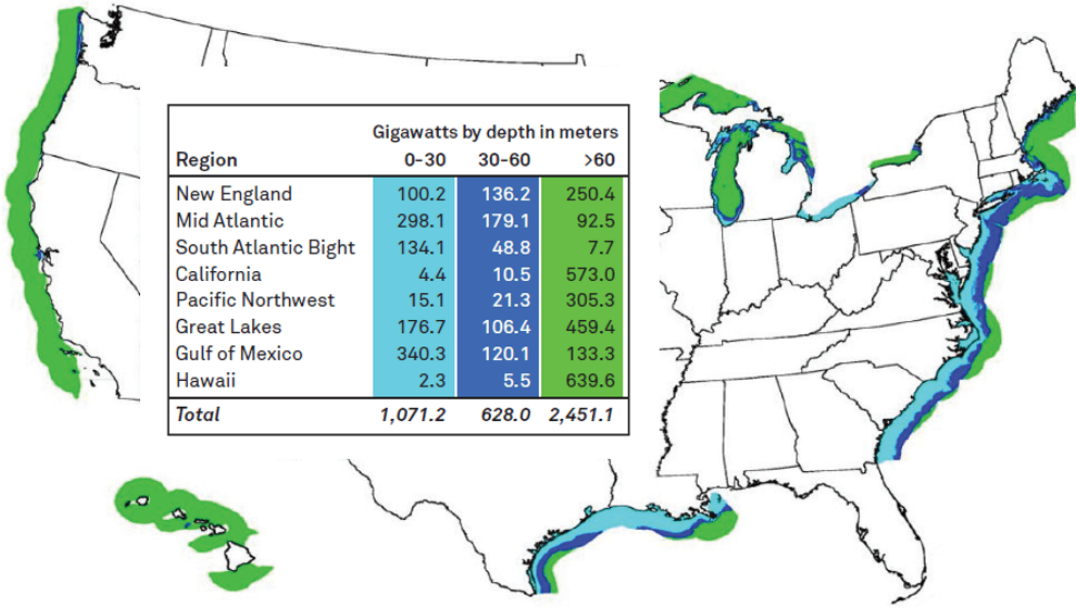

Region	Gigawatts by depth in meters 0-30	30-60	>60
New England	100.2	136.2	250.4
Mid Atlantic	298.1	179.1	92.5
South Atlantic Bight	134.1	48.8	7.7
California	4.4	10.5	573.0
Pacific Northwest	15.1	21.3	305.3
Great Lakes	176.7	106.4	459.4
Gulf of Mexico	340.3	120.1	133.3
Hawaii	2.3	5.5	639.6
Total	*1,071.2*	*628.0*	*2,451.1*

Figure 4: U.S. offshore wind capacity by water depth [9]

The trend towards fewer, larger turbines in a wind farm achieves lower installation and balance-of-system costs, higher capacity factors, and reduced operational expenditures [8]. As larger, heavier turbines are utilized, a limit will likely be reached where fixed-bottom structures cannot adequately support the turbines due to adequate stiffness requirements and drivability limits, while floating substructures are free of such a limitation on turbine size [10]. Larger turbines are additionally a good fit for floating turbines in their ability to withstand high wind-speeds and the associated larger rotor thrust forces that will result [11].

Numerous floating wind projects continue to be investigated and tested. Equinor successfully installed its five-turbine spar-substructure 30-MW Hywind farm off the coast of Scotland in October 2017. Senvion and Principle Power LLC have partnered to test floating platforms capable of supporting offshore wind turbines that are 10 MW or larger in real-world conditions by 2021. Ideol's Floatgen 2-MW demonstration project

was assembled in port, towed to sea, moored to the seafloor at Le Croisic (France), and connected to the grid in May 2018. Additional projects can be seen in Figure 5 below.

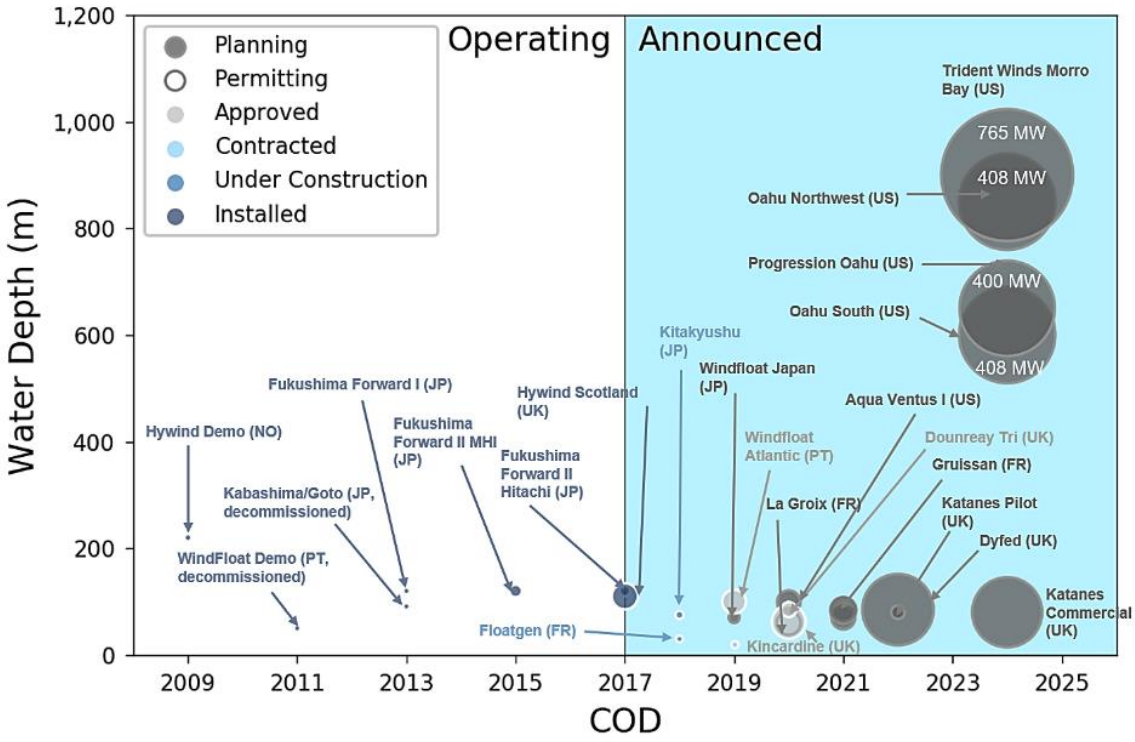

Figure 5: Developer-announced global floating offshore wind pipeline [1]

The support structure of a FOWT consists of a buoyant platform, anchors, and mooring lines extending between the two. Examples of FOWT platform types include buoyancy stabilized semi-submersibles, ballast-stabilized spar buoys, and mooring-stabilized tension leg platforms as shown in Figure 6. The TLP is not suitable to the multiline concept since the taut mooring lines are nearly vertical and could not reach common anchors with reasonable FOWT spacing maintained. While the catenary mooring systems of both semisubmersibles and spar buoys would be suitable for the multiline anchor concept, only the semisubmersible platform is studied in this work, for consistency. Mooring lines are typically composed of chain, wire rope, fiber rope, or a combination of these [12]. Anchor types include piles, suction caissons, drag embedded

anchors, and vertically loaded anchors, as shown in Figure 7 [13]. The design of these different components for a FOWT substructure is a complex function of water depth, environmental loading conditions, and seabed conditions, and other parameters.

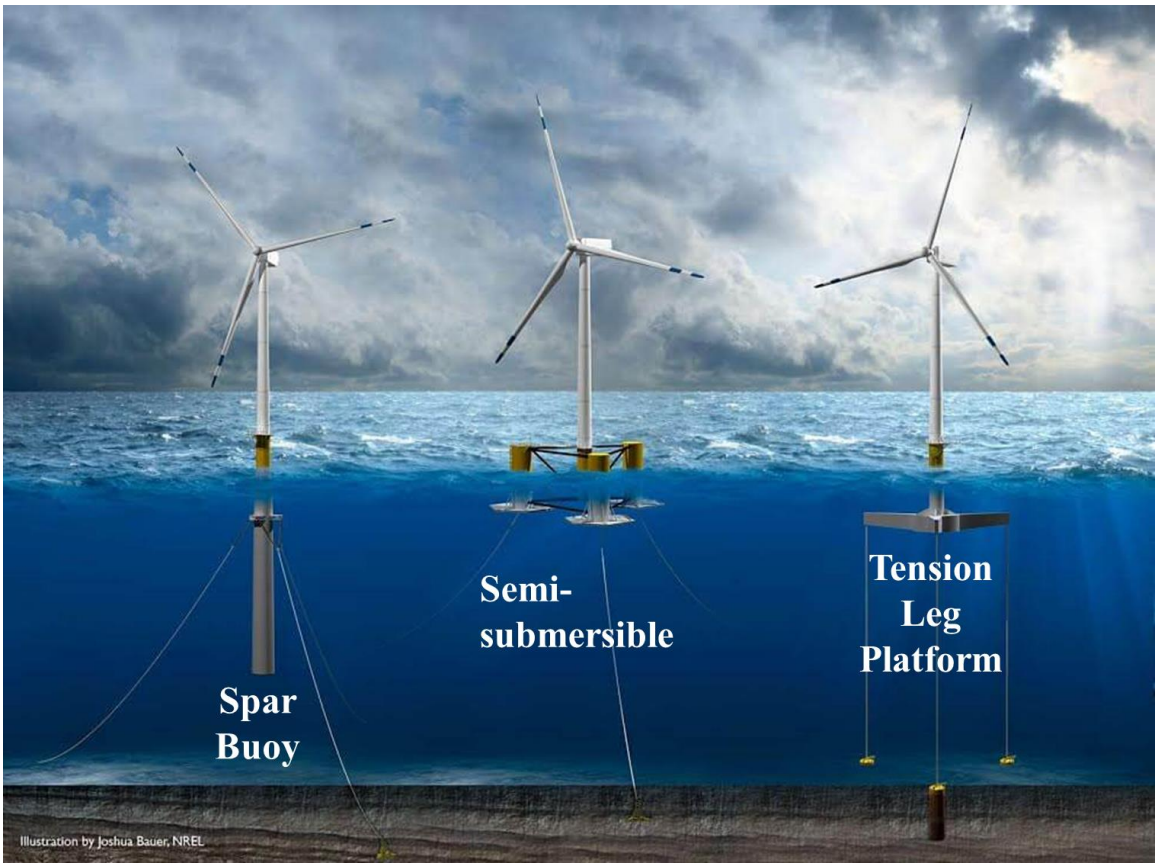

Figure 6: Floating platform types

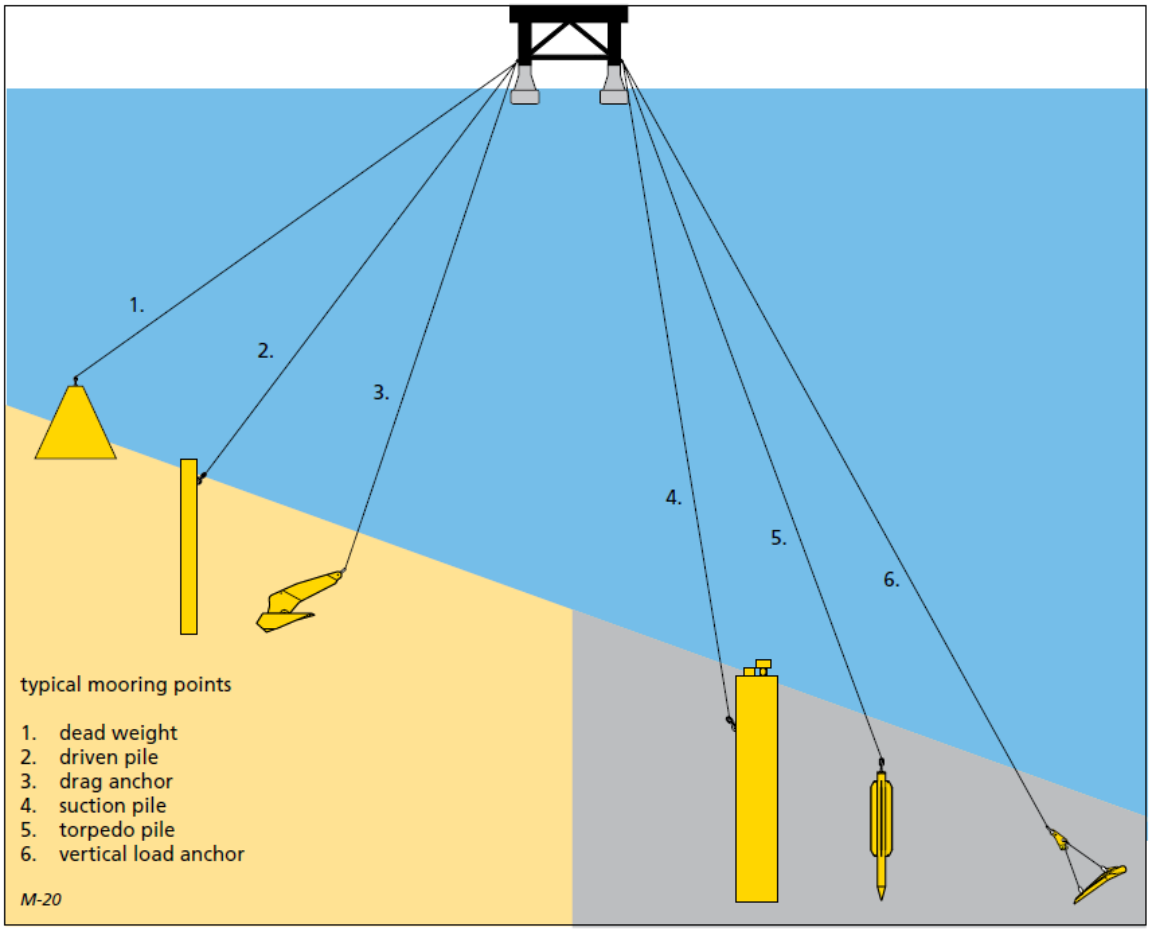

Figure 7: Offshore anchor types [13]

While the offshore wind industry's trend towards floating turbines is strong, there is still considerable optimization to be achieved for floating systems that support wind turbines, and significant barriers to FOWT development are still present. A primary obstacle in floating offshore wind development is the high capital cost associated with constructing the large platforms and mooring systems needed to support the turbines in deep water [14], and this high capital cost must be reduced if floating wind is to become cost competitive in the energy generation market. Figure 8 reveals that the substructure accounts for the largest portion of a floating wind turbine's capital cost, which is composed of the floating platform, mooring lines, and anchors.

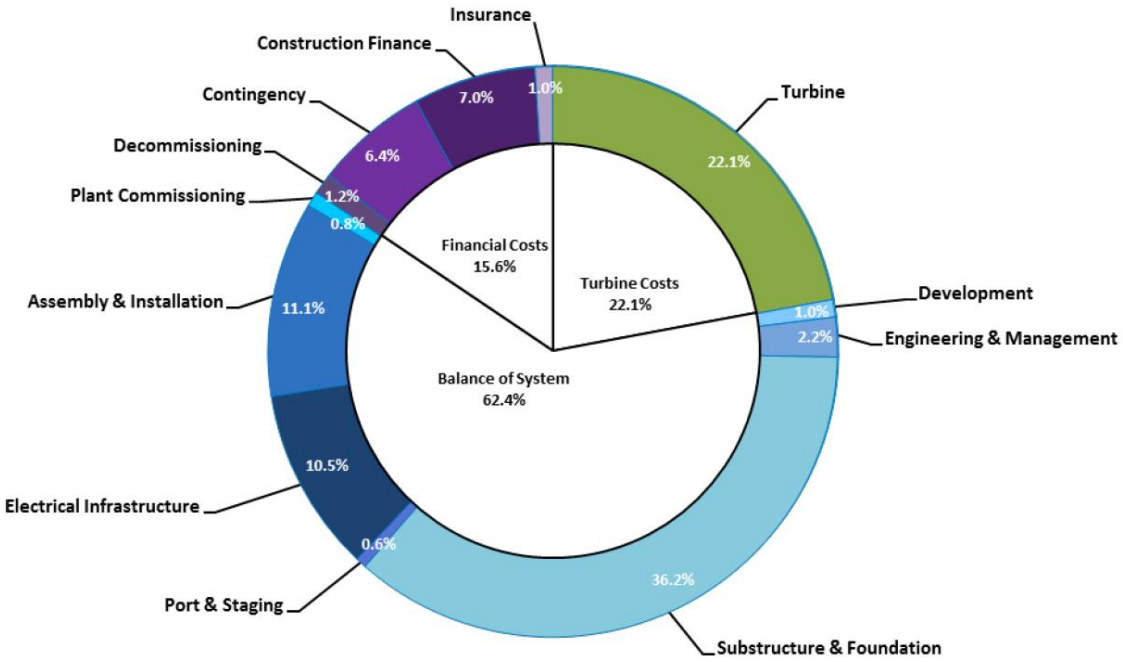

Figure 8: Breakdown of capital expenditures for the floating offshore reference wind plant project [15]

The magnitude of the support structure cost relative to the total cost encourages research in support structure efficiency, which motivates the multiline anchor concept analyzed in this thesis. In the conventional single-line anchor concepts of current installed and planned floating offshore projects, each FOWT is moored to the seafloor separately by at least 3 of its own single-line anchors. Therefore, the number of anchors required to moor a conventional single-line floating wind farm is at least 3 times the number of turbines. In the multiline concept, turbines are arranged such that they share anchors amongst each other, allowing for a smaller number of anchors required. This reduction in anchor points would result in less material, installation operations, and site investigations, and in effect an overall cost reduction of the anchor system.

1.2 Research Objectives and Methodology

Given that current floating technology in both the wind industry and the oil & gas industry only utilize conventional single-line anchor systems, this novel multiline anchor

concept must be thoroughly investigated. The overarching goal of this work is to evaluate the novel multiline anchoring concept for potential implementation in a real floating offshore wind farm, and to investigate all behaviors and characteristics of such a system that may be relevant in a design and development context. All research conducted in this thesis is in the numerical domain, though some experimental work on the topic has been completed by collaborators (see Section 1.4). Specific research objectives include:

1.) Determining realistic and feasible layouts of a floating offshore wind farm with multiline anchors, and assessing limits on the number of lines per anchor, water depth, and turbine spacing for these farms
2.) Finding a suitable method for modeling multiline anchor loading and determining the unique load characteristics of a multiline anchor, relative to conventional single-line anchor systems, under different environmental load conditions. Additionally, evaluating and designing anchor types for multiline anchor loading.
3.) Developing environmental load models that are suitable for numerical simulation of the interconnected multiline anchor system, and evaluating the importance of these models relative to those used in conventional single-line anchor systems
4.) Quantifying the cost benefit of the multiline system relative to single-line system, and determining how the cost benefit changes over a different spatial parameters.

1.3 Thesis Organization

This thesis consists of six chapters. A brief outline of each chapter is given below:

1.) Chapter 1 (current chapter) is an introduction to the thesis. The background & motivation, research objectives & methodology, thesis organization, and associated work are detailed.

2.) Chapter 2 is a Wind Energy journal paper that was published in 2018. This chapter examines the dynamics of the net multiline anchor force for a semisubmersible floating platform in two different layout geometries – a 3-line anchor and anchor 6-line. The magnitude, cyclic nature, and directionality of the multiline anchor force is analyzed over a range of environmental load cases.

3.) Chapter 3 is an Ocean Engineering journal paper that has been accepted with minor revisions. In this chapter, wave loading in the interconnected system is studied to determine if characteristics of the anchor loads are sensitive to spatial coherence of the wave field as it moves through an offshore floating wind farm, or whether an assumption of independence of the wave fields at different FOWT locations provides sufficiently accurate anchor load characterizations.

4.) Chapter 4, which is in the format of a journal paper to be submitted, uses the site characteristics of the first installed floating offshore wind farm to examine the multiline concept in the context of a real project.

5.) In Chapter 5, mooring systems are designed over a range of water depths and turbine spacings to evaluate the how the cost benefit of the multiline anchor

system relative to the single-line anchor system changes with respect to spatial parameters and farm size.

6.) Chapter 6 is a concluding chapter that summarizes findings of each chapter and recommendations for future work on the multiline anchor concept.

Please note: Since this thesis is formatted as a series of stand-alone papers, some repetition of certain aspects and considerations was inevitable, especially in the introductory sections of the chapters.

Furthermore, the appendix contains a Wind Engineering journal paper published in 2015, which details doctoral research on foundation damping in fixed-bottomed offshore wind turbines that was completed before the start of the multiline anchor project.

1.4 Literature Review and Associated Work

The concept of sharing mooring materials between turbines has been investigated by several other researchers. Goldschmidt et al [16] investigated the cost saving potential and dynamic properties of shared catenary mooring systems that reduce both the number of lines and number of anchors in floating offshore wind farms. The study supported the general feasibility of integrated mooring systems and concluded that cost reductions of up to 60% in mooring system and 8% in total system costs could be achieved. However, it also stated that displacements increase with the number of floaters, and cost savings diminish for larger numbers of turbines as the required diameters, lengths and costs of mooring chains increase. In another study of shared mooring systems, Connolly et al. [17] modelled pilot scale FOWT farms with shared mooring systems at different water depths. This study showed that shared mooring systems were effective at maintaining platform spacings and reducing the number of line and anchors required per FOWT, and

that significant cost savings over individually-moored farms are possible at water depths exceeding 400 m. Associated work by Hall et al. [18] dug deeper into the dynamics of these shared mooring systems for FOWTs via numerical modelling, revealing how surge displacements under wind and wave loading reflect the complex restoring properties of the shared mooring arrangement, and how shared mooring lines will see different excitation at either end. The work also concluded that shared mooring lines show a greater tendency for resonance due to the absence of seabed contact.

Other work devoted to substructure cost reduction has typically focused on minimizing the material consumption of the platform or mooring lines [19]–[21], as these components of the support structure account for a larger portion of the steel costs than the anchors [22]. However, the geotechnical site investigation and installation costs associated with the anchors are substantial, making it an important for focus point for cost reduction efforts. Furthermore, the results of this study on a multiline anchor concept are not limited to floating offshore wind - design of wave energy converters (WECs) may also benefit from a multiline anchor concept, as wave energy systems also seek to become cost competitive with other energy generation technologies.

The multiline anchor concept has been explored in several papers by the authors [23]–[31]. Hallowell et al. [27] assessed the reliability of a floating wind farm utilizing multiline anchors relative to a farm utilizing conventional single-line anchors, and found that the multiline system always had lower reliability and the potential for cascading failures. However, following work concluded that relatively small increases in the multiline anchor strength could allow the farm to achieve reliability values equal to the corresponding single-line system. Diaz et al. [29] examined different anchor types that

are potentially suitable as anchors for FOWTs, and assessed the potential for adapting these anchors to multiline systems. Anchor types examined included driven piles, dynamic piles, suction caissons, drag embedded anchors, vertically loaded anchors, pile driven plate anchors (PDPA), dynamically embedded plate anchors (DEPLA), and suction embedded plate anchors (SEPLA). While anchors with axisymmetric strength like piles and caissons are best-suited for the multidirectional loading in the multiline system, drag anchors with uniaxial capacity may be combined in a load-ring concept to be used in such a system.

The multiline system was also evaluated in an experimental setup. In Burns et al. [30], centrifuge modelling was used to assess the performance of suction caissons under orthogonal, double taut-line loading. Loading scenarios were chosen to provide insights into caisson behavior under single-line monotonic and cyclic loading, sustained loading of one line with cyclic loading of the orthogonal line, and simultaneous cyclic loading of both lines. The addition of a second orthogonal line resulted in increased capacity in the direction of monotonic loading to failure for all cyclic load combinations tested compared to the reference monotonic resistance. Additional numerical modeling by Chung et al [31] was particularly valuable for the simulation and modeling methods used in the remainder of this thesis, as it revealed that vector summation of contributing line tensions in the physical model was a suitable method for calculating the resultant load resistance of suction caisson with multiline loading.

CHAPTER 2

MULTILINE ANCHOR FORCE DYNAMICS IN FLOATING OFFSHORE WIND TURBINES

2.1 Introduction

The offshore wind industry has shown a steady trend towards larger turbines being installed in deeper water in locations further offshore [7]. These new potential areas of offshore wind development in deeper water offer access to higher, more consistent wind resources and remove the concern of shoreline aesthetics. The depth limitations of fixed-bottom offshore wind turbines (approximately 60 m) [8] motivates the development of floating concepts. Therefore floating offshore wind turbines (FOWTs) hold great potential as the next step in the offshore wind energy industry.

A primary obstacle in floating offshore wind development is the high capital cost associated with constructing the large platforms and mooring systems needed to support the turbines in deep water [14]. The magnitude of the support structure cost relative to the total cost encourages research in support structure efficiency, which motivates the multiline anchor concept analyzed in this thesis. In conventional concepts, each FOWT is moored separately by at least 3 single-line anchors. In the multiline concept (Figure 9), anchors are shared amongst FOWTs, allowing for a smaller number of anchors, site investigations, and installation operations. This chapter explores this novel multiline anchor concept in terms of layout geometries and characteristics of the anchor forces.

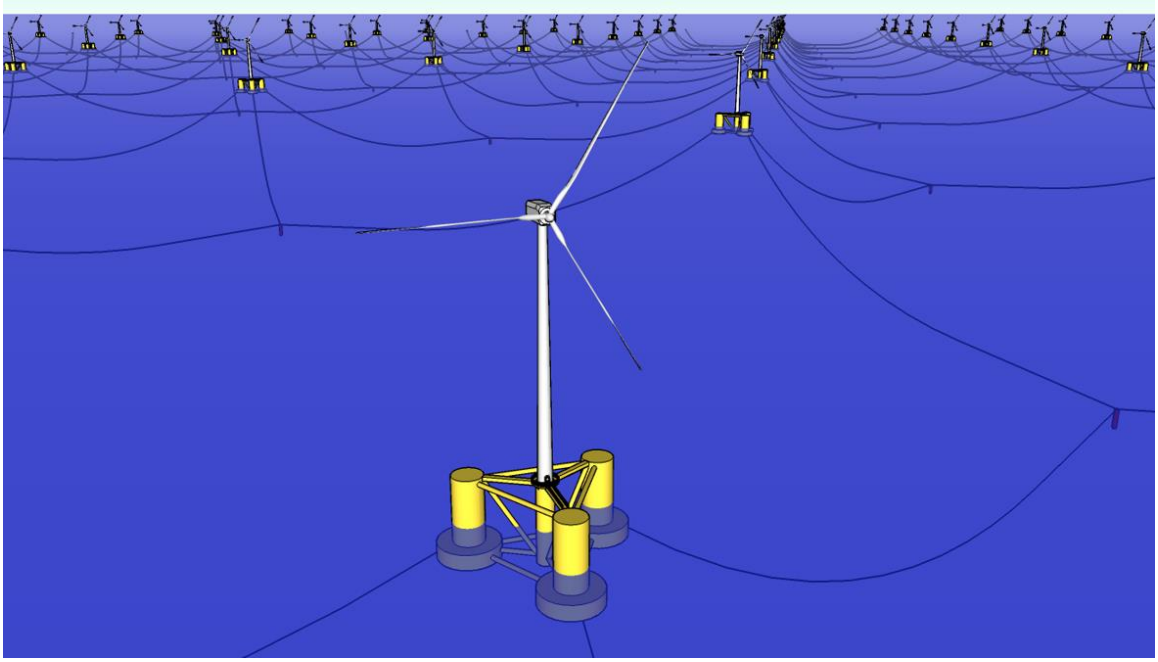

Figure 9: Floating offshore wind farm utilizing multiline anchor system

2.2 Multiline Anchor Layout Geometries

The first step in evaluating the multiline anchor concept is generation of the multiline anchor geometries. Both the number of anchors per FOWT and the number of FOWTs per anchor can be modified to create new multiline geometries. The single-line system used for comparison in this research has 3 anchors per FOWT and 1 FOWT per anchor. The use of 3 mooring lines and anchors per FOWT is most common amongst FOWT demonstration projects (Hywind, WindFloat, and Hybrid Spar) and development concepts—almost half of the projects that disclosed mooring system information in the Carbon Trust's 2015 FOWT Review utilize 3-line mooring systems, compared with others using as little as 1 line to as many as 8 lines [32]. The multiline geometries in Figure 10 are developed with the following characteristics:

1. For simplicity in a potential wind farm, only multiline geometries that contain a repeating unit cell are used. In such a repeating unit cell geometry, the turbines

connected to a multiline anchor are arranged concentrically around it, and the FOWT-FOWT, FOWT-anchor, and anchor-anchor spacing is consistent across a specific multiline geometry. As a result, the unit cells of a specific multiline anchor geometry can be easily multiplied to any farm size.

2. All systems evaluated—single-line anchor, 3-line anchor, and 6-line anchor—are nonredundant mooring systems because there are only 3 lines per FOWT.

3. The catenary mooring system design in terms of number of lines (3), radial distance from fairlead to anchor (797 m), each line length (835 m) and chain size (76 mm), is consistent across all systems evaluated (see Section 2.4.1, Turbine, Floating Platform, and Mooring System). The default 3-single-line system is patterned so that anchor locations become coincident, creating the multiline geometries (see Figure 10).

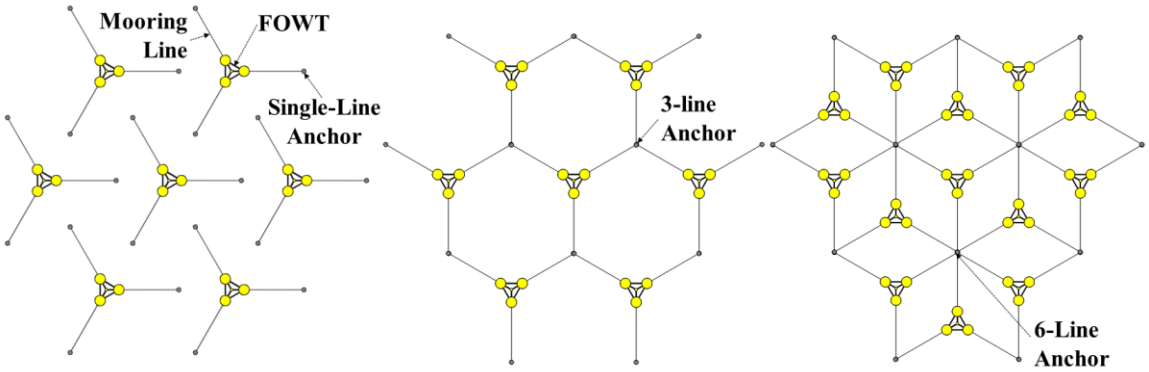

a.) b.) c.)

Figure 10: Layout of a.) single-line; b.) 3-line anchor; and c.) 6-line anchor systems

Table 1: Properties of the OC4-DeepCwind semisubmersible floating system [33]

Mooring System	Catenary
Mooring Line Type	Studless Chain
Extensional Stiffness	753.6 MN/m
Water Depth	200 m
Line Length	835.35 m
Chain Nominal Diameter	0.0766 m
Mass per Unit Length Chain	113.35 g/m

In terms of number of anchors, the most efficient geometry would be one that minimizes the ratio of anchors to turbines. More specifically, this would be a geometry that maximizes the number of FOWTs connected to each multiline anchor and minimizes the number of anchors used to moor each FOWT, subject to the constraint that an FOWT must be moored by at least 3 anchors ($n_{A/T} \geq 3$). Note that the number of anchors per turbine and number of turbines per anchor are not inverses of each other since, for example, a turbine may be moored by 3 anchors but each anchor may be connected to 6 turbines (see Figure 13). An approximation to the number of anchors required for a specified farm size is given by

$$\boldsymbol{N_A = N_T \times \frac{n_{A/T}}{n_{T/A}}} \qquad \textbf{(1)}$$

where N_A is the total number of anchors required, N_T is the total number of FOWTs, $n_{A/T}$ is the number of anchors connected to each FOWT, and $n_{T/A}$ is the number of FOWTs connected to each anchor. The ratio of $n_{A/T}$ to $n_{T/A}$ can be thought of as a measure of the aforementioned efficiency in terms of number of anchors. This relationship neglects perimeter effects in which the anchors around the perimeter of the farm are connected to less FOWTs than the farm's overall $n_{T/A}$ value. The magnitude of this perimeter effect varies by multiline geometry and wind farm size. Perimeter effects become negligible for

very large wind farms. Figure 11 presents the total number of anchors required relative to farm size for each geometry.

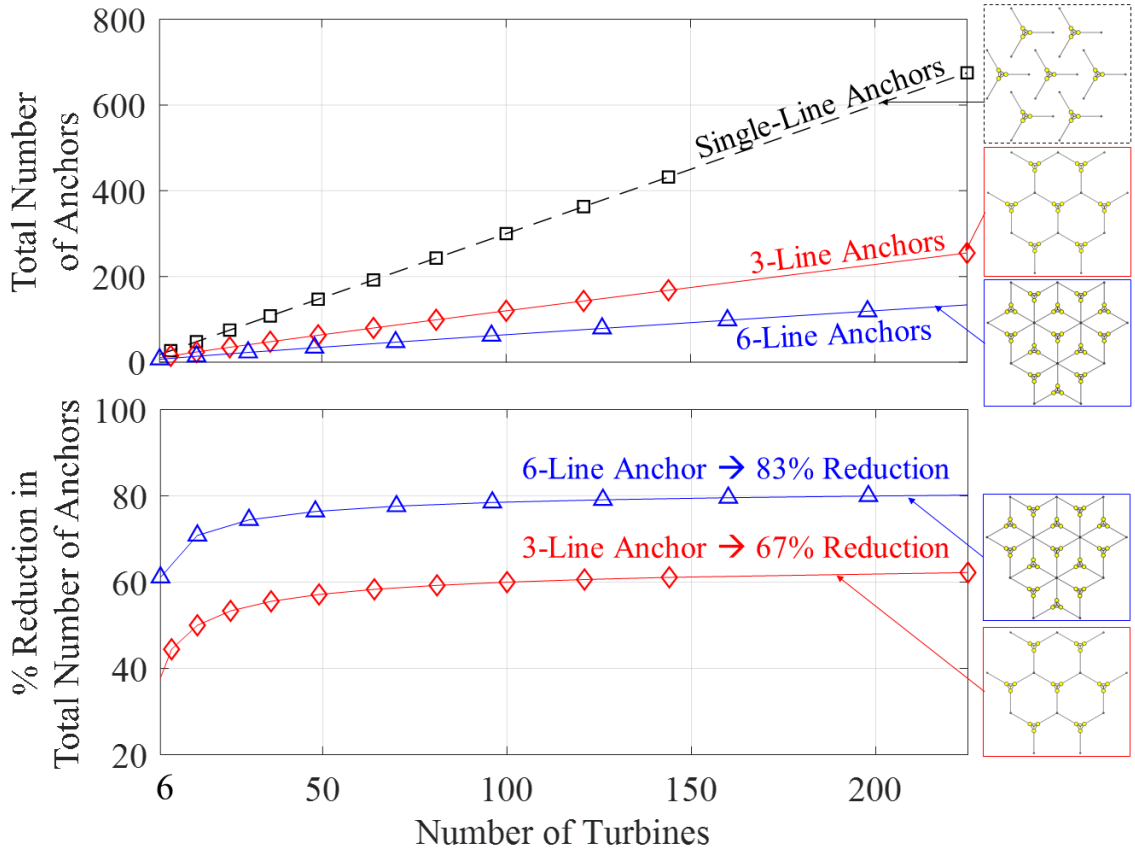

Figure 11: Total number of anchors for the single-line, 3-line, and 6-line geometries relative to farm size, and percent reduction in total number of anchors from single-line concept

For a hypothetical commercial scale wind farm of 100 FOWTs, the use of 3-line or 6-line anchor systems would result in 60% or 79% reductions in total number of anchors required, respectively. The sharp increase in percent reduction at low numbers of FOWTs is result of sharply decreasing perimeter effects. This initial analysis is strictly limited to number of anchors and does not include cost of anchor materials or installation.

It is anticipated that floating wind installations may use larger capacity turbines than the 5-MW model used in this study [7]. While changes in turbine size has not been

specifically studied in the context of the multiline anchor concept, it is possible that larger turbines may mean fewer turbines per farm, so the percent reduction in number of anchors and installations may be lower (note the scale effects in Figure 11).

2.3 Definition of Multiline Anchor Force

A key goal of this work is to understand the dynamics of the multiline anchor net force, as this novel system in which a single anchor is loaded by multiple mooring lines from different directions has not been used for FOWTs in practice or explored in concept. This section is devoted to the description of the multiline anchor system and forces in order to clarify the following analysis of mean and fluctuating anchor forces, maximum anchor forces, and anchor force directionality.

In single-line anchor systems, the dynamics of the loading on the anchor is governed by a single line connected to it. In multiline systems in which anchors are shared amongst the FOWTs, the anchor is loaded by 3 or more lines simultaneously. This introduces the need to analyze the net multiline loading on the anchor and how it differs from the single-line loading.

In the following description of the multiline anchor system and forces, the subscript of a value identifies the connected FOWT. A visual representation of the FOWTs, lines, and multiline anchor for the 3-line anchor system is shown in Figure 12 where T_1, T_2, and T_3 are the line tensions from the connected FOWTs 1, 2, and 3 that make up the multiline anchor net force.

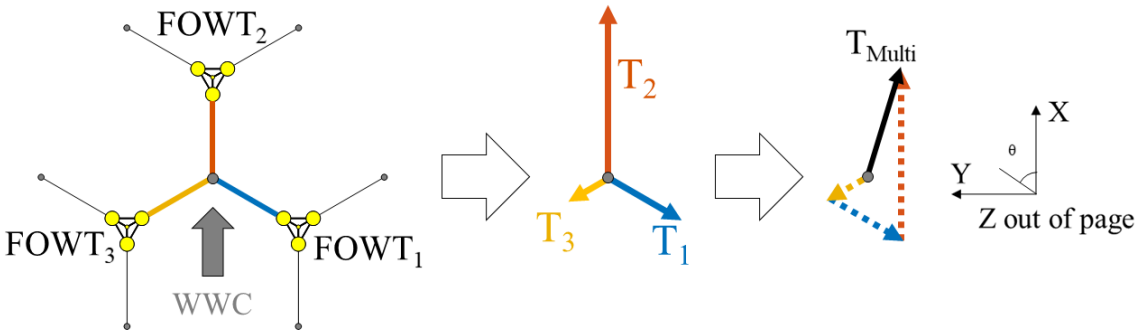

Figure 12: Diagram of multiline anchor net force from single-line contributing tensions of the 3 connected floating offshore wind turbines (FOWTs) for the 3-line anchor with 0° wind, wave, and current (WWC) direction. WWC direction is designated as θ, with 0° pointing to the top of the page, and 90° pointing to the left

The multiline anchor net force is found with vector summation, given by

$$\boldsymbol{T_{multi}(t)} = \sum_{i=1}^{n} \boldsymbol{T_i(t)} \qquad \textbf{(2)}$$

where T_i is the vector containing the x, y, and z components of the contributing line tension at the shared anchor and n is the number of mooring lines connected to the anchor.

Since the mooring system is catenary, there is always a portion of line laying on the seabed, and there are no uplift forces on the anchor at the seabed. As a result, the z-component of any contributing single-line tension is always zero, and the magnitude of the multiline line anchor force in the XY plane, T_{multi}, can be simplified to

$$\boldsymbol{T_{multi}(t)} = \sqrt{\boldsymbol{T_{multiX}(t)^2 + T_{multiY}(t)^2}} \qquad \textbf{(3)}$$

where T_{multiX} is the sum of the X-components of the contributing line tensions and T_{multiY} is the sum of the Y components of the contributing line tensions. Furthermore, the direction of single-line anchor force in the XY plane has a range of less than 3° for the FOWT system of this study. This is a result of the very large fairlead-to-anchor distances (>800 m) relative to small platform motions (<20 m). Therefore, it can be reasonably approximated that the lines connected to the 3-line anchor apply tensions at 120° from

one another (Figure 10B), and the lines connected to the 6-line anchor apply tensions at 60° from one another (Figure 10C). For the 3-line anchor

$$\boldsymbol{T_{multiX}(t) = T_2(t) - cos\,60\,[T_1(t) + T_3(t)]} \quad \textbf{(4)}$$

$$\boldsymbol{T_{multiY}(t) = sin\,60\,[T_3(t) - T_1(t)]} \quad \textbf{(5)}$$

And for the 6-line anchor,

$$\boldsymbol{T_{multiX}(t) = T_2(t) + cos\,60\,[T_4(t) + T_6(t) - T_1(t) - T_3(t)] - T_5(t)} \quad \textbf{(6)}$$

$$\boldsymbol{T_{multiY}(t) = sin\,60\,[T_3(t) + T_4(t) - T_1(t) - T_6(t)]} \quad \textbf{(7)}$$

where T_1, T_2, T_3, T_4, T_5, and T_6 are the magnitudes of the line tensions at the anchor from the connected FOWTs. This method of vector summations is supported by the work of co-author Landon's student, in which physical modeling of a suction caisson loaded orthogonally showed that the resultant load resistance of the multiline anchor correlated very well with the vector summation of the contributing line tensions [31]. This validation of the vector summation method for net multiline anchor force calculation is important in that multiple lines attached to a single anchor is a novel system; therefore, there are no specific standards that dictate how to calculate forces in this configuration.

2.4 Model and Analysis Methods

This section describes the FOWT model, simulation software, and environmental loading conditions used to generate time histories of the anchor force dynamics.

2.4.1 Turbine, Floating Platform, and Mooring System

The turbine chosen for this analysis is the National Renewable Energy Laboratory's (NREL) 5-MW reference turbine, and the support structure chosen is the OC4-DeepCwind semisubmersible floating system [34]. NREL's 5-MW reference turbine was developed to be representative of a typical utility-scale turbine and is widely used in

the offshore wind energy research community [35]. The OC4-DeepCwind semisubmersible floating system was chosen because it employs the most commonly studied platform type (semisubmersible) and mooring system type (catenary) in current FOWT technology/concepts [32]. The buoyancy-stabilized semisubmersible platform also possesses a variety of advantages, including suitability in any water depth, low installation vessel requirements, onshore assembly, and towing stability [32]. Spatial layout of the OC4-DeepCwind floating system for 3-line and 6-line multiline anchor geometries are shown in Figure 13, and relevant properties of the OC4-DeepCwind mooring system are provided in Table 1 [33].

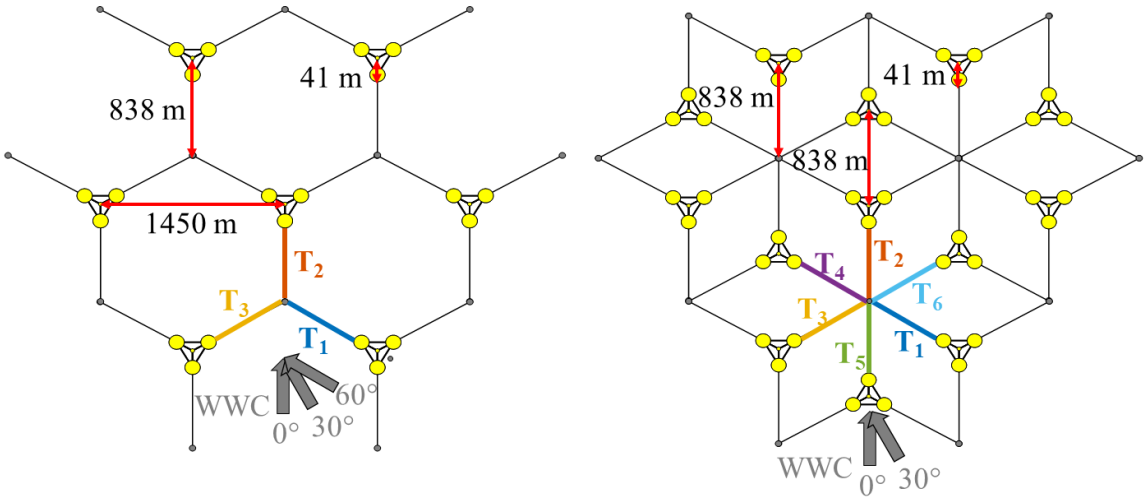

Figure 13: Spatial layout of the multiline anchor connection and OC4-DeepCwind floating system for A, 3-line anchors; B, 6-line anchors. Water depth = 200 m. WWC = wind, wave, and current

The 3-line and 6-line anchor geometries result in inter-turbine spacings of 1451 and 838 m, respectively. The spacing of the 3-line system is consistent with the spacing of the first and only floating offshore wind farm—Hywind Pilot Park—which consists of 5 FOWTs and employs a spacing of 1386 m [36]. It should be noted, though, that the Hywind project is installed in water depths of 95–120 m [36], which is shallower than the

200-m water depth of the OC4-DeepCwind floating system model [33], [34]. The contributions of line tensions from FOWTs 1, 2, and 3 are the same for the 3-line and 6-line anchor system, and the 6-line anchor system has an additional 3 FOWTs connected to the anchor.

2.4.2 Simulation Software and Mooring Model

The dynamics of the FOWT system are modeled with NREL's FAST (Fatigue, Aerodynamics, Structures, and Turbulence) Code. FAST v8 is a comprehensive, fully coupled aero-hydro-servo-elastic simulator capable of predicting motions and loads in the time domain [37], [38]. Mooring line and anchor force dynamics were simulated via MoorDyn, a lumped-mass mooring model within FAST. MoorDyn was chosen out of the 3 available mooring models in FAST for its combination of accurate prediction of mooring dynamics and high computational efficiency. The model accounts for mooring line axial stiffness and damping, weight and buoyancy forces, and hydrodynamic forces from Morison's equation [39]. Line properties for the OC4-DeepCwind mooring system in the MoorDyn input file are taken from Hall and Goupee [40]. Furthermore, MoorDyn has been validated against experimental test data and industry standard software to yield accurate results for mooring dynamics [40].

The American Bureau of Shipping Guide for Building and Classing FOWTs requires friction force be included in the calculation of anchor force [41], as friction between the mooring line and seabed can have a significant effect on anchor forces, especially in catenary mooring systems where large portions of the chain are resting on the seabed [42]. Friction force is not currently included in MoorDyn. FAST models the anchor as a fixed point at the seabed surface, but it should be noted that this

simplification does not affect mooring line dynamics. For this chapter, seabed friction was applied to the anchor force in a postprocessing routine. Time histories of the mooring line lay length were first determined from MoorDyn node location output, and seabed friction force, $F_{friction}$, was calculated by

$$\boldsymbol{F_{friction}(t) = fL(t)W_{sub}} \quad \textbf{[41]} \qquad \textbf{(8)}$$

where t is the time, f is the coefficient of static friction between the chain and the seabed, taken here as 1.0 as given by American Bureau of Shipping [41], L is the lay length of the mooring line on the seabed, and W_{sub} is the submerged unit weight of the mooring line [41]. Anchor forces from FAST outputs then were subsequently decreased by the force of the seabed friction at each time step. The number of segments per line used for the lumped-mass mooring dynamics model was increased from 20 to 165 to increase the accuracy of the lay length time history. Friction forces may change slightly over time, but in this study, the ABS recommended approach described above has been used [43].

2.4.3 Environmental Conditions

It is important to evaluate the dynamics of the multiline anchor net force over a wide range of environmental and operating conditions. In an effort to narrow down the combination of WWC parameters to test, several critical design load cases (DLCs) are selected for this analysis, shown in Table 2. These cases include both operating and nonoperating, and both normal and extreme conditions. Most importantly, the governing environmental load is different for each case, which allows for differentiation of the multiline anchor load effects between each type of environ- mental loading. Governing load refers specifically to wind or waves, as current loads are typically much smaller.

DLC 1.2 is wind dominated, DLC 1.6 is wind-and-wave dominated, and the survival load case (SLC) is wave dominated.

Table 2: Details of environmental loading conditions [43]

Load Case	DLC 1.2	DLC 1.6	SLC
Conditions	Normal Operating (Fatigue)	Extreme Operating (Strength)	Extreme Non-Operating (Strength)
Wind Speed at Hub Height	10.2 m/s	11.4 m/s (rated)	45 m/s (500-yr)
Turbulence Intensity	9%	10%	10%
Significant Wave Height	2.7 m	8.0 m (50-yr)	12 m (500-yr)
Peak Spectral Wave Period	7.0 sec	12.7 sec	15.3 sec
JONSWAP Gamma Factor	2.5	2	2.5
Current Speed	0.23 m/s	0.30 m/s	0.55 m/s

The WWC parameters for these 3 critical environmental conditions are taken from the full-scale VolturnUS project [44], harvested from over 10 years of buoy data at a site off Monhegan Island, Maine [45], [46]. The water depths of the OC4-DeepCwind FOWT and the full scale VolturnUS project are 200 and 168 m, respectively. Therefore, the environmental conditions were deemed to be suitable for use in this study. The wind speed in DLC 1.6 of 11.4 m/s is the rated wind speed of the NREL 5-MW reference turbine that produces peak thrust [35], as designated in American Bureau of Shipping [41]. The turbulent wind field is generated with a Kaimal spectrum via Turbsim [47]. Waves are generated with a JONSWAP spectrum, and wave heights are Rayleigh distributed [48], consistent with the modeling choices in Coulling et al. [34]. Current is steady and equal at each FOWT. Co-directional WWC directions of 0°, 30°, and 60° are evaluated for the 3-line anchor geometry, and directions of 0° and 30° are evaluated for the 6-line anchor geometry. The range of 0° to 60° is suitable for capturing the range of

important dynamics for the 3-line anchor system because the geometry has 120° rotational symmetry. For the 6-line case, only 0° to 30° WWC directions are needed because the 6-line anchor geometry has 60° rotational symmetry (see Figure 13). Furthermore, these direction ranges of WWC are also appropriate because yaw misalignment is not included. Six 1-hour simulations using different random seeds were completed for each combination of load case and WWC direction.

Each of the FOWTs connected to the multiline anchor are subjected to independent wind fields and independent wave fields; therefore, wind wake effects and spatial coherence of the waves are not included [24]. As a rule of thumb, wind wake effects can be neglected when the turbines are spaced more than 10 rotor diameters apart [49]. The NREL 5-MW reference turbine has a rotor diameter of 126 m, making the turbine spacing at which wake effects can be considered negligible 1260 m. In the 3-line anchor system, the turbine spacing is 1451 m, and the assumption of negligible wake effects is appropriate in this case. In the 6-line anchor system, the turbine spacing is 838 m, and wake effects are not negligible in this case. For example, the decrease in wind speed due to wake effects from 11.4 to 9 m/s [49] would decrease the rotor thrust from 800 kN to roughly 500 kN [50] in DLC 1.6 for the 6-line anchor system. Including wake effects in this stage significantly increases the number of permutations of conditions with WWC directions; therefore, they are not considered in this study. However, the inclusion of wake effects in a farm scale analysis of the multiline concept is an ongoing subject of research for the authors, as it is likely to produce some changes in the mooring line tensions and anchor forces.

Furthermore, the connected FOWTs are subjected to independent wave fields, and spatial coherence of the waves is not included. This decision is supported by previous work from the authors, which concluded that there was no significant difference between anchor force characteristics for connected turbines loaded by spatially coherent waves versus with independent waves [24]. Additional ongoing work on this topic has further shown that correlation in coherent wave fields is insignificant for points separated by more than several hundred meters, depending upon wave parameters.

2.5 Multiline Anchor Loading Dynamics

Using multiline anchors for FOWTs is a novel idea; therefore, it is important to examine a wide variety of dynamic effects on the anchor loading. This section will examine general trends, mean and maximum forces, and directionality of the multiline anchor net force.

2.5.1 Anchor Force Magnitude and Variation

Due to the direction of environmental loads chosen for this study, T_2 is greater than or equal to the largest contributing tension in all load cases and WWC directions because it is connected to the one of the FOWTs that is most directly downwind of the anchor (see Figure 13). Therefore, comparisons of forces will be made between the multiline anchor net force, T_{multi}, and T_2 from the single-line case. The multiline anchor net force in the 3-line anchor system is a combination of line tensions T_1, T_2, and T_3, (Equations (4) and (5)), and the multiline anchor net force in the 6-line anchor system is the same combination of T_1, T_2, and T_3, plus the additional contributions of T_4, T_5, and T_6 (Equations (6) and (7)), as shown in Figure 14.

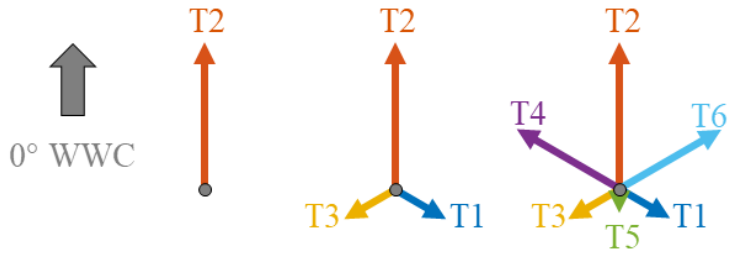

Figure 14: Line tension(s) contributing to anchor force for A, single-line anchor; B, 3-line anchor; and C, 6-line anchor. Line tension vectors are proportional to mean tensions in DLC 1.2 with 0° wind, wave, and current (WWC) direction

The use of the same tensions between these different scenarios allows for a more direct comparison of the multiline anchor loading dynamics between single-line loading, 3-line anchor loading, and the 6-line anchor loading. An example of this direct comparison is shown in Figure 15, where a specific peak force event on the single-line anchor (T_2) is reduced under the loading of the 3-line anchor system and increased under the loading of the 6-line anchor system.

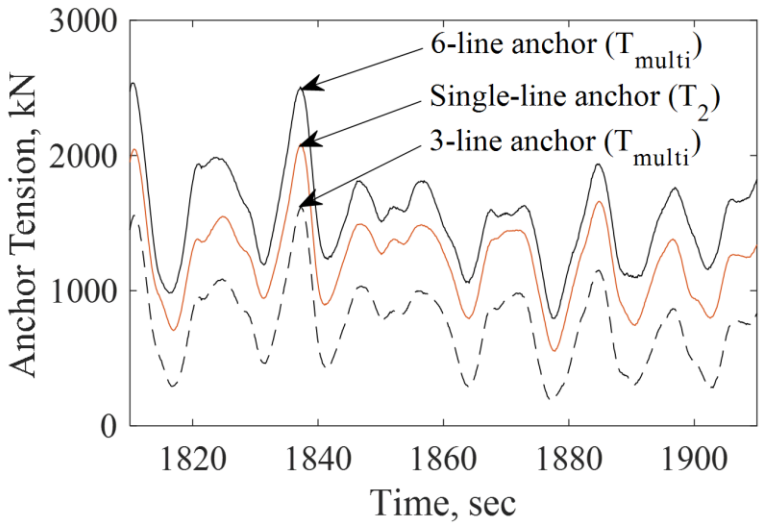

Figure 15: Comparison of same peak force event for single-line, 3-line, and 6-line anchor system

Examples of multiline anchor net force time histories, maximum forces, and contributing mean tensions are shown in Figure 16. While the magnitude of the specific

contributing tensions in Figure 16 change with load case and direction, there are some general characteristics that should be noted. First, there is a significant range in the contributing tensions on the multiline anchor. Second, symmetry of the mooring system configuration and WWC directions results in many cases where some of the contributing line tensions are approximately equal (i.e. T_1 and T_3 in the 3-line anchor, T_4 and T_6 in the 6-line anchor). Most importantly, the mean and maximum anchor force is decreased in the 3-line anchor system and increased in the 6-line anchor system, relative to the single-line system.

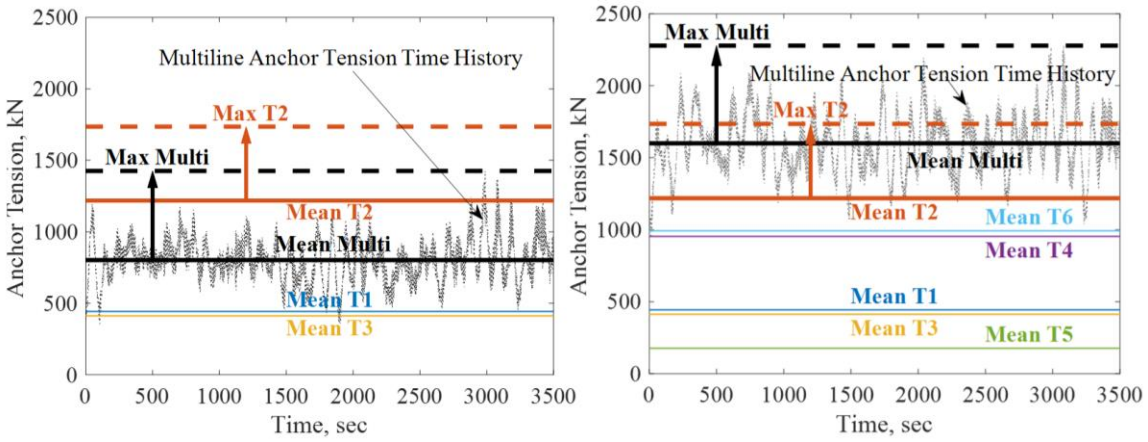

Figure 16: Time history of multiline anchor net force, means of contributing line tensions, and maxima of the maximum contributing single-line (T2) and multiline anchor net forces in wind-dominated normal operational design load case 1.2 with 0° wind, wave, and current direction for A, 3-line anchor and B, 6-line anchor

A broader evaluation of the single-line and multiline anchor net forces can be accomplished by comparing the mean, maximum, and standard deviation of the forces, as shown in Table 3. In general, the mean, maximum, and standard deviation are lower for the 3-line anchor and higher for the 6-line anchor, compared with the single-line anchor. This trend can be understood by revisiting the vector sum of the line tensions in each geometry and noting the direction of each line's tension components (see Figure 14). The

maximum contributing single-line tension (T_2) is always applying force directly in the positive X direction (upwards on this page). In the 3-line anchor system, T_1 and T_3 always have components in the negative X direction (downwards on this page), opposite of the governing maximum contributing tension. Therefore, these contributing line tensions are only able to cancel out force in the X direction, never adding to it. In contrast, the 6-line anchor has additional contributing line tensions—T_4 and T_6—that have components in the same direction as the maximum contributing single-line tension T_2 (positive X); therefore, the vector sum results in an addition of tensions, instead of a cancellation. It should be noted that the 0° and 60° WWC direction for the 6-line case are identical loading scenarios.

Table 3: Mean, maximum, and standard deviation of the single-line and multiline anchor net forces in kN. Red shading shows percent increase from single-line anchor value, and green shading shows percent decrease from single-line anchor values

		0° WWC Direction			30° WWC Direction			60° WWC Direction		
		Single -Line	3-Line	6-Line	Single -Line	3-Line	6-Line	Single -Line	3-Line	6-Line
Maximum, kN	DLC 1.2	1,726	-19%	29%	1,672	-22%	31%	1,411	-16%	58%
	DLC 1.6	2,560	-16%	20%	2,250	-18%	32%	1,610	-16%	90%
	SLC	3,767	-11%	8%	3,283	-13%	27%	2,127	-14%	91%
Mean, kN	DLC 1.2	1,218	-34%	32%	1,165	-30%	38%	987	-18%	63%
	DLC 1.6	1,238	-33%	34%	1,194	-29%	40%	1,019	-17%	63%
	SLC	1,166	-32%	27%	1,099	-27%	36%	923	-17%	60%
Standard Deviation, kN	DLC 1.2	116	19%	53%	114	4%	49%	119	-9%	49%
	DLC 1.6	280	0%	14%	229	-7%	28%	148	-12%	116%
	SLC	581	-14%	3%	476	-25%	20%	238	-16%	152%

Section 2.2 revealed that the 3-line and 6-line anchor geometries can reduce the total number of anchors required for a floating offshore wind farm, but due to differences in loading, these anchors also must be designed with different strengths. The key loading for this comparison is the maximum anchor force, as this value governs anchor design. In this study, the analyses used to determine the maximum anchor force required for design are the critical strength load cases, DLC 1.6 and SLC. It should be noted that in a true design, a larger number of DLCs would need to be completed to determine the maximum anchor force. The design force is determined from whichever WWC direction produces the largest anchor force. In almost all cases, this is the 0° WWC. The only situation for which this does not hold true is the 6-line anchor system in the SLC case, where the 30° WWC direction results in a larger maximum force than the 0° WWC direction. The results of the maximum anchor force data reveal that a multiline anchor used in the 3-line anchor system would require less strength than its single-line counterpart, while a multiline anchor in the 6-line anchor system would require more strength.

It can also be observed that for a given multiline configuration (3-line or 6-line), the mean multiline anchor net force is nearly identical across all WWC directions for given a load case—less than 4% different. This is due to the way that the contributing line tensions change with respect to each other as the WWC direction changes—as some lines transition to lower tensions, others transition to higher tensions, resulting in very little change in the mean of the net multiline anchor net force. Although the mean force experiences little change, the direction of the multiline anchor net force changes significantly.

The behavior of the multiline anchor net force is governed by the line contributing the largest tension, which is T2 in all load cases and WWC directions. This governing nature of the maximum contributing line is clearest for the cases where waves are the dominant environmental load (DLC 1.6 and SLC), as shown in the example in Figure 17.

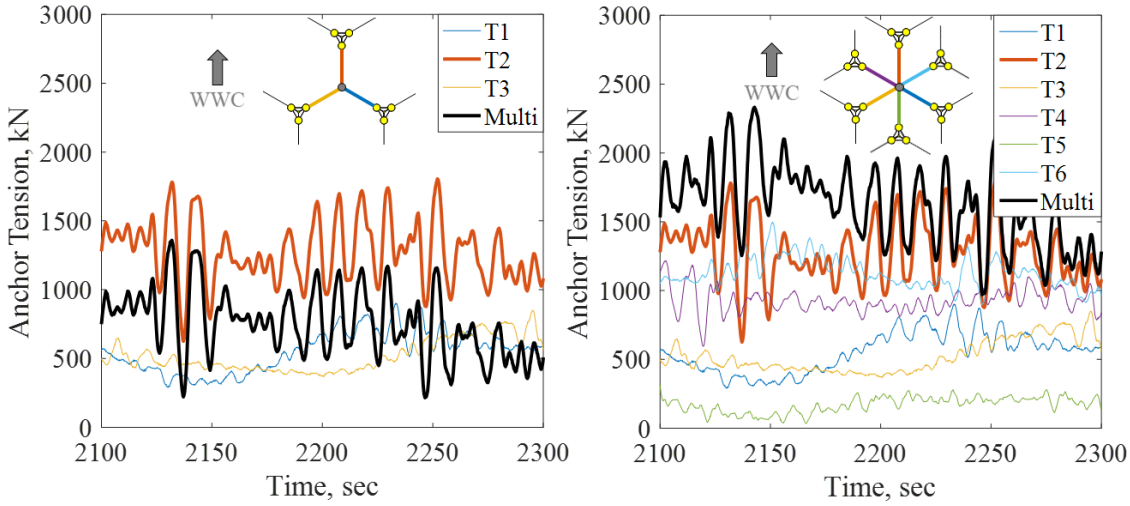

Figure 17: Contributing line tensions and multiline anchor time history in wind-and-wave dominated extreme operational design load case 1.6 with 0° wind, wave, and current (WWC) direction for A, 3-line anchor and B, 6-line anchor, showing governing behavior of the high T2

This governing nature of T2 is also relevant in the comparison of anchor forces for different WWC directions. For the 3-line anchor, the largest controlling nature of T2 occurs in the 0° WWC direction. In the 30° and 60° WWC direction, the governing line tension T2 is decreased, and the new governing contributing line tensions (T2 and T3) are closer in magnitude. These more balanced contributing line tensions reduce the multiline anchor net force cycle amplitudes as shown in Figure 18. This is because there is a greater proportion of the force being cancelled, as the components of large controlling T2 and T3 tensions in the direction perpendicular to the WWC direction are more equal but opposite. This trend is not present in the 6-line anchor system due to larger number of

contributing line tensions. In the 0° WWC direction for the 3-line system, the multiline anchor behaves very much like the single-line anchor because the contributions from the other lines (T_1 and T_3) are very small. In contrast, the 6-line system always has more than one line contributing a significant portion of the net force, and therefore consistently has more balance between the governing tensions.

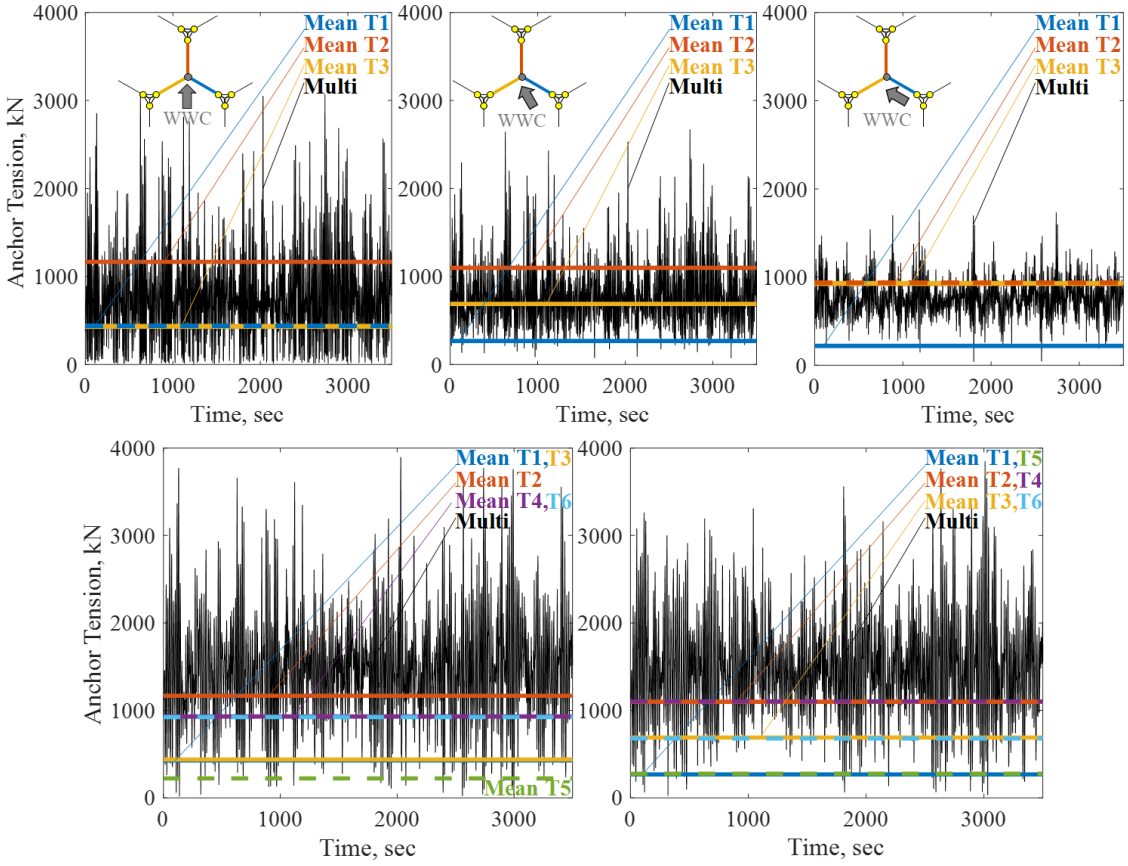

Figure 18: Multiline anchor time histories and mean contributing tensions in wave-dominated survival load case for the 3-line anchor for A, 0° wind, wave, and current (WWC); B, 30° WWC, and C, 60° WWC direction, and in the 6-line anchor for D, 0° WWC and E, 30° WWC

2.5.2 Directionality

A primary difference between the single-line anchor force and the multiline anchor net force is the directionality, and this directionality must be assessed over a range of time scales: short (single force cycle), medium (1-h time history with consistent WWC

direction), and long (days to years with changing WWC direction). It is important to note that multidirectional lateral loading on offshore anchors is a novel concept; therefore, applicable anchor design standards do not provide guidance or commentary relative to this type of loading. However, small-scale physical modeling of a suction caisson loaded in multiple directions has been conducted, revealing multiline anchor peak resistance greater than that of a caisson loaded in a single direction [30].

2.5.2.1 Directionality over 1 Hour

The forces on a single-line anchor come from one direction that has a range of less than 3° in this FOWT system, while the multiline anchor can be subjected to loading from any direction, depending on which contributing line tensions are largest (see Figure 12). Two characteristics of multiline anchor net force directionality in the 1-hour time scale are average direction and directional variation, which are given in Table 4. The maximum contributing single-line tension, T2, always has an angle mean of 0° and standard deviation of less than 1°. This approximately 0° standard deviation of the direction of the single-line force is a result of mooring geometry—the radial distance from the fairlead to the anchor is 800 m, and the platform displacements that move the mooring line are less than 20 m; therefore, the single mooring line's orientation with the anchor remains nearly unchanged.

Table 4: Mean and standard deviation of multiline anchor net force angle

		0° WWC		30° WWC		60° WWC
		3-line	6-line	3-line	6-line	3-line
Angle Mean	DLC 1.2	-2°	-2°	28°	28°	58°
	DLC 1.6	-5°	-4°	28°	26°	57°
	SLC	3°	1°	40°	30°	60°
Angle Standard Deviation	DLC 1.2	10°	7°	11°	7°	10°
	DLC 1.6	17°	8°	14°	9°	12°
	SLC	53°	18°	32°	22°	23°

Results in Table 4 reveal that the average direction of the multiline anchor net force is aligned with the WWC direction. This can also be seen in the force direction rosettes for the 6-line anchor in Figure 19 and the 3-line anchor in Figure 20. While only several examples of force direction rosettes are given, the alignment of the multiline anchor net force direction with the WWC direction appears in all load cases and WWC directions for both multiline geometries. The percentage labels on the circular axes depict frequency of the direction.

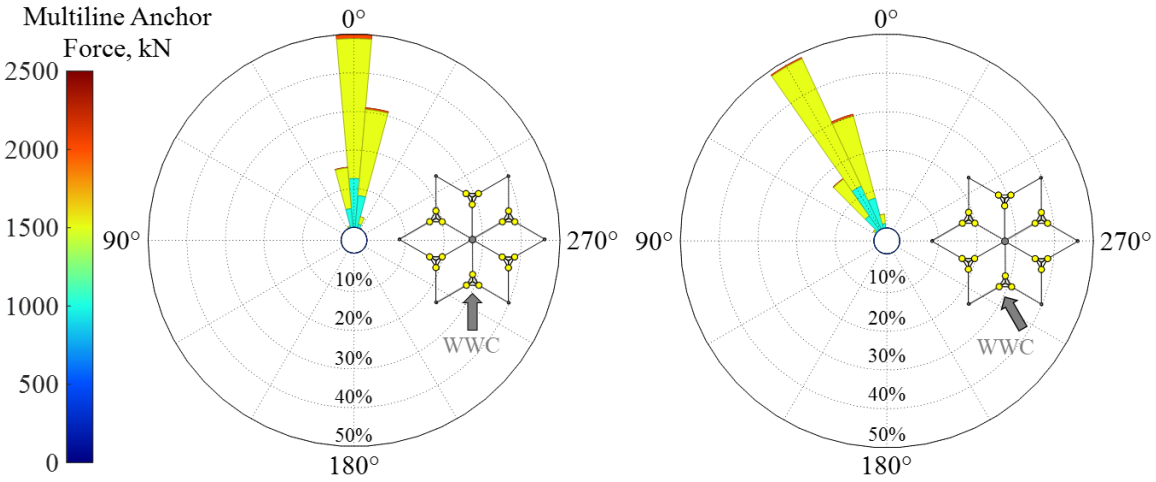

Figure 19: Direction rosettes for multiline anchor net force, example shown for 6-line anchor under wind-dominated design load case 1.2 loading with A, 0° wind, wave, and current (WWC) and B, 30° WWC

These results can be understood by considering the flow of forces; all connected FOWTs have a force applied to them in the direction of the WWC, and the fixed-point anchors are the nodes resisting this force. Therefore, the collective force applied to all connected FOWTs is applied to the multiline anchor in the same direction. In almost all cases, the average direction of the multiline anchor net force is within 4° of the WWC direction. The only exception to this is the 3-line anchor in SLC with 30° WWC, where

the average direction is 10° different from the WWC direction. This difference results from the specific combination of multiline geometry and load case. In the SLC, the waves are the dominant load (see Section 2.4.3), and they act primarily on the floating platform. In the 0° and 60° cases, the waves are hitting the platform along one of its lines of symmetry, but this is not the case for the 30° WWC direction. This wave loading along a line of asymmetry in the 30° case results in an asymmetry in the line tensions that is effectively translated to the anchor. The effect is not present in DLC 1.2 and DLC 1.6 because the wind load on the more symmetric rotor accounts for a larger portion of the loading, and the wind loading overshadows this effect of asymmetry in platform wave loading. Furthermore, this effect is also not present in the 6-line anchor system because although the asymmetry of the WWC direction and plat- form is still present, it is cancelled out by the symmetry of the 2 connected platforms loaded in this way (FOWTs 2 and 4, see Figure 13). The slight bias in average direction away from the WWC direction in the operational cases (DLC 1.2 and DLC 1.6) is a result of the small wind/rotor bias.

The results in Table 4 also show that the standard deviation of the multiline anchor net force direction increases as the load cases transition from wind dominated (DLC 1.2), to wind and wave dominated (DLC 1.6), to wave dominated (SLC). While this behavior is true of all load cases and WWC directions for both multiline geometries, it is shown most clearly for the 3-line anchor with 60° WWC direction, as seen in the rosettes in Figure 20.

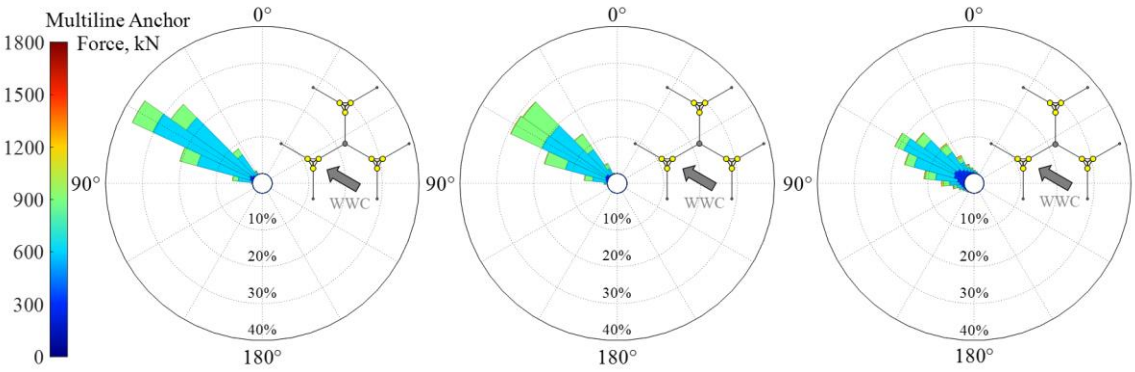

Figure 20: Direction rosettes for multiline anchor net force, example shown for 3-line anchor with 60° wind, wave, and current (WWC) under A, DLC 1.2 loading (wind dominated); B, DLC 1.6 loading (wind and wave dominated); and C, SLC loading (wave dominated)

The difference between wind loading and wave loading on an FOWT must first be discussed to understand this behavior. Wind loading acts on the rotor and contributes primarily to mean platform position and anchor force. Wave loading acts on the platform and contributes primarily to the force cycles and maximum force. In other words, the turbulence of the wind is insignificant compared with the fluctuation of wave elevation, relative to anchor forces. Due to this characteristic of the wave loading, the contributing line tensions have much larger fluctuations in cases that are wave dominated, and this larger variation in contributing line tensions results in the wider range in multiline anchor net force and direction. This is further supported by a comparison of correlation coefficients between anchor force and wave elevation at FOWT2 across the load cases, as shown in Table 5.

Table 5: Correlation coefficient between anchor force and wave elevation

	Single-line (Line 2 Max Contributing)			3-line anchor			6-line anchor	
	0°	30°	60°	0°	30°	60°	0°	30°
DLC 1.2	0.09	0.11	0.10	0.07	0.09	0.06	0.06	0.06

DLC 1.6	0.72	0.70	0.44	0.68	0.64	0.28	0.62	0.45
SLC	0.84	0.85	0.83	0.77	0.75	0.39	0.79	0.56

It is important to think about these directional results over the 1-hour time scale from a potential anchor design standpoint, for which there is one very important outcome. A wind farm may see WWC coming from any direction over the course of its 20- to 25-year lifetime, and since the multiline anchor net force is closely aligned with the WWC direction, a multiline anchor may see loading from any direction over the course of its operation. As a result, a multiline anchor must have axisymmetric strength. This is a valuable conclusion, in that catenary mooring line systems like the one in this FOWT typically use drag anchors, which do not have omnidirectional capacity. Therefore, different, but existing, anchor types must be investigated for the multiline application [29].

2.5.2.2 Directionality Over A Single Load Cycle

It has been shown that a multiline anchor can experience loading from any direction over the course of its design life and that the force direction is closely aligned with the WWC direction. It is also important to examine the variation in direction over a short time scale (on the order of a single force cycle), which can be from 7 to 15 seconds from wave loading.

In this chapter, direction reversal refers to events in which the component of the multiline anchor net force in the mean angle direction (Table 4) reverses to the opposite direction, as shown in the rose plot and time history of Figure 21. The cumulative percent of direction reversals in SLC are shown in Figure 22. Percent direction reversals are calculated relative to the number of local minima in the time history of the component of

the multiline anchor net force in the direction of the mean angle, and these percentages are averaged across 6 seeds.

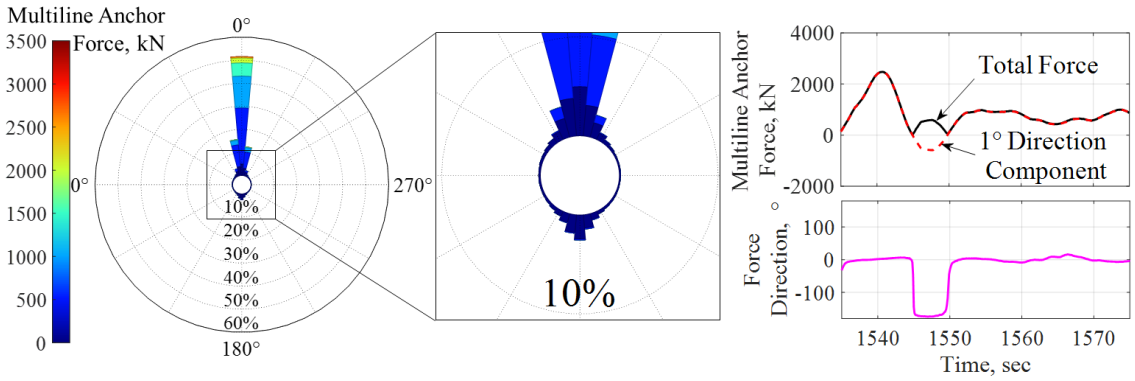

Figure 21: Direction reversal on 3-line anchor present in wave-dominated survival load case with 0° wind, wave, and current direction and 1° mean angle direction

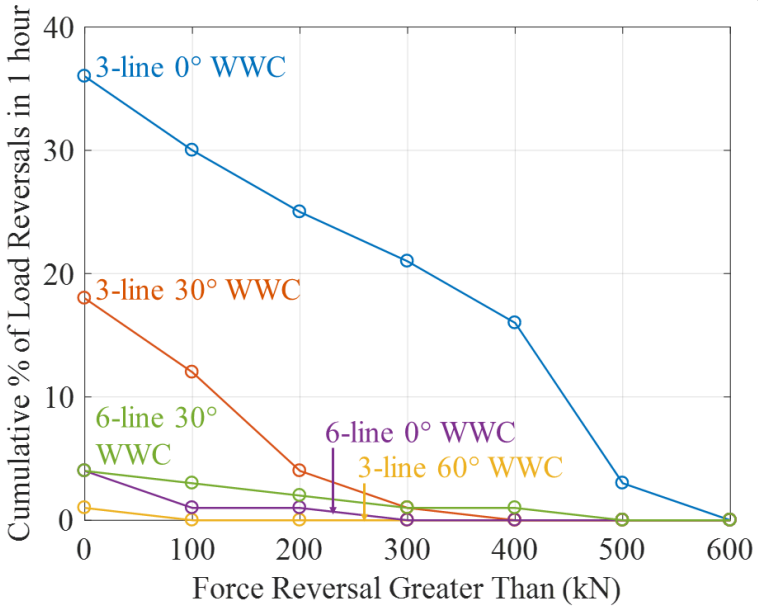

Figure 22: Cumulative percent of direction reversals relative to number of local minima in the component of the multiline anchor net force in the direction of the mean angle, for wave-dominated survival load case. WWC = wind, wave, and current

Direction reversal of the multiline anchor net force occurs most in this study under the 3-line anchor geometry in the SLC with 0° WWC direction. The higher occurrence of direction reversal in SLC is due to a combination of the large waves and small mean platform offset, which means that the governing contributing tension is

experiencing higher amplitude cycles at a lower mean force. Direction reversal is not a result of the nongoverning lines contributing higher tensions, but rather the governing line dipping to a very low tension. This commonly occurs following a peak tension event, after which the governing line (T_2) drops low enough that the other lines (T_1 and T_3) temporarily become the largest contributing tensions. Since the collective contribution of T_1 and T_3 is in the opposite direction of the normally governing T_2, direction reversal occurs.

While direction reversal is thought to be detrimental to offshore foundation performance [51], there are several characteristics that reduce this concern, the first of which is the infrequent nature of this behavior. Direction reversal does not occur at all in the normal operating load case (DLC 1.2), which approximates the most likely conditions the FOWT is to experience for the majority of its design life. Direction reversal occurs rarely in the extreme operating case (DLC 1.6)—only for the 3-line anchor with 0° WWC direction, and in this situation, less than 3% of the time. While direction reversal does happen frequently in the SLC, the SLC has a small probability of occurring in the FOWT's design life, and therefore, the probability of the direction reversal has a small likelihood as well. SLC is important for the determination of peak force events for use in anchor design strength but is not as relevant for cyclic analysis. Since direction reversal is a cyclic loading concern, it is only anticipated to be a significant design consideration if it occurs frequently in a more probable DLC, namely, those used in fatigue analysis. It should be noted that the critical design load case DLC 6.1, with nonoperational 50-year storm conditions, is not included in this analysis and is also expected to have occurrences of direction reversal.

In addition, while the multiline anchor net force does reverse direction, the magnitudes of the force direction reversals in Figure 22 are relatively small compared to the maximum multiline anchor net force in the direction of the mean angle as shown in the Table 6. Table 6 also shows the mean value of the force reversal as a percent of the previously occurring peak force in the opposite direction.

Table 6: Maximum multiline anchor net force in direction of the mean angle (compare to small force reversal magnitudes in Figure 14), and mean force reversal as a percent of the peak force that occurs just before reversal

	3-line anchor			6-line anchor	
WWC Direction	0°	30°	60°	0°	30°
Maximum force in direction of mean angle (kN)	3,347	2,650	1,487	4,047	4,055
Mean of force reversal as percent of previously occurring peak force (%)	17	10	6	4	8

When a direction reversal occurs in a force cycle, the mean of the force cycle is still heavily nonzero. This is an important distinction to make for an offshore anchor, as mean zero force cycles can lead to capacity reduction, while offset mean can lead to capacity increase [51]. Even in the most extreme realization of direction reversal, the reversed force is only 33% of the previous peak force in the mean direction, and the mean of the cycle is highly nonzero at 730 kN. However, the nature of multiline anchor net force direction range and reversal may be affected by extreme weather events with extreme wind directional changes, and this impact is an ongoing topic of study for the authors.

2.6 Conclusions

A multiline anchor concept is evaluated in which FOWTs share anchors, in an effort to lower FOWT support structure costs. Results of this analysis are compared to

conventional single-line anchor loading. It is shown that the implementation of the multiline anchor system in a floating off- shore wind farm would result in large reductions in the total number of anchors required—60% in the 3-line anchor system and 79% in the 6-line anchor system for a typical commercial scale 100-turbine floating offshore wind farm. The average maximum anchor force differs significantly for the multiline anchor compared with the single-line anchor, decreasing by 16% in the 3-line anchor and increasing by 20% in the 6-line anchor for DLC 1.6, and decreasing by 11% in the 3-line anchor and increasing by 10% in the 6-line anchor for the SLC. Therefore, the design strength of the multiline anchor would be different than its single-line counterpart.

It is also shown that a multiline anchor will be subjected to loading from any direction over the course of its design life, as the average direction of multiline anchor net force is aligned with the direction of the environmental load. Furthermore, force direction reversals within a single force cycle are present in extreme cases for the multiline anchor. A variety of anchor types with axisymmetric strength exist that can perform appropriately under such multidirectional loading conditions and differ from drag anchors that are being considered for mooring of single-line FOWTs. Suitability of different anchors for the multiline concept is discussed in Diaz et al. [29]. Other important considerations not examined in this chapter include effects of anchor placement accuracy and increased number of padeyes per anchor.

The anchor force results in Section 2.5 are specific to the OC4-DeepCwind semisubmersible floating system. However, general conclusions about multiline anchor systems with catenary mooring systems can still be made from this work, namely, that

multiline anchor forces will be significantly different from single-line anchor forces, mean direction of force will be aligned with the WWC direction, and force directional reversal may be present.

CHAPTER 3

SPATIAL WAVE COHERENCE IN MULTILINE ANCHOR SYSTEMS FOR FLOATING OFFSHORE WIND TURBINES

3.1 Introduction

As the offshore wind industry trends towards deeper water locations, the need for floating offshore wind technology becomes more important [7]. However, the additional support structure demands present in floating offshore wind turbines (FOWTs) currently prevent them from being cost competitive with fixed-bottom turbines [15]. One potential way to address this high cost hurdle is a multiline anchor concept, in which FOWTs share anchors to reduce the total number of anchors required, as shown in Figure 23 [25].

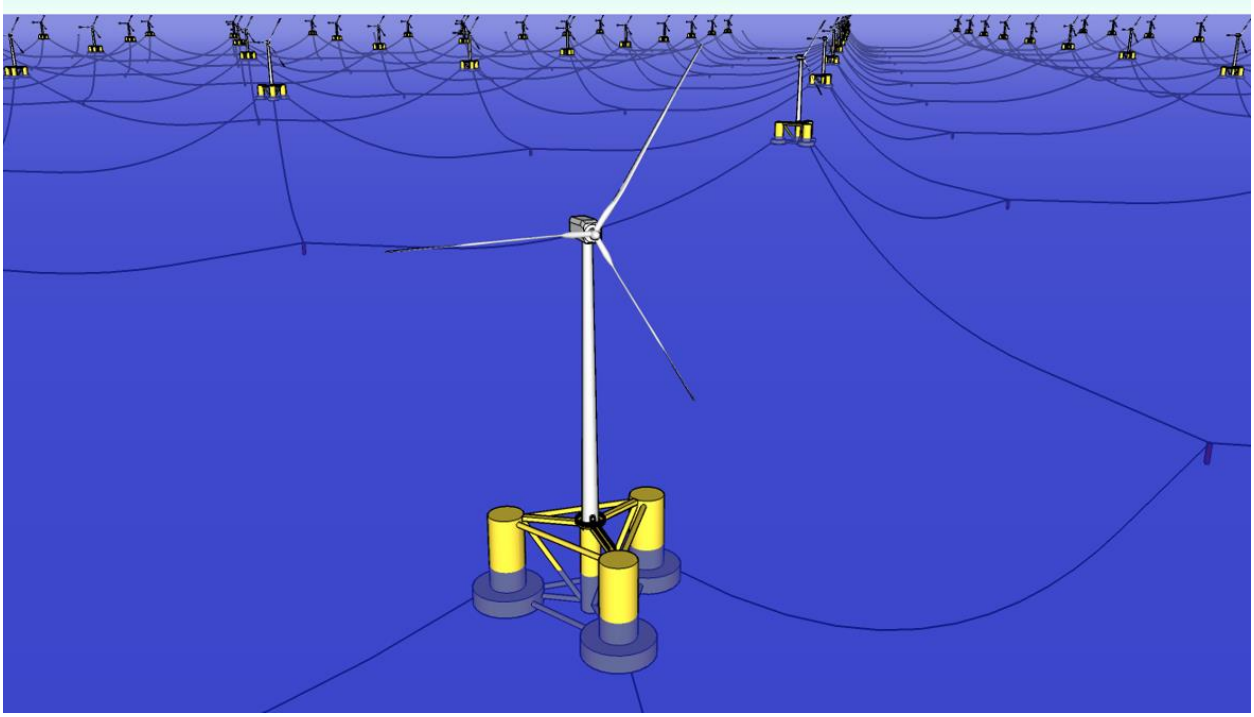

Figure 23: Multiline anchor system for floating offshore wind farm

A key difference in this novel anchoring concept is that the forces acting on the multiline anchor come from multiple turbines at several different locations in the wind farm, as

compared to the conventional single-line anchor, which only sees forces from one FOWT at one location. This interconnectedness of the system through shared anchor points creates the need to evaluate the loading of the multiline anchors on a multi-turbine, spatio-temporally coherent scale, since demands on the multiline anchor depend on the motions of multiple platforms at different locations in the wind farm.

The goal of this work is to determine if characteristics of the anchor loads are sensitive to spatial coherence of the wave field as it moves through an offshore floating wind farm, or whether an assumption of independence of the wave fields at different FOWT locations provides sufficiently accurate anchor load characterizations. This investigation of spatial wave coherence in multiline anchor systems will inform more accurate numerical modeling, an essential task when obtaining meaningful results for this novel system. Determining the importance of spatial wave coherence in multiline anchor force modeling is also a valuable outcome for all future multiline anchor analysis, as the simulations of spatially coherent waves are significantly more complex than those of independent wave fields, especially as the scale of the wind farm and number of wind turbines increase. For the purposes of this study, wind fields are assumed to be spatially independent at different FOWT locations. However, wake effects could play a role in governing multiline anchor forces, and this topic is a subject of ongoing study by the authors.

There are many examinations of spatial wave characteristics in published literature, but far fewer have looked at the wave surface over a large distance, and have mostly been limited to extreme and freak waves. Latifah and Groesen (2012) focused on estimating the position and time of a freak wave event given a time signal and phase

information at a certain position. Alvise et al. (2017) analyzed the temporal profile and height of space-time extreme wind waves using real wave data, in efforts to verify estimations of the shape and the crest-to-trough height of near-focusing large 3D wave groups. Other research on spatial characteristics of waves has been focused on the evolution of statistical wavefield parameters. Shemer and Sergeeva (2009) generated unidirectional random waves in 300 m wave tank to analyze changes in the frequency spectrum of the wavefield over the distance of travel. Additionally, Sergeeva et al. (2013) generated numerical simulations of unidirectional spatio-temporal wave evolutions, with a focus on rogue wave occurrence and propagation. As a distinction, one of the novel outcomes of this research is the examination of the correlation coefficient of wave elevation time histories at two different points in space. Furthermore, this research examines wave correlation and coherence over larger distances (>1000 m) than most previous studies.

The results of this study on spatial wave coherence are not limited to use in FOWTs with multiline anchor systems. Design of wave energy converters (WECs) may also benefit from better understanding of spatial wave coherence, as it could potentially be used to optimize the layout within an array such that each WEC experiences the largest waves, and in effect, produces the most power [56]. In addition, wave energy converters may also be a well-suited candidate for multiline anchor system applications. The role of spatial wave coherence in determining multiline anchor forces is addressed with numerical simulations of a multiline anchor connected to FOWTs loaded by spatially coherent and independent waves. This chapter first examines the effect of spatial wave coherence in a multiline anchor system for semisubmersible FOWTs, then

expands upon these results with an examination of just-waves realizations (no FOWT) to determine how wave characteristics affect the wave correlation lengths. In both of these sections, regular waves are first used to examine the dynamics in a simple context, then irregular waves are used to more accurately simulate real world conditions. Results are presented in the context of real spacings of installed offshore wind farms.

3.2 Multiline Anchor Force

This section examines a multiline anchor connected to FOWTs subjected to both regular and irregular wave loading. In this context, use of the terms in-phase versus out-of-phase to describe waves at the platforms is specific to regular waves, while use of the terms coherent versus independent are specific to irregular waves. The first goal of this section is to establish the range of the multiline anchor force for the case where the platforms connected to the anchor are loaded by in-phase versus out-of-phase regular waves. The following subsection then uses irregular waves to determine if the multiline anchor force dynamics are a function of wave coherence.

3.2.1 Software and Turbine Model

Simulation of FOWT dynamics was accomplished with National Renewable Energy Laboratory's computer-aided engineering tool FAST (Fatigue, Aerodynamics, Structures, and Turbulence). FAST v8 is a comprehensive, fully-coupled aero-hydro-servo-elastic simulator capable of predicting motions and loads in the time domain [37], [38]. The turbine chosen for this analysis is the National Renewable Energy Laboratory's (NREL) 5-MW reference turbine, which was developed to be representative of a typical utility-scale turbine, and is widely used in the wind energy research community [35]. The FOWT support structure chosen for this study is the OC4 DeepCwind

semisubmersible platform [33], [34], which is based largely on the DeepCwind scaled test floater [57] and consists of a ballast supported tri-floater with three large cylindrical columns acting as pontoons which are connected to a central main column that supports the tower and rotor nacelle assembly [33]. The DeepCwind OC4 semisubmersible floating system was chosen because it employs the most commonly studied platform type (semisubmersible) and mooring system type (catenary) in current FOWT technology/concepts [32]. Mooring line and anchor force dynamics were simulated via MoorDyn, a lumped-mass mooring model within FAST [58]. Seabed friction forces on the mooring line are not currently included in this model, and therefore were applied in a post-processing routine outlined in Fontana et al. (2017).

The spatial layouts of the conventional single-line and novel multiline FOWT systems are shown in Figure 24. The interconnectivity of the turbines in Figure 24b and 2c exhibits the need to examine whether the spatial coherence of the waves in the multiline system affects the anchor forces significantly, compared to the configuration of the turbines in Figure 24a where each anchor's load depends only on the dynamics of a single FOWT.

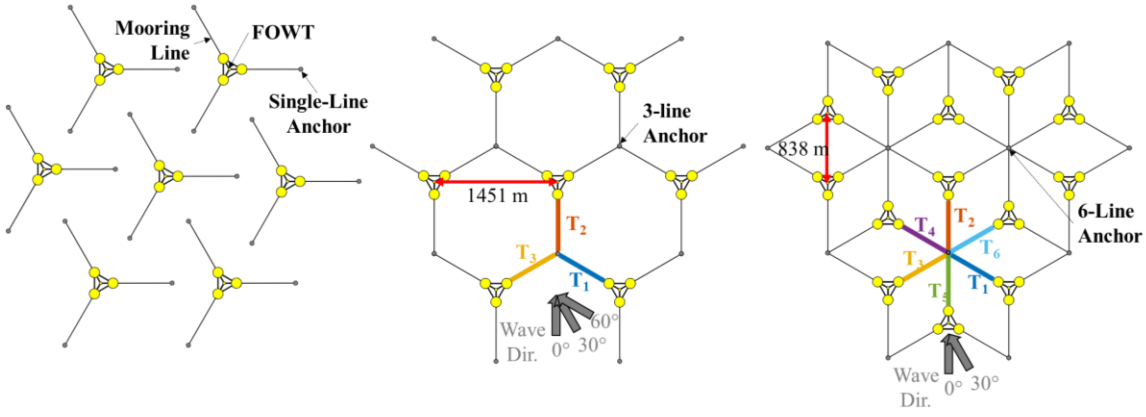

a.) Single-line anchor system b.) 3-line anchor system c.) 6-line anchor system

Figure 24: Layout of a.) single-line, b.) 3-line and c.) 6-line anchor system for FOWTs. Scale is consistent across all images.

To determine the net force on an anchor being loaded by multiple mooring lines simultaneously, simulations of single-line FOWTs are completed, then post-processed as shown in Figure 25. The net multiline anchor force is computed by the vector sum of the contributing single-line tensions.

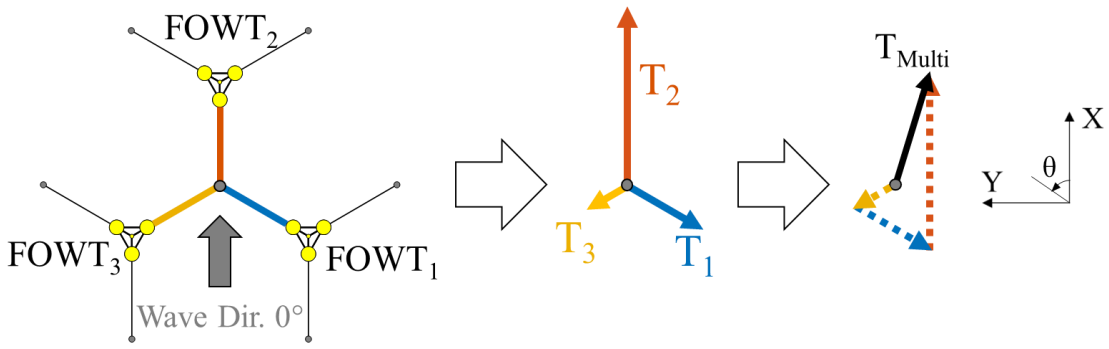

Figure 25: Calculation of net multiline anchor force from contributing single-line tensions. Example shown for 3-line anchor system with 0° wave direction. θ is the direction of the waves.

It can be observed that the magnitude and direction of the net multiline anchor force is a function of the contributing line tensions. The net multiline anchor force is controlled by the maximum contributing (critical) single-line tension, while the smaller (cancelling) tensions, create a reduction in this force. This is where wave coherence between connected turbines is most important, as the magnitude of this reduction depends on the timing of the cancellation tension relative to the critical tension.

3.2.2 Multiline Anchor Force with 1-Dimensional Regular Waves

The goal of this section is to determine the differences between the net multiline anchor force produced under perfectly in-phase and out-of-phase regular wave loading on the connected platforms. In-phase loading refers to regular wave crests acting on the

connected FOWT platforms simultaneously (Figure 26a), and out of phase loading refers to wave crests and troughs acting on the connected platforms simultaneously (Figure 26b). These two cases represent bounding/limiting realizations of the way that spatially coherent irregular waves may affect multiline anchor loads. Equation of the regular wave surface, η, in the time domain is

$$\boldsymbol{\eta(x,t) = a\cos(kx - \omega t + \phi)} \qquad \textbf{(9)}$$

where k is wave number, x is distance, ω is wave frequency, t is time, a is regular wave amplitude ($H/2$) and ϕ is the random phase. For simplification in describing the effects of wave phase relative to anchor tension, the following analysis focuses only on the 3-line anchor system.

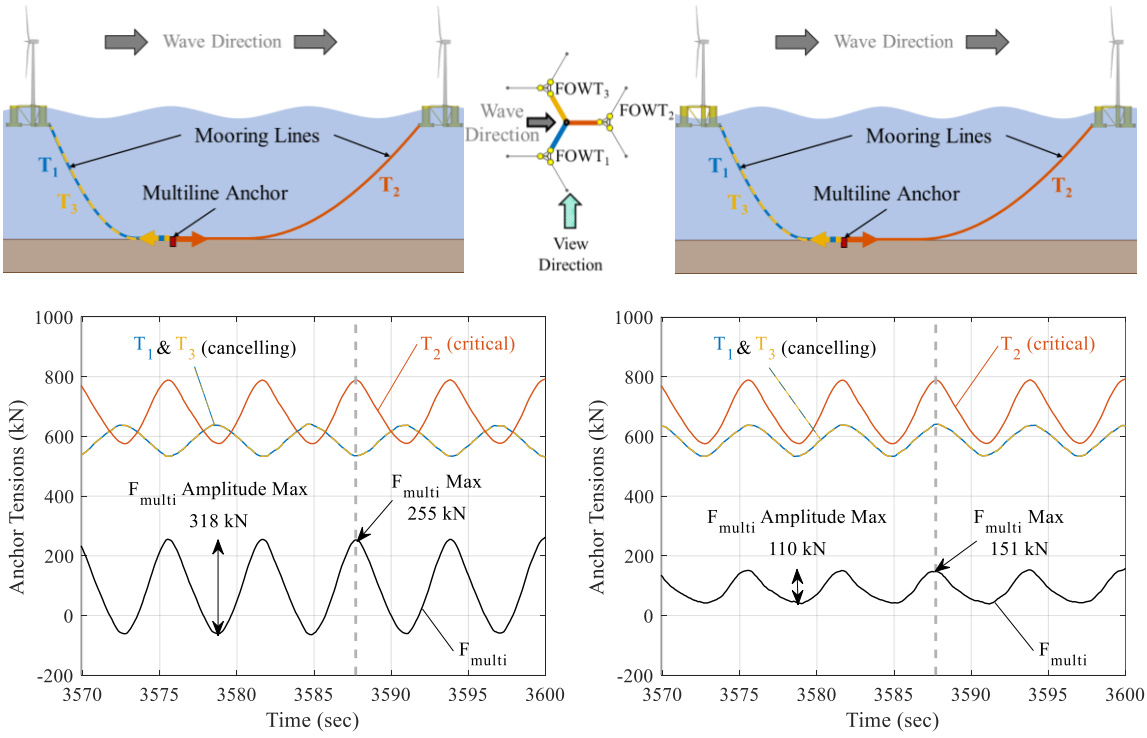

a.) Waves in-phase at connected platforms b.) Waves out-of-phase at connected platforms

Figure 26: Steady-state time history of contributing single-line tensions and net multiline anchor force for a.) in-phase wave loading and b.) out-of-phase wave loading. Example time histories are shown for 3 m regular waves with a period of 6.1 seconds and 0° wave direction. The wave height and length in the top figures are not to scale, so as to better exhibit wave phases.

Figure 26 reveals how the timing of the cancellation tension relative to the critical tension affects the cycle amplitude and maximum of the net multiline anchor force. To better understand these cases, the dynamics of the FOWT mooring system must first be examined. Wave elevation, platform displacement, and line tension are all tightly correlated. When a wave strikes and displaces a FOWT platform in its direction of travel, the upwind line (T_2) experiences peak tension, while the downwind lines (T_1 and T_3) simultaneously experience a minimum tension. Conversely, when a wave trough comes in contact, the platform displaces opposite the wave direction of travel, and in effect the upwind line (T_2) experiences a minimum tension while the downwind lines (T_1 and T_3) experience peak tensions. It should be noted however that these are general descriptions of the temporal relationship between wave strike, platform displacement, and line tension, as there can be significant and varying time delays between these events depending on the wave characteristics. Figure 26a is a specific example in which there is negligible time delay, and the peak & minimum tensions are nearly simultaneous with the wave strike on the platform.

When critical and cancelling contributing tensions are out-of-phase, the amplitude and maximum of the net multiline anchor force are maximized (Figure 26a). Conversely, when the critical and cancelling single-line tensions are in phase, the amplitude and maximum of the net multiline anchor force is minimized (Figure 26b). This behavior is related to interference, in that waves in-phase at the connected platforms produce

contributing line tensions with constructive interference, while waves out-of-phase at the connected platforms produces contributing line tensions with destructive interference. Spatial characteristics, namely wavelength, are not considered in this step because it is not possible to compare the same wave acting on the connected platforms in both an in-phase and out-of-phase scenario when spacing between the FOWTs is held constant. In order to produce perfectly in-phase and out-of-phase wave loading of a certain wave height on the set of platforms in a multiline system, the waves would need to have slightly different wavelengths and periods; a wave train with N waves over a distance of 1257 m (see Figure 24b) is different than a wave train with N+½ waves over the same distance. For example, a 6m regular in-phase wave (i.e. 10 waves between the platforms) has a wavelength of 125.7 m and a wave period of 8.97 seconds. In contrast, a 6m regular out-of-phase wave (10.5 waves between the platforms) has a wavelength of 119.7 m and a wave period of 8.75 seconds. Wavelength is determined by converting wave peak spectral period to angular frequency, then using angular frequency and water depth in the linear dispersion relationship [59] to determine wave number κ and in effect, wavelength. Instead, the steady-state minima and maxima of the line tensions produced under regular wave loading are used to examine the magnitude of the anchor force produced by different sized regular waves. More specifically, the regular wave scenario is used here to evaluate the question where given a sea state (regular wave height), what is the best (minimum) and worst (maximum) loading on the multiline anchor. The minimum and maximum values of the maximum net multiline anchor force for all wave loading cases (Figure 27) are found by offsetting the time between the critical and cancelling line tensions such that the maximum critical and minimum cancelling tensions are aligned in

time (in-phase waves at the platforms), or the maximum critical and maximum cancelling tensions are aligned (out-of-phase waves at the platforms), as previously shown in Figure 26.

The effect of wave phase at the platforms is examined over a range of wave heights and periods. In this context, wave period factor, t_f, is a value used in calculating wave period, given by

$$\boldsymbol{T = t_f\sqrt{H/g}} \qquad \textbf{(10)}$$

where T is wave period, H is wave height and g is gravity. Values of 11 and 14 for t_f are chosen to be close to the lower and upper bounds of this value as recommended in IEC 61400 (2009). Furthermore, the 0° wave direction is used for the entirety of this section because it is the most critical load direction case, meaning that it produces larger maximum single line and multiline anchor forces than those of the 30° and 60° case. Therefore, it is of the most interest relative to the effects of wave phases. Results are shown in Figure 27.

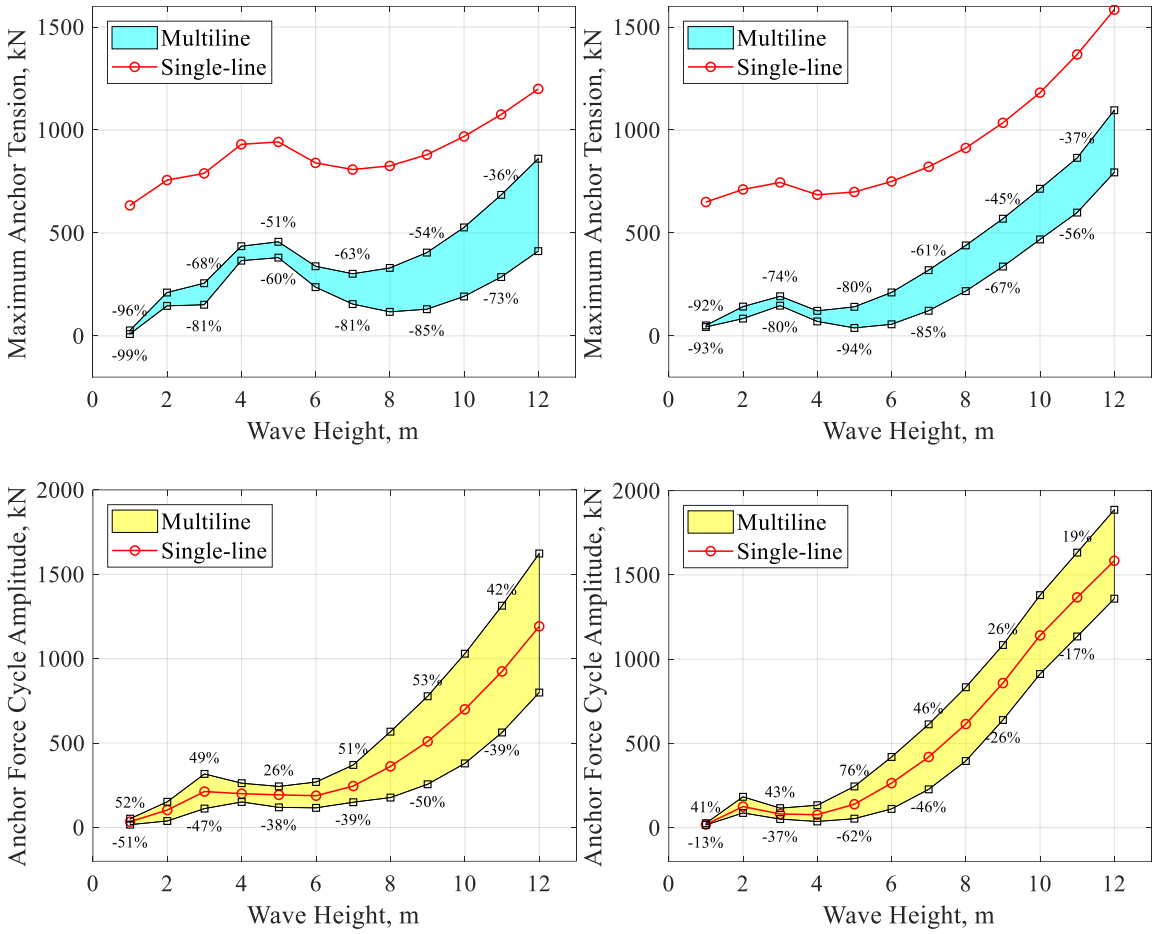

a.) 0° wave direction, t_f = 11

b.) 0° wave direction, t_f = 14

Figure 27: Maximum multiline anchor forces and force cycle amplitudes under regular waves acting on parked and feathered FOWTs (no wind). Results show critical single-line (T_2) and net multiline anchor force versus regular wave height for a.) 0° wave direction and t_f = 11, and b.) 0° wave direction and t_f = 14, with percent difference from the critical single-line value shown. The upper bound corresponds to roughly in-phase waves at the connected platforms, the lower bound corresponds to roughly out-of-phase waves at the connected platforms, and the colored fill between them indicates the range in values over the wave phase difference at the connected platforms.

In general, the range/variance of the net multiline anchor force relative to wave phase at connected platforms increases with wave height. The local maxima of anchor force that occurs at the 5 m wave height for t_f = 11 (T = 7.9 sec) and at the 3 m wave height for t_f = 11 (T = 7.7 sec) is due to the mean drift of the platform. This mean drift force results

from closeness of these wave frequencies to the rigid-body motion natural frequencies for the semisubmersible and its mooring system. Details on mean drift forces in the NREL semisubmersible floating system can be found in Coulling, Goupee, Robertson, & Jonkman (2013). The mean drift (or mean surge) displaces the platform in the direction of the waves, resulting on a higher mean tension on the critical line (T_2), and a lower tension on the cancelling lines (T_1 and T_3). It is this higher mean tension in critical line T_2 that amplifies on the maximum force for the wave periods close to the platform's rigid body motion natural frequency.

Similar trends are present for cases where the turbine is operating with the addition of a steady rated wind of 11.4 m/s and a steady current of 0.3 m/s in addition to regular waves, as shown in Figure 28.

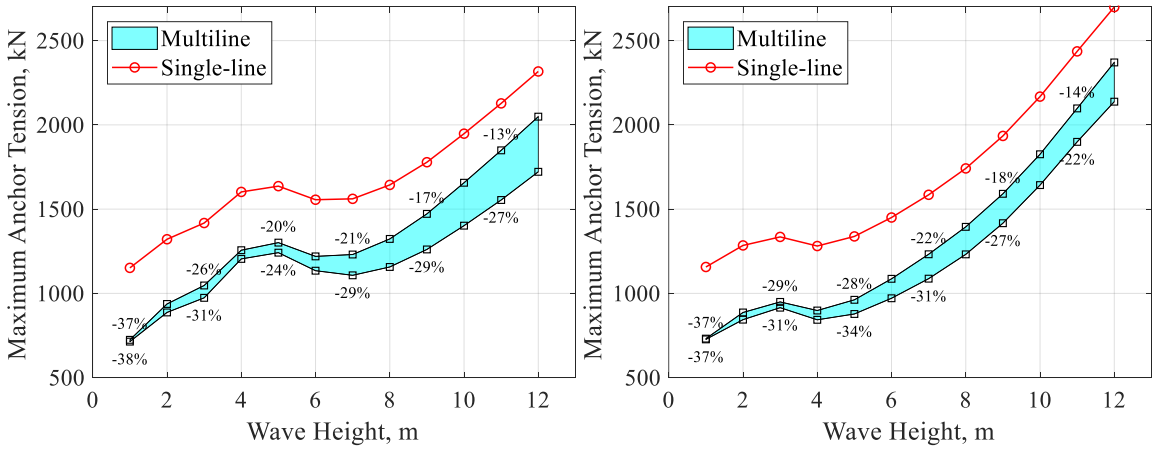

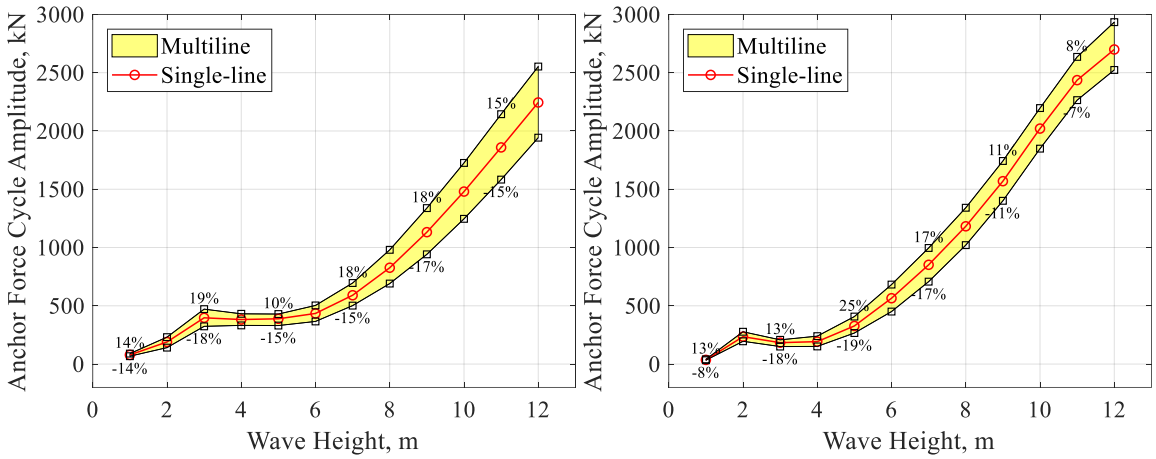

a.) 0° wave direction, t_f = 11

b.) 0° wave direction, t_f = 14

Figure 28: Maximum anchor forces and anchor force cycle amplitudes under regular waves, steady wind (11.4 m/s), and steady current (0.3 m/s). Results show critical single-line (T_2) and net multiline anchor force versus regular wave height for a.) 0° wave direction and t_f = 11, and b.) 0° wave direction and t_f = 14, with percent difference from the critical single-line value shown. The upper bound corresponds to roughly in-phase waves at the connected platforms, the lower bound corresponds to roughly out-of-phase waves at the connected platforms, and the colored fill between them indicates the range in values over the wave phase difference at the connected platforms.

The primary distinction of these operational cases compared to the wave-only cases is a smaller range/variance of the net multiline anchor force relative to wave phase at connected platforms increases with wave height. There is less sensitivity to wave phase differences in these operational cases because a significant portion of the line tension is being controlled by the wind loading, therefore changes in the wave phase have less effect. This is an important distinction to make over the non-operational wave-only scenario, as these larger values of anchor force are produced from a more realistic environmental conditions, and are likely closer to design values.

Anchor design is based primarily on a maximum anchor force [41]. Therefore, in this set of analyses, the difference in maximum net multiline anchor force between in-

phase and out-of-phase wave loading can be thought of a measure of uncertainty in anchor demand. Anchor design uses whichever load case produces the largest anchor force, therefore it can be observed from the values in Figure 27 and Figure 28 that the larger wave height cases encompass the conditions most likely to control anchor design. These larger wave height cases see larger differences between maxima produced by in-phase and out-of-phase wave loading, which would potentially lead to a more conservative anchor design if irregular spatial wave coherence were to be deemed important.

The amplitudes of the anchor force cycles are used primarily in checking the fatigue strength of the anchor, and the smaller wave height cases encompass the conditions most likely to be used in fatigue analysis. Since the difference between in-phase and out-of-phase force cycle amplitude values are smallest in these small wave height cases, it can be anticipated that spatial wave coherence will not have a significant impact on fatigue analysis, even if irregular spatial wave coherence were to be deemed important.

While the force cycle amplitudes in larger (extreme) wave height conditions are not likely to be used in a fatigue analysis of the anchor, the bounds are still important in the context of anchor force direction reversal. This behavior can be seen in Figure 26, where correlated loading produces a net multiline anchor force that reverses direction ($\min(F_{multi}) = -62$ kN), while the anti-correlated loading does not ($\min(F_{multi}) = +42$ kN). This behavior is of interest because force direction reversal is a characteristic of anchor loading that is not present in single-line anchors, which are only loaded in one direction. The effect of this force direction reversal within a single force cycle relative to anchor

design is not yet known, as anchor design standards currently only apply to single-line anchors. This type of anchor loading event has been examined in previous work by the authors, which determined that multiline anchors can experience force direction reversal within a single cycle for extreme loading conditions [25]. It should be noted that force direction reversal falls within the broader topic of multidirectionality of the anchor force, which is an ongoing topic of study for the novel multiline anchor concept.

3.2.3 Multiline Anchor Force with 1-Dimensional Irregular Waves

This section extends the previous section to the case of irregular 1-dimensional waves and seeks to understand how the multiline anchor force is affected by the use of spatially coherent irregular waves at connected platforms. The irregular waves in this study are modeled via the procedures outlined in Agarwal and Manuel (2010). They are linear, with a JONSWAP spectrum, and Rayleigh-distributed wave heights.

Fourier coefficients for sea surface elevation, *X*, are

$$\boldsymbol{X(\omega_m) = A_m \exp(-i\phi_m)} \quad \textbf{(11)}$$

Where A_m is the Rayleigh distributed amplitudes. The spatial phase shift is accounted for using the dispersion relationship at each frequency, given as

$$\boldsymbol{X(\omega_m) = A_m \exp(kx - i\phi_m)} \quad \textbf{(12)}$$

In the final step, Fourier coefficients are transformed to the time domain to obtain the wave surface, resulting in

$$\boldsymbol{\eta(t,x) = \Re\{IFFT[X(\omega_m, k, \phi_m, x)]\}} \quad \textbf{(13)}$$

This method of modeling creates time histories of one-dimensional spatially coherent waves over a distance [63]. When they are applied to the FOWT simulations, the variation in wave elevation is spanned only over the direction of travel, and wave

elevation is identical over the direction perpendicular to their travel due to the 1-dimensional nature, as shown in Figure 29.

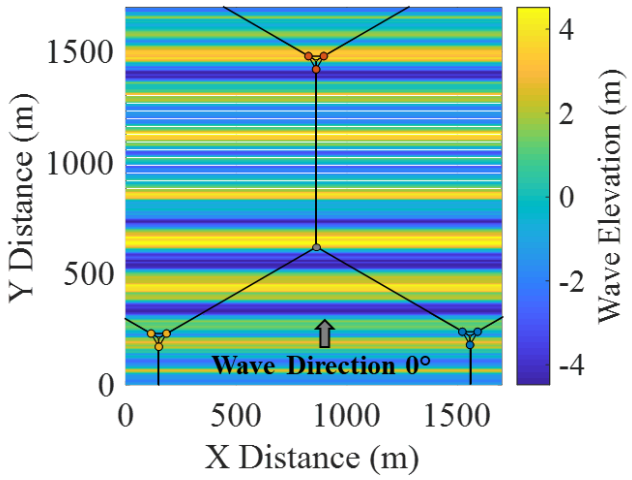

Figure 29: 1-dimensional irregular wave field traveling in 0° direction in 3-line anchor system for H_s = 8 m and t_f = 14

With this use of one-dimensional wave fields, multiple turbines connected to the multiline anchor experience identical wave loading under spatially coherent wave conditions. This is shown in Figure 30a for Turbines 1 and 3, and Figure 30c for Turbines 2 and 3. More specifically, the only scenario in which duplication of wave elevation time history at two turbines does not occur is for the 3-line anchor with 30° wave direction. Therefore, this case is focused on more specifically in the following analysis, although the other cases are discussed as well. Where there is wave loading duplication in the coherent case due to location (Turbines 1 and 3 in 0° degree, Turbines 2 and 3 in 60° direction), the corresponding independent wave loading case also uses 2 of the same, although independent, waves fields at these turbines for consistency in comparison (See Figure 30a and Figure 30c).

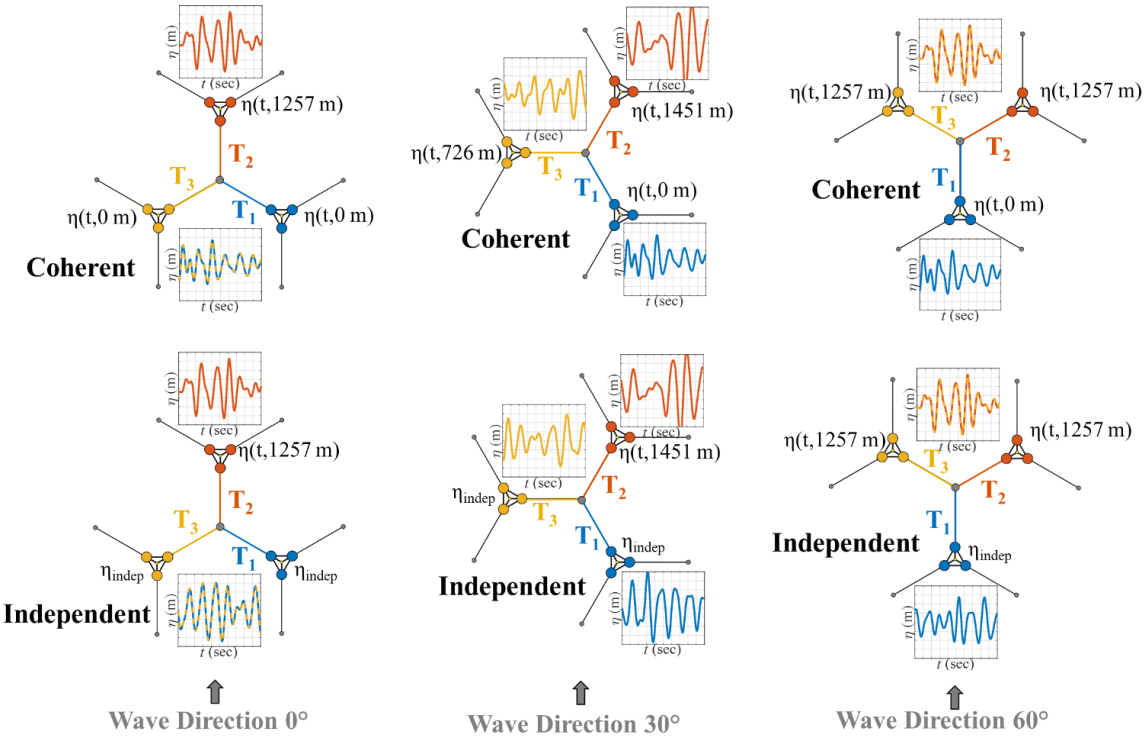

a.) 0° Wave Direction b.) 30° Wave Direction c.) 60° Wave Direction

Figure 30: Description of wave elevations for a.) 0° wave direction, b.) 30° wave direction, and c.) 60° wave direction

In this section, the coherent wave condition refers to simulations of the net multiline anchor force in which the connected turbines are loaded by spatially coherent waves, where wave elevation time history at the distance location of each turbine is generated via the procedure outlined in Equations (11) through (13). The independent wave condition refers to simulations of the net multiline anchor force in which the connected turbines are loaded by independent waves. To make the comparison between coherent and independent wave conditions, the wave history that generates the critical contributing line tension T_2 remains common, while cancelling tensions T_1 and T_3 are changed to fit the degree of wave coherence (see Figure 30). The contributing line tensions and the net multiline anchor force for the coherent and independent case can be seen in Figure 31.

Figure 31 also displays the how the dominant contributing force of T_2 controls the behavior of the net multiline anchor force. For each combination of wave significant wave height, wave period factor, direction, and coherence or independence, six realizations were completed, consistent with the number of realizations recommended by IEC for design [60].

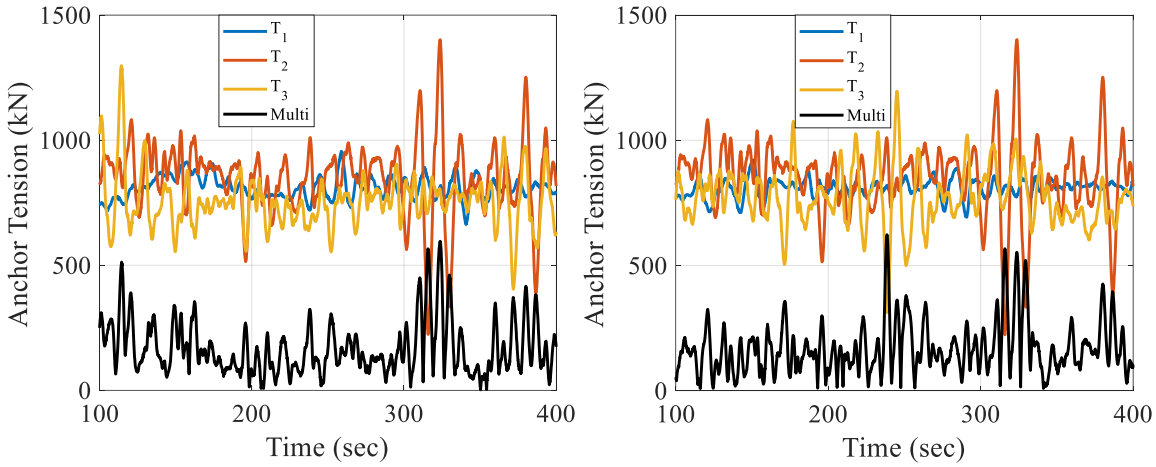

a.) Coherent waves b.) Independent waves

Figure 31: Time history snapshot of contributing line tensions and net multiline anchor force for H_s = 8 m, t_f = 14, and wave direction = 30° for a.) coherent and b.) independent waves

The effect of wave coherence is examined for both the 3-line and 6-line geometries, as shown in Figure 24. The difference in the multiline anchor force dynamics between the coherent and independent wave conditions is shown in Table 7, and which shows average values across the six realizations. The percent difference in the maximum value, mean value, and standard deviation of the net multiline anchor force for coherent and independent waves is calculated relative to the corresponding T_2 single line value. The maximum significant wave height is chosen based on Survival Load Case (SLC) conditions of the full-scale VolturnUS, a planned floating wind demonstration project in

the Gulf of Maine [44]. It should be noted that the 0 values in Table 7 are not absolute 0 values, but rather a result of rounding values <0.5 to one significant digit,

Table 7: Percent difference between coherent and independent value of net multiline anchor force, relative to T_2 single-line value. The intensity of shading reflects the magnitude of the percent difference for each value in question – maximum, mean, and standard deviation.

			3-Line Anchor									6-Line Anchor					
			0° Dir.			30° Dir.			60° Dir.			0° Dir.			30° Dir.		
			H_s (m)			H_s (m)			H_s (m)			H_s (m)			H_s (m)		
			4	8	12	4	8	12	4	8	12	4	8	12	4	8	12
Maximum (%)	t_f	11	2	4	0	3	-4	4	1	5	-2	-8	0	4	9	-11	9
		14	0	1	-1	1	5	0	2	0	1	-2	0	8	2	12	-1
Mean (%)	t_f	11	0	0	0	0	0	0	0	0	0	-1	0	2	1	0	0
		14	0	0	0	0	0	0	0	0	0	0	0	5	0	0	0
Standard Deviation (%)	t_f	11	1	0	0	8	1	0	5	-1	2	-10	-5	2	18	1	0
		14	0	0	0	3	0	0	0	1	0	-9	-3	6	7	-1	0

The lack of any consistent trend in the differences for the net multiline anchor tension suggest that the differences result primarily from natural randomness of the irregular wave fields, not from a difference in coherence versus regular wave loading. This lack of any trend was verified by repeating the analysis with six additional irregular wave realizations. Larger differences are seen in the 6-line anchor cases, as the duplicate wave effects are amplified by the presence of additional line attachments.

When examining multiline anchors forces, one of the most distinctive characteristics is the directionality of the force. In a single-line anchor system, only one mooring line is attached, therefore the anchor is loaded in one direction that varies by less than 1° for the OC4 floating system in any of the simulations completed. In a multiline anchor system, multiple mooring lines are attached, and the anchor is loaded in many different directions with many different force magnitudes. Therefore, a comparison must be made of the directionality of the net multiline anchor force between the coherent and

independent wave conditions, as shown in Table 8. This comparison is only shown for the 30° wave direction, because the duplicate wave effect renders the anchor force directionality for the other wave directions 1-dimensional - the direction of the net multiline anchor force in the 0° and 60° wave direction cases in the 3-line anchor system and the 0° and 30° wave direction cases in the 6-line anchor system fluctuate between the positive and negative value of the wave direction. Due to the exact symmetry of the loading in the direction perpendicular to the waves, y-components (y-direction being perpendicular to wave direction) of the contributing tensions cancel out perfectly due to the duplicate wave effect, therefore the direction of the multiline anchor force only varies back and forth in the exact direction of the waves. For the 30° wave direction case, which does not have any duplicate wave effects, the variation in the direction of the multiline force can be seen in Figure 32.

Table 8: Value difference of mean and standard deviation of direction of net multiline anchor force between coherent and independent conditions. The intensity of shading reflects the magnitude of the difference in value.

			Wave H_s (m)					
			2	4	6	8	10	12
Difference in Mean Direction of Net Multiline Anchor Force (°)	t_f	11	3	-2	-1	0	2	0
		12	4	-2	0	1	0	2
		13	3	0	0	1	1	0
		14	2	0	1	1	1	2

			Wave H_s (m)					
			2	4	6	8	10	12
Difference in Standard Deviation Direction of Net Multiline Anchor Force (°)	t_f	11	-3	5	2	0	-1	0
		12	-4	4	2	-1	0	-1
		13	-3	2	0	-1	-1	0
		14	-1	1	0	0	0	0

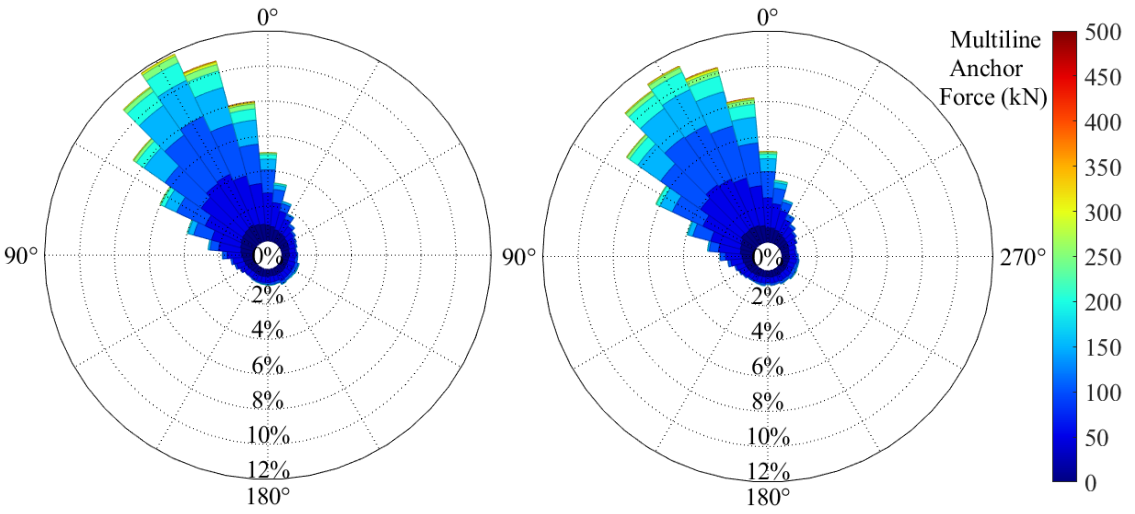

a.) Coherent (H_s = 6, t_f = 14)

b.) Independent (H_s = 6, t_f = 14)

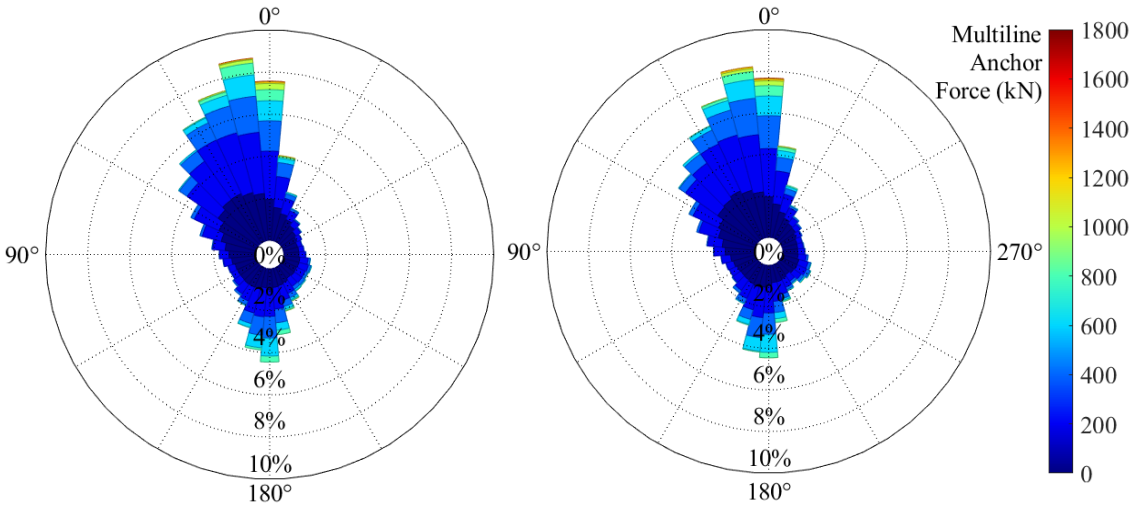

c.) Coherent (H_s = 12, t_f = 14)

d.) Independent (H_s = 12, t_f = 14)

Figure 32: Force direction rosettes for the net multiline anchor force in the 30° wave direction with H_s = 6 m and t_f = 14 for a.) coherent wave condition and b.) independent wave condition, and with H_s = 12 m and t_f = 14 for c.) coherent wave condition and d.) independent wave condition

As with Table 7, the lack of any consistent trend in the differences for the mean and standard deviation of the net multiline anchor force direction suggests that the differences result primarily from natural randomness of the wave fields. This lack of trend was again

verified by repeating the analysis with six additional irregular wave realizations. The lack of difference between the coherent and independent wave cases is also exhibited in the rosettes. While some of the rosettes not shown here exhibit slightly larger differences in shapes, there is still no consistency or trend in these small differences. This further bolsters the conclusion that the differences are a product of the natural dissimilarity between two different realizations of waves, not a difference due to the use of spatially coherent waves versus independent waves.

The smallness of the differences in the critical values of the net multiline anchor force reveal that spatial wave coherence does not have any significant effect on the dynamics of the net multiline anchor force, and that assumption of independence of the wave fields at different FOWT locations provides sufficiently accurate anchor load characterizations. This conclusion is of course of quite a different nature than that of regular waves in Section 3.2.2, and this difference is explained in Section 3.3.

3.3 Wave Coherence

The lack of difference between the coherent and independent wave results in the previous analysis suggests that wave coherence at connected turbines in a multiline anchor system is insignificant in determining multiline anchor force dynamics. The following section seeks to better understand and explain these results by focusing on only the waves and their characteristics and examining the distances at which wave elevations are no longer correlated enough to produce measurable synchronicity (or anti-synchronicity). The metric used here to determine the relationship of waves at different locations is the correlation coefficient between wave elevation time histories at different distances.

3.3.1 Regular Waves

Before examining realistic irregular waves, the correlation of regular waves is first presented. A regular wave, in the shape of a repeating sine wave, is shown in Figure 33.

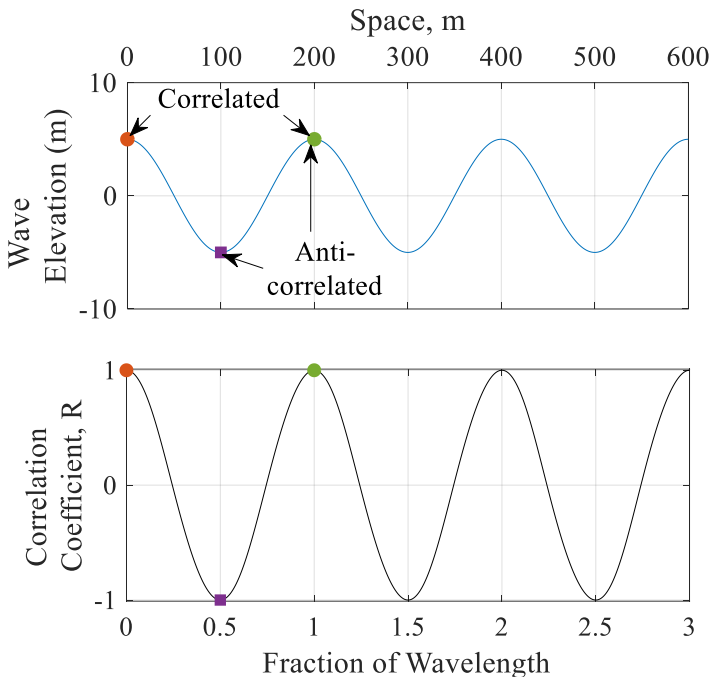

Figure 33: Wave elevation and correlation coefficient of a regular wave train with wave height of 10 m and wavelength 200 m

The relationship between wave elevation and space is expressed through the correlation coefficient, *R*, which is a measure of the strength and direction (positive or negative) of the linear relationship between two variables. For regular waves, at intervals of the wavelength, the correlation coefficient is 1, and the wave elevations at a time lag of one wave period are perfectly correlated. Conversely, at intervals of wavelength plus or minus one half, the correlation coefficient is -1, and the wave elevations at these points are perfectly anti-correlated. These characteristics can be seen in Figure 33, where the red and green markers are perfectly correlated, and the purple and green markers are

perfectly anti-correlated. With regular waves, each wave has an identical height, length, and period, therefore the location of and time between any of the crests and troughs can be perfectly and infinitely identified. With irregular waves in the following analysis, *R* serves as a measure of predictability for the locations of the crests and troughs of the waves.

3.3.2 1-Dimensional Irregular Waves

This section builds upon the previous section, with the goal of examining the correlation coefficient between irregular wave elevation time histories at different distances. Elevation time histories of irregular spatially coherent waves are generated via the procedures outlined in Equations (11) through (13), and each is generated over a distance of 7 peak spectral wavelengths for a 1-hour duration. Sections of a sample time history are shown in Figure 34.

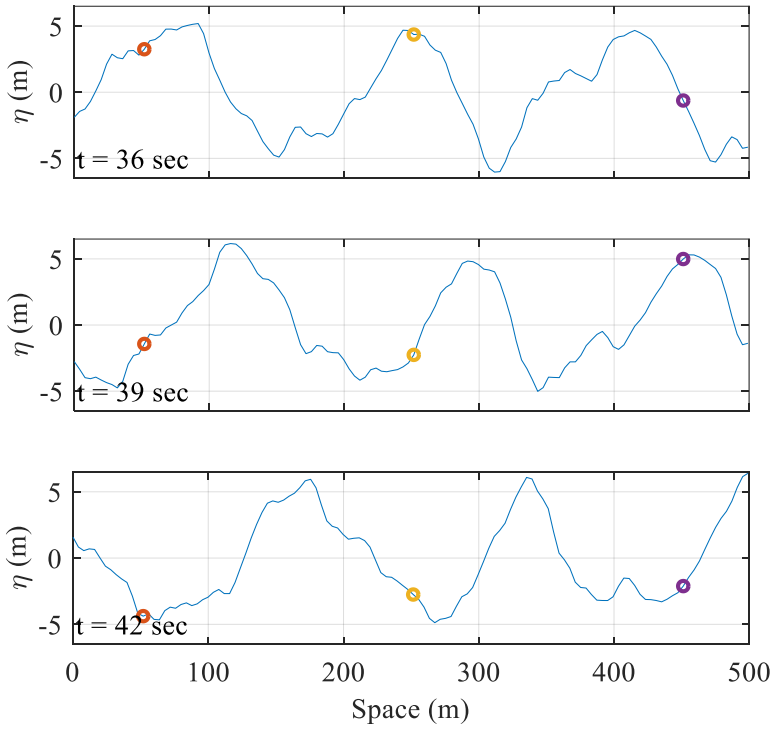

a.) Time snapshots of wave elevation in space

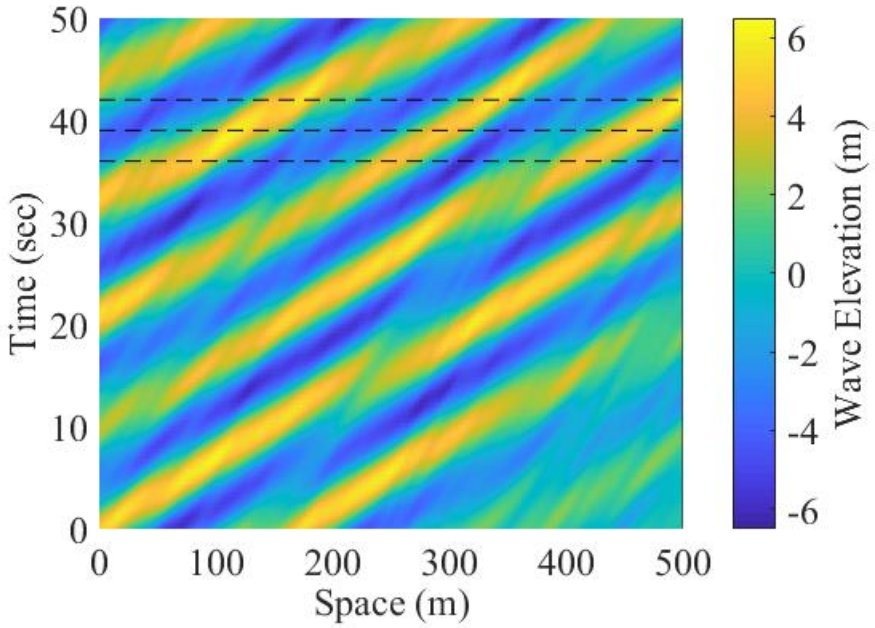

b.) Wave elevation versus space and time

Figure 34: a.) Time snapshots of wave elevation over space generated for different time instances and b.) wave elevation versus space and time. Example shown for significant wave height of 10 m, peak spectral wave period 11.3 sec, and peak spectral wavelength 200 m in water depth of 200 m. The markers in a.) are separated by a distance of 1 peak spectral wavelength, or 200 meters. The three subfigures in a.) correspond to the three dashed lines in b.)

Figure 34b reveals more clearly how quickly a specific wave moves in space, and how long it lasts in time. The colored ridges correspond to specific waves and show that larger waves generally last longer and travel faster than smaller waves (yellow ridges compared to green ridges). It can be observed that even the largest waves are only able to maintain themselves in the wave train no more than several hundred meters, which is far less than the any turbine spacings in Section 3.2.3.

Wave correlation relative to space and time can be calculated by

$$\boldsymbol{R(x) = \frac{cov(\eta(t,0),\eta(t,x))}{\sigma_{\eta(t,0)} \times \sigma_{\eta(t,x)}}} \qquad \textbf{(14)}$$

where R is the correlation coefficient of wave time histories at locations 0 and x, x is distance, t is time, η is wave elevation, σ is standard deviation, and cov is covariance. The correlation coefficient with distance is shown in Figure 35. It is important to note that the correlation coefficient is used over the space domain, as the interest lies in how wave elevation time histories at different locations correlate, not how a single wave propagates over time. Figure 35a shows the correlation coefficient of waves generated with the minimum recommended period, and Figure 35b shows waves generated with the maximum recommended period as designated by IEC offshore wind turbine design standards [60]. The relationship of correlation coefficient with distance is averaged across 18 realizations of the random process for each combination of significant wave height and peak spectral wave period.

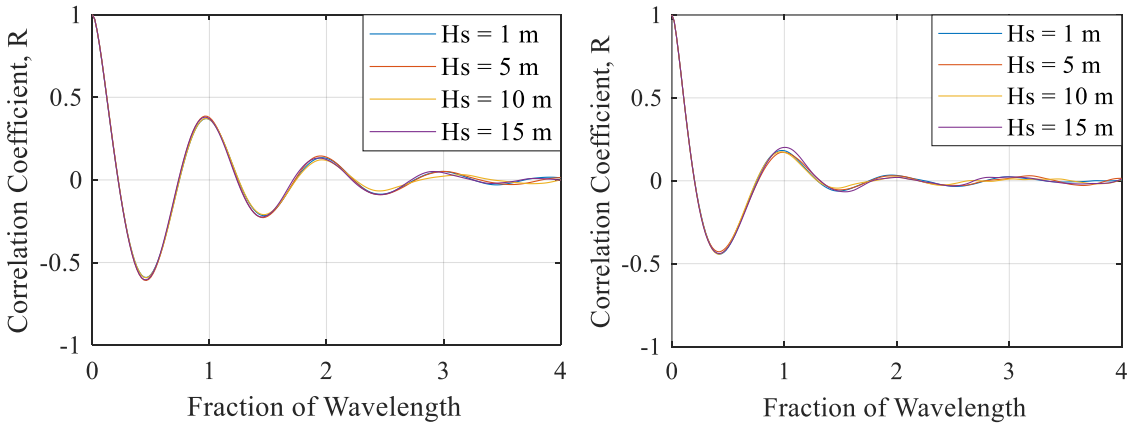

a.) $T_P = 11.1\sqrt{H_s/g}$ b.) $T_P = 14.3\sqrt{H_s/g}$

Figure 35: Correlation coefficient of irregular waves with space relative to number of peak spectral wavelengths for a.) maximum recommended peak spectral period and b.) minimum recommended peak spectral period

Similar to the regular waves, the correlation coefficient function still experiences peaks at intervals of peak spectral wavelength, but the magnitudes of the peaks decay with distance due to irregularity and loss of correlation of the wave train. These peaks at

intervals of peak spectral wavelength are used to fit an exponential decay function, as shown in Figure 36. The decay constant, C_d, measures how quickly the correlation coefficient approaches 0. This relationship is determined relative to distance (Figure 36) rather than fraction of peak spectral wavelengths (Figure 35) to allow for comparisons of C_d across different wave parameters. Correlation length, x_c, is defined as the distance x at which the correlation coefficient is equal to e^{-1}, or 0.368. A large decay constant means that the correlation coefficient decreases quickly (short correlation length), and a small decay constant means the correlation coefficient decreases slowly (long correlation length).

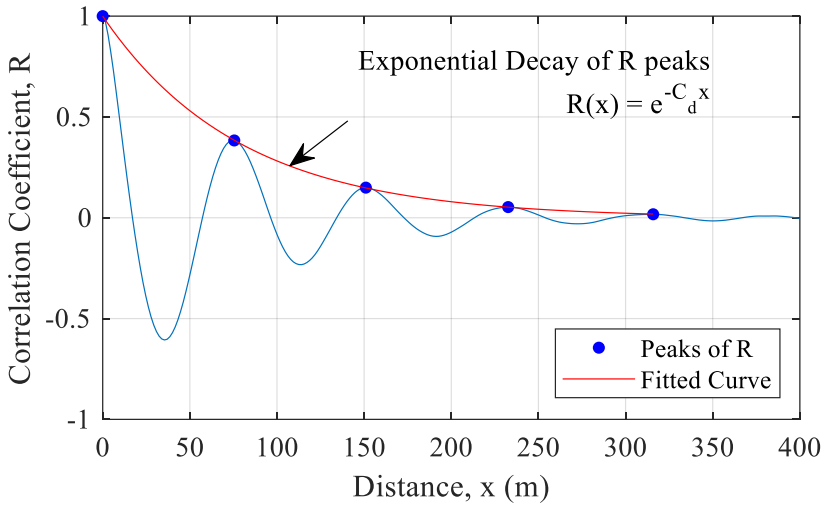

Figure 36: Exponential decay function fit for water depth = 200 m, H_s = 4 m, t_f = 11, and peak spectral wavelength = 77 m. Decay constant, C_d, is 0.0127 m^{-1} and correlation length, x_c, is 79 m.

This relationship can be expressed by

$$\boldsymbol{R(x) = exp(-C_d x) \text{ for } x = \lambda n} \qquad \textbf{(15)}$$

where R is the correlation coefficient between the wave elevation time history at a starting point and a wave elevation time history at a point n peak spectral wavelengths

away, x is distance from the starting point, C_d is decay constant, n is an integer, and λ is peak spectral wavelength.

A parametric study reveals how wave height (H_s), wave period factor (t_f), and water depth affect decay constant and in effect, correlation length. Parameter ranges are given in Table 9. Wave period factors (t_f) extend slightly beyond the recommended range of 11.1-14.3 given in IEC 61400 (2009) for modeling normal and extreme wave heights.

Table 9: Range of parameters for modeling spatially coherent irregular waves

	Range	Step Size
Water Depth (m)	50 - 500	50
Significant Wave Height, H_s (m)	1 - 12	1
Wave Period Factor, t_f	10 - 15	0.5

The relationship between input wave parameters and the correlation length can be seen in Figure 37.

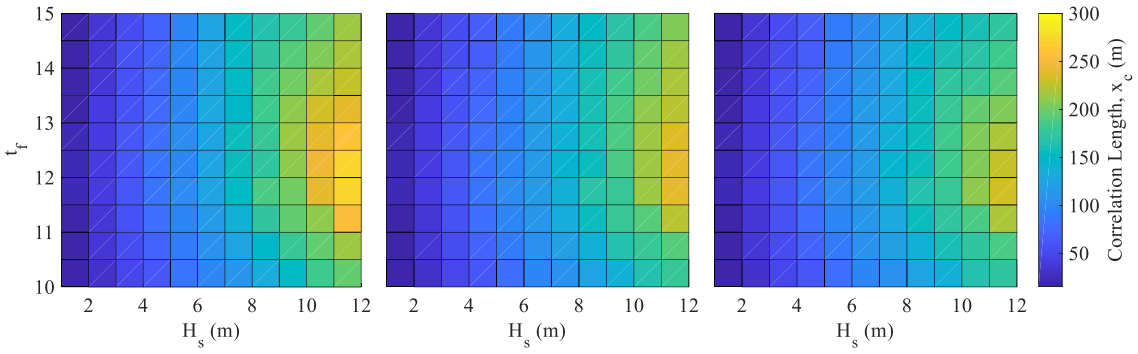

a.) 50 m water depth *b.) 100 m water depth* *c.) 500 m water depth*

Figure 37: Correlation length relative to wave parameters for a.) 50 m water depth, b.) 100 m water depth and c.) 500 m water depth

In general, it can be seen that wave correlation length increases with significant wave height. Water depth has a very small effect on the relationship between correlation

length and wave characteristics. The correlation length is largely independent of changes in wave period factor, except for very large wave heights. The maximum correlation length of 298 m occurs for water depth = 50 m, t_f = 11.5, and H_s = 12 m, where C_d = 0.0034. The minimum correlation length of 16 m occurs for H_s = 1 m and t_f = 10 for all water depths, where C_d = 0.0639.

Referring back to the multiline anchor analysis, for the maximum significant wave height of H_s = 12 m with t_f = 11 and water depth = 200 m, the minimum decay constant is 0.0042 and the maximum correlation length is 238 m. This correlation length is significantly smaller than any of the minimum turbine spacings in the multiline anchor layouts, as shown in Table 10.

Table 10: Correlation coefficient of waves at distances of minimum spacings in multiline configurations

Multiline Configuration	Wave Direction (°)	Minimum Turbine Distance in Direction of Wave Travel (m)	Minimum Decay Constant	Wave Correlation Coefficient at Minimum Turbine Distance
3-line	0	1257	0.0042	0.005
	30	725		0.048
	60	1257		0.005
6-line	0	417		0.174
	30	725		0.048

These very low correlation coefficients (<0.2) supplement the conclusion that spatial coherence of the waves at these distances does not have any significant effect on the multiline anchor force compared to the independent wave scenario.

Furthermore, the correlation coefficient decays faster in the 2-dimensional wave case than in the 1-dimensional wave case (Figure 38), and as a result, wave correlation lengths are shorter in the 2-dimensional case. Therefore, the use of 1-dimensional waves is a conservative choice in that, if there was any effect of spatial wave coherence on net multiline anchor force, it is expected that it would be revealed here. These 1-dimensional wave field results effectively allow the assumption that the 2-dimensional wave field would also not result in any difference between spatially coherent and independent wave loading at platforms connected to a multiline anchor.

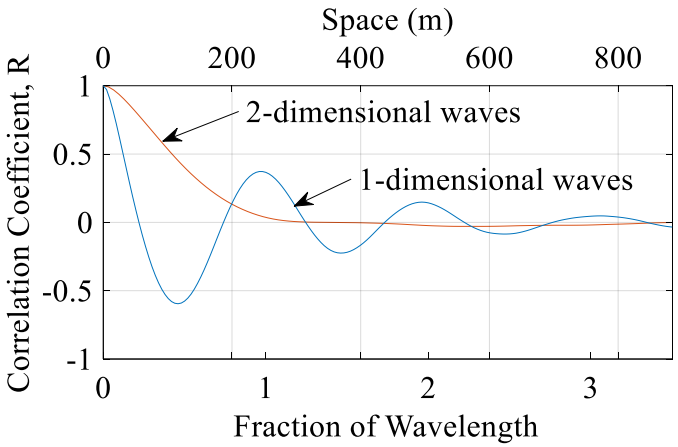

Figure 38: Correlation coefficient decay for 1-dimensional and 2-dimensional waves. Example shown for H_s = 12 m, t_f = 11.5, and depth = 200 m, which are the conditions that produce the largest wave correlation lengths in this study.

3.3.3 Minimum spacing of installed offshore wind turbines

The correlation lengths of this study are evaluated here in the context of typical spacing between turbines in installed offshore wind farms. While there is only one operational floating offshore wind farm, observations can still be made for the many installed fixed-

bottom wind farms. The following analysis of turbine spacing uses only wind farms that employ turbines with a 4MW or greater capacity, as deployment of commercial-scale floating wind technologies is likely to coincide with the progression to larger turbines [64]. The wind farms from this study exhibit a range of turbine capacities, farm sizes, and countries of origin, and all wind farms were commissioned within the past 10 years. It was found that most of the installed wind farms in this study have minimum turbine spacings between 4 and 8 rotor diameters, with fixed bottom wind turbine spacings ranging from 435 to 1072 m. Data for this study was obtained from 4C Global Offshore Wind Farms Database (2018), and details on the determination of turbine minimum spacings can be found in the Appendix.

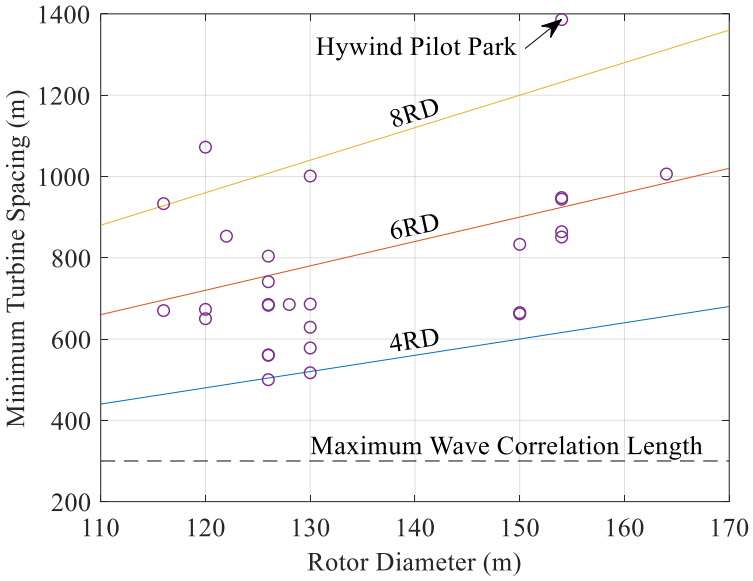

Figure 39: Turbine rotor diameter versus minimum turbine spacing for installed offshore wind farms

The first and only floating offshore wind farm as of writing this thesis, Hywind Pilot Park [66], employs the largest turbine spacing by a significant amount in terms of both total distance and number of rotor diameters. While no conclusions can be drawn from this

singular example of a floating offshore wind farm, it is still important to note the outlier nature of this point amongst the other offshore wind farms.

The most important conclusion to note is that the wave correlation lengths in Section 3.3.2 of this study (<300 m) are smaller than typical spacings of installed OWTs (>500 m), and anticipated spacings of other FOWTs. Even if the significant wave height in the correlation length study is increased to 18 m, the maximum correlation length is only 413 m, which is still smaller than any of the current spacings of most installed offshore wind farms using 4MW or larger turbines.

The idea of changing the mooring system and/or wave characteristics such that turbine spacings were less than or equal to the wave correlation length was considered. However, this was not feasible. From extrapolating the relationship between maximum correlation length and significant wave height in 200 m water depth, it was estimated that unrealistically large significant wave heights (H_s > 25 m, more than double the SLC value of H_s in the full-scale VolturnUS [44]) would be needed to create correlation lengths greater than the minimum turbine spacing in terms of rotor diameter of any currently installed offshore wind farms (Rotor Diameter =126 m, RD = 4.0, Spacing = 504 m).

3.4 Conclusions

This chapter investigated spatial characteristics of waves in the context of a multiline anchor system for floating wind turbines. The goal was to determine if multiline anchor force dynamics are a function of spatial wave coherence, or if the treatment of wave fields as independent at each turbine provides adequate load characterizations.

While regular waves fields in the multiline system showed the limits of what the difference in multiline anchor forces could be between these two models could be, the irregular wave fields applied to FOWTs in a multiline anchor system revealed no consistent trends that differentiated multiline anchor force dynamics generated by spatially independent versus coherent waves. Differences between the two wave loading models were insignificant – mean anchor force values differed by less than 1% and maximum anchor force values differed by less than 5% in the 3-line anchor system. A deeper investigation into spatial wave characteristics revealed that the correlation coefficient between wave elevation time histories at different points in space decays rapidly with distance between the points. Even for the maximum wave height studied (H_s = 12 m), the correlation length was less than 300 m.

The situation where wave coherence could potentially have an effect on multiline anchor force dynamics is one in which turbine spacing is less than or equal wave correlation length. It is almost certain that this situation is not feasible/possible for several reasons. First, in the context of turbine spacing, it is observed that spacing will likely not be less than 4 rotor diameters. This minimum spacing limit, coupled with the limit of floating turbines not being less than 4 MW capacity and 120 m rotor diameter, means that the absolute minimum spacing of FOWTs is likely to be at about 500 m. In combination with the findings in Section 3.3.3 that significant wave heights must be unrealistically large (H_s > 25 m) to produce wave correlation lengths of this distance, it can be concluded that a situation will not exist in which waves will be significantly correlated at the connected platforms in multiline anchor systems for FOWTs.

3.5 Appendix

Minimum turbine spacings were determined from Matlab image processing procedures, with images of offshore wind turbine locations taken from the 4C Offshore resource [65]. This is a public resource that provides a large amount of information about offshore wind farms. The map feature of this resource provides the location and layout of many fully commissioned offshore wind farms, as shown in Figure 40.

The use of this resource allows for the determination of turbine locations, and in effect, turbine spacings. The image in Figure 40a is first converted into matrix form using the *imread* function, then turbine locations are obtained using the *imfindcircles* function. These initial turbine locations are in terms of pixel distances, and the map scale key provided in for each wind farm was used to determine the number meters per pixel.

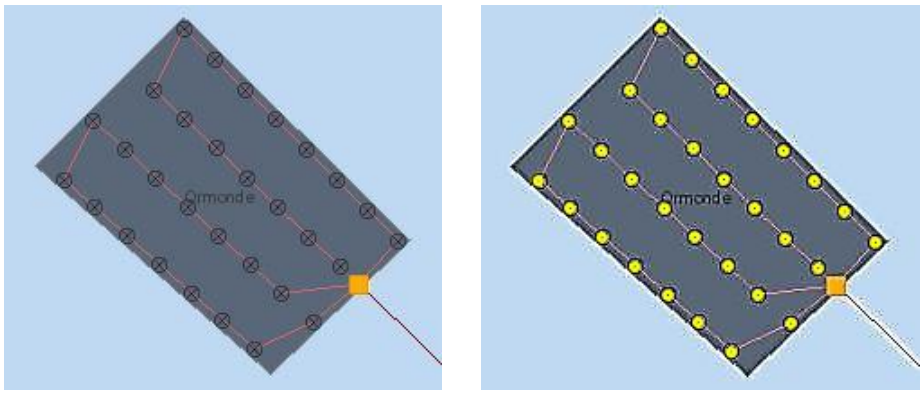

a.) Original image b.) Sharpened image with turbine locations

Figure 40: Image processing of map data from 4coffshore to obtain turbine locations

The minimum distance for grid-layout farms such as Ormonde offshore wind farm in Figure 40 is simple, but determining spacing for farms such as the Bard 1 Offshore Wind Farm in Figure 41 is more complex.

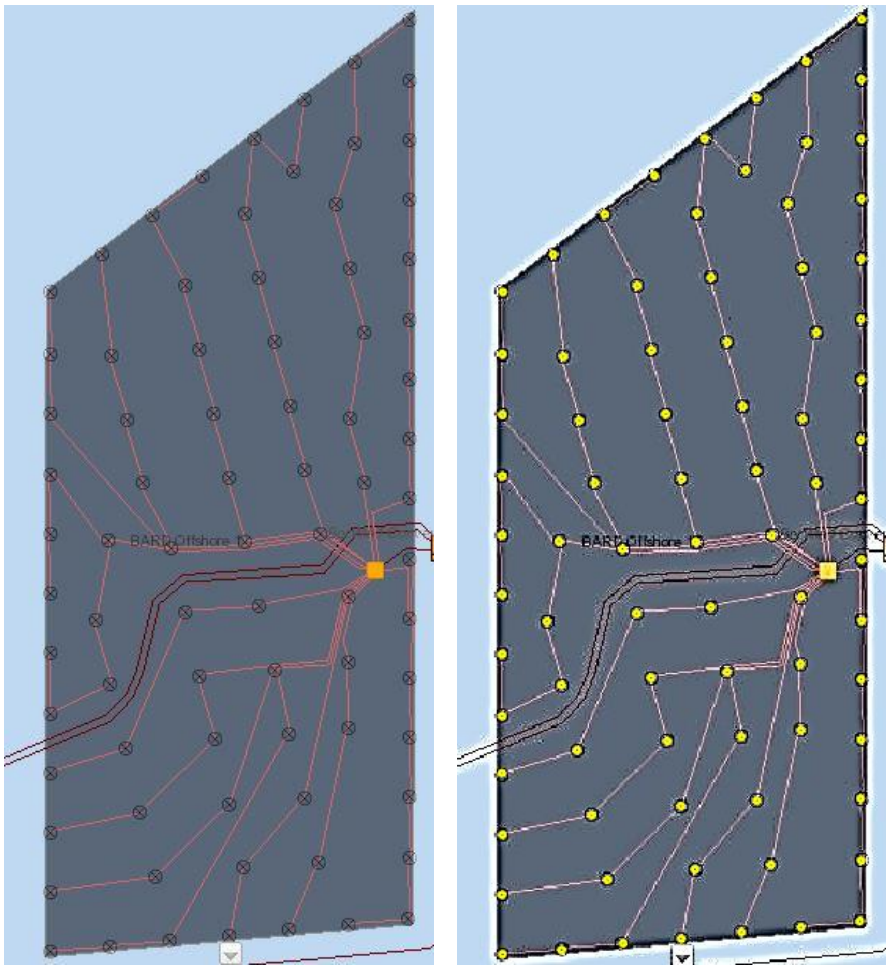

Figure 41: Inconsistent turbine spacing in Bard Offshore 1 wind farm

In cases such as this, where turbine layout lacks a pattern/grid and spacing is inconsistent, an alternate method is used to determine spacing. The Delanuay triangulation function in Matlab (*delaunayTriangulation*) is used to determine which turbines are the nearest neighbors for each turbine, and the distance of the nearest neighboring turbine in noted. The minimum spacing value for the farm is then taken as the average of these values for all turbines in the farm. Results for minimum turbine spacing are shown in Table 11.

Table 11: Turbine spacing of installed offshore wind farms. * indicates farms in which minimum turbine spacing was found in the literature. All others were calculated from the open-source map data on http://www.4coffshore.com/windfarms

Wind Farm	Year	Location	Turbine Capacity	Number of Turbines	Rotor Diameter	Minimum Turbine Spacing	RD

Alpha Ventus	2010	Germany	5	12	126	804	6.4
BARD Offshore 1	2013	Germany	5	80	122	853	7.0
Block Island Wind Farm	2017	U.S.	6	5	150	833	5.6
Borkhum Riffgrund 1	2015	Germany	4	78	120	673	5.6
Burbo Bank Extension	2017	U.K	8	32	164	1006	6.1
Dudgeon	2017	U.K.	6	67	154	851	5.5
Formosa	2017	Taiwan	4	2	120	1072	8.9
Fujian Putian City	2016	China	5	10	128	685	5.3
Gemini	2017	Netherlands	4	150	130	629	4.8
Global Tech I	2015	Germany	5	80	116	670	5.8
Gode Wind phases 1+2	2017	Germany	6	97	154	864	5.6
Hywind Pilot Park *[36]	2017	Scotland	6	5	154	1386	9.0
Huaneng Rudong North	2017	China	5	34	150	662	4.4
Huaneng Rudong South	2017	China	4	36	150	665	4.4
London Array *[67]	2013	U.K.	3.6	175	120	650	5.4
Longyuan Putian Nanri	2015	China	4	4	130	517	4.0
Nordsee One *[68]	2017	Germany	6.15	54	126	741	5.9
Nordsee Ost	2015	Germany	6.15	48	126	561	4.5
Ormonde *[69]	2012	U.K.	5.075	30	126	560	4.4
Race Bank	2018	U.K.	6	91	154	944	6.1
Sandbank1	2017	Germany	4	31	130	1001	7.7
SPIC Binhai North H1	2016	China	4	25	130	686	5.3
Tahkoluoto	2017	Finland	4	10	130	578	4.4
Thorntonbank I *[70]	2009	Belgium	5.075	6	126	500	4.0
Thorntonbank II	2013	Belgium	6.15	30	126	683	5.4
Thorntonbank III	2013	Belgium	6.15	18	126	685	5.4
Trianel Borkum I	2015	Germany	5	40	116	933	8.0
Westermost Rough	2015	U.K.	6	32	154	948	6.2

The wind farms that had literature containing spacing information were effective in verifying the image processing and turbine spacing calculation methods used for the majority of farms that do not publicly state minimum spacing values.

CHAPTER 4

APPLICATION OF THE MULTILINE ANCHOR CONCEPT IN AN EXISTING FLOATING OFFSHORE WIND FARM

4.1 Introduction

The floating wind industry is still in its nascence, and cost is one of the primary barriers to its development [14]. Given that the substructure of a floating turbine may account for almost one third of the total capital cost [32], it is important to address its structural efficiency. One way to increase the efficiency of the floating substructure is the implementation of a multiline anchor system, in which the FOWTs share anchors instead of each being moored separately (see Figure 42). This anchor-sharing multiline concept may result in less material usage, fewer anchor installations, and a reduced number of geotechnical site investigations required, resulting in an overall cost reduction of the anchor system. The multiline anchor concept has been investigated in several papers by the authors [23]–[31].

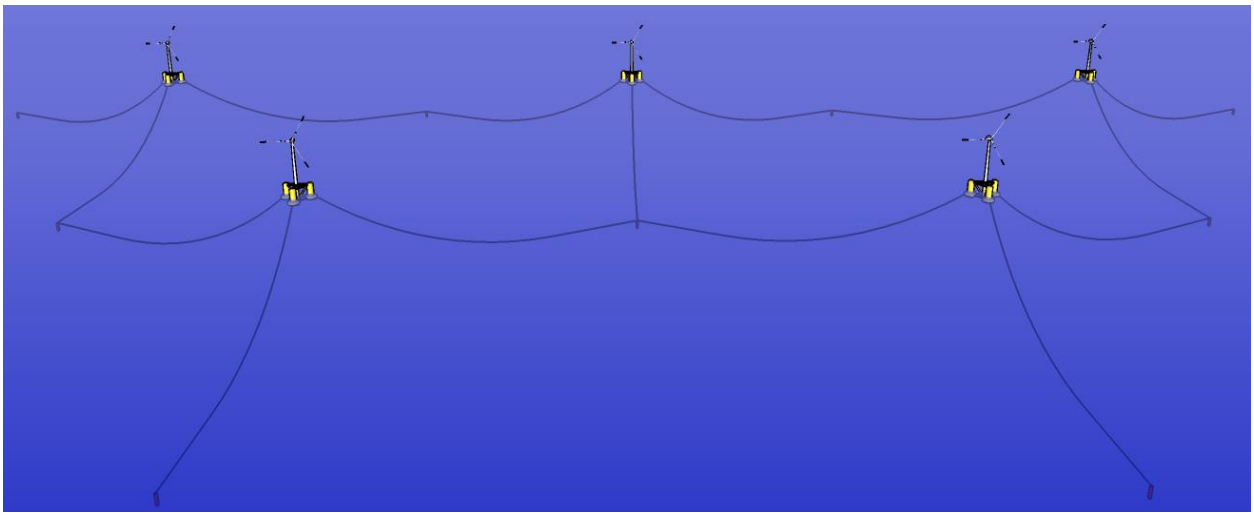

Figure 42: Example of multiline anchor concept for Hywind Pilot Park floating offshore wind farm configuration

Due to the interconnectedness of the multiline system, the turbine spacing and layout is an important factor in design and analysis. Previous work by the authors has made reasonable assumptions regarding these spatial characteristics, but the recent completion of the Hywind Scotland Pilot Park now provides the opportunity to analyze the multiline concept in the context of a real project. While there have been multiple single-turbine demonstration projects for floating offshore wind energy, the Hywind Pilot Park makes history as the first multi-turbine floating wind farm [71]. Statoil's Hywind Pilot Park is located 19 km off Peterhead, Scotland, and was commissioned in October 2017. It consists of five 6-MW turbines on floating spar buoys, and was installed in a water depth of approximately 100 m. An environmental report published by Statoil provides details on the installed turbine and anchor layout of the project, describing the differences in water depth between each turbine and between anchors connected to the same turbine [36]. This introduction of realistic variation in the water depth at the Hywind site is particularly valuable for the further investigation of multiline anchors, given that previous studies on the concept have assumed a uniform water depth across all turbines and anchors.

The goal of this Hywind Pilot Park case study is to examine the multiline anchor concept in the context of an existing real-world project and explore the differences between the single-line and multiline systems. In this chapter, the layout and water depths of the installed single-line system are detailed, then modified to obtain a multiline configuration. It should be noted that the layout of the installed Hywind project may differ slightly from the layout planned in the 2015 environmental report [36]. Following this initial evaluation of system geometry, an abbreviated mooring design is then carried

out for all five FOWTs in both the single-line and multiline configurations, noting assumptions and limitations of the process. Comparisons between the single-line and multiline anchor systems are made for mooring layout, mooring line lengths, anchor forces, direction of anchor forces, and anchor designs. A final comparison is made between the total amount of steel required for the single-line and multiline designs.

4.2 Layout Configurations

The first step in comparing the single-line and multiline systems for the Hywind project is the 2-dimensional layout orientation of the turbines, anchors, and mooring lines. These details for the installed single-line system are provided in the environmental statement of the Hywind Pilot Park [36], which contains turbine and anchor coordinates. The layout of the multiline system is obtained through rotation of the turbine mooring systems and modification of the turbine-anchor distances, while the positions of the five FOWTs kept constant. A uniform turbine spacing of 1386 m was used in the single-line configuration, therefore the transformation of the system to a multiline configuration yields uniform radial turbine-anchor distances of 800 m. The comparison of the 2-dimensional layout of the single-line and multiline system is shown in Figure 43.

The Hywind Pilot Park environmental document also lists the water depth at the single-line anchor points. This water depth data was used to generate a continuous water depth contour map, using thin-plate spline interpolation between the 15 data points [72]. The continuous water depth map over the area of the wind farm is then used to determine water depth at the turbine locations and water depth at the multiline anchor locations for use in the mooring design process.

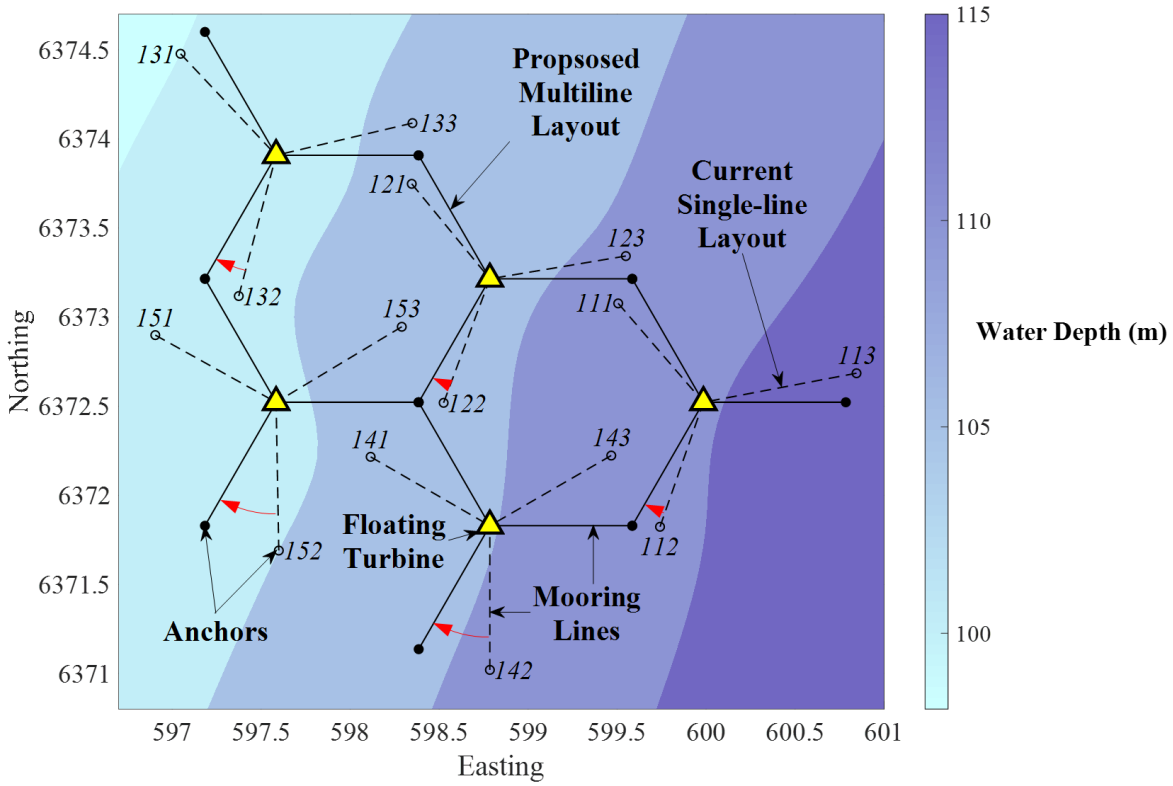

Figure 43: 2-dimensional layout of turbines and anchors for the installed single-line and proposed multiline configuration. Contours indicate water depth. Red arrows indicate the rotation of the mooring systems from the single-line to multiline configuration. Anchor numbers will serve as a legend for the remaining sections of the chapter.

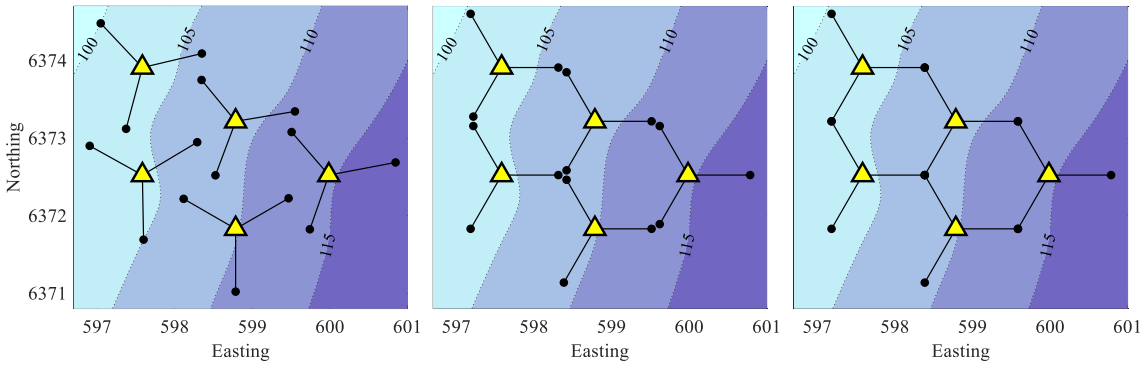

a.) b.) c.)

Figure 44: Diagrams of the a.) Single-line anchor locations, b.) Single-line anchor locations of the multiline anchor layout and c.) multiline anchor locations.

Figure 43 reveals that very little modification of the 2-dimensional mooring system layout is needed to obtain a multiline configuration. Rotations of the lines from their

original single-line to proposed multiline orientations range from 9 to 31 degrees. Since the locations of the anchor points are similar between the single line and multiline configurations, the depth at the anchor points is also largely unchanged - difference in depth for each anchor between the current single-system and the proposed multiline system ranges from 0.1 to 1.9 m.

Orientation of a 3-line catenary mooring system often aims to align a mooring line in the direction of the prevailing wind, such that the mooring system is stiffest against the wind and the platform displacement is minimized [12]. This is consistent with the mooring layout of the Hywind project - the wind predominantly comes from the southwest (Figure 3, Statoil, 2015), and the turbines have a mooring line generally aligned upwind with this direction. This alignment characteristic continues to be satisfied in the reoriented multiline configuration; there is in fact a slightly better alignment of the upwind mooring line with the wind direction (Figure 43). Given that the rotations the mooring systems are small, and mooring line alignment with the direction of wind origination is consistent, it can be assumed that the modified multiline system is still an appropriate and realistic layout.

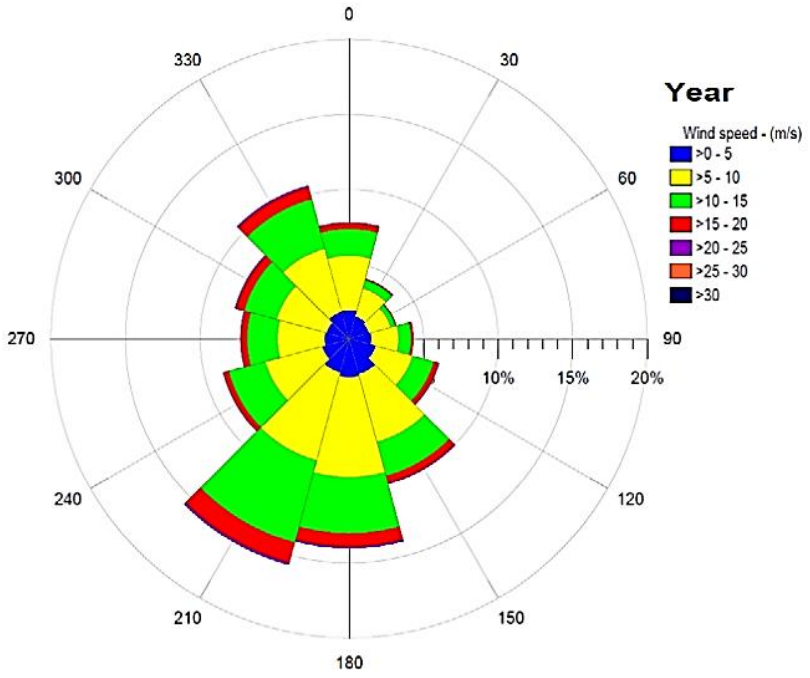

Figure 45: Wind speed and direction rosette for Hywind Scotland Pilot Park site [36]

The comparison of the 2-dimensional layout for the installed single-line and proposed multiline configuration is summarized in Table 12.

Table 12: 2-dimensional layout comparison for single-line and multiline system

	Single-line	Multiline
Turbine spacing	1386 m	1386 m
Water depth at anchors	100 – 117 m	100 – 117 m
Radial distance from turbine to anchor	691 – 875 m	800 m
Angle between mooring lines	118 - 122°	120°

4.3 Mooring & Anchoring System Design

The mooring and anchoring systems of this chapter are designed based on the geometric layout and water depths of Equinor's Hywind Scotland project. In place of the

6-MW turbines supported by spar buoys used at Hywind Scotland, the NREL 5MW turbine and the associated DeepCwind semisubmersible floating system are utilized, since both are open source and freely available for academic research and publication.

4.3.1 Turbine & Platform Models and Simulation Software

The dynamics of the FOWT system are modeled with the National Renewable Energy Laboratory's FAST (Fatigue, Aerodynamics, Structures, and Turbulence) Code. FAST v8 is a comprehensive, fully-coupled aero-hydro-servo-elastic simulator capable of predicting motions and loads in the time domain [37], [38]. The NREL OC4-DeepCwind semisubmersible system used in this study was developed for a 3-line catenary mooring system like the Hywind spar, but has a much shorter draft, making it suitable in shallower water depth. Furthermore, the OC4-DeepCwind platform employs the most commonly studied platform type (semisubmersible) in current FOWT technology/concepts [32], therefore it is still a realistic choice for investigating the multiline concept in the context of a real project. Details on the OC4-DeepCwind system can be found in Robertson et al. (2014). One of the primary differences between these two platform types is that the a semisubmersible platform is dominated by surge motions, while a spar platform is dominated by pitch motions [32]. The implications of this difference in platform-type relative to the results will be discussed in later sections. Furthermore, the NREL 5-MW reference turbine was used instead of Hywind's 6-MW turbine, again due to the public availability of the model.

4.3.2 Mooring Design

The turbine and platform models are consistent between the single-line and multiline system, but the differences in the spatial layout of the anchors as described in

Section 4.2 (Figure 43) are what create the differences in the mooring systems and anchor forces. Mooring design for each of the five turbines in the single-line and multiline systems was carried out in general accordance with the American Bureau of Shipping standards [41]. The chain size and mooring line lengths were developed from a simplified mooring design regime, to prevent time-domain design in FAST from becoming prohibitive in computational expense.

The Hywind project environmental statement states a mooring chain size range of 100-160 mm [36], so a mooring chain size of 130 mm is selected and held constant for all designs. This intermediate chain size was chosen initially as a test, then verified in the design process to be adequate for all mooring designs. The mooring systems were designed for only Ultimate Limit State, and were not evaluated for the Fatigue and Accidental Limit States. The three critical design load cases selected to analyze the Ultimate Limit State are explained in Section 4.3.3 (Table 13). Lastly, the quasi-static mooring model MAP [73] is used due to its capability of simulating varying water depth at the anchors for the same turbine.

Performance criteria to be met by the catenary mooring designs are governed by American Bureau of Shipping (2014) and are as follows:

1.) Average maximum line tension does not exceed the factored minimum breaking strength of the line (FS = 2.0 for DLC 1.6 and DLC 6.1, FS = 1.05 for SLC)
2.) Maximum platform offset does not exceed 20% of the turbine's water depth
3.) No vertical uplift force at the anchor

In 2.), the 20% water depth limit is chosen based the platform offset limits discussed in Campanile, Piscopo, & Scamardella (2018).

4.3.3 Environmental Conditions

Candidate mooring systems must be subjected to a range of environmental loading conditions to verify the adequacy of the designs. While some environmental conditions were provided in the Hywind Environmental Statement [36], the large wave heights of these given conditions were physically incompatible with the turbine and platform model used in this study. For example, the 50-yr significant wave height of 19.7 m [36] resulted in wave heights as large as 27 m during the simulations, which intersected with the bottom of the rotor swept area of the NREL 5MW/DeepCwind model and prevented the simulation from completing normally. As a result, the Gulf of Maine conditions were used instead, as this site has a similar water depth to the Hywind Project of roughly 100 m, and possesses thorough environmental data. The wind, wave and current (WWC) parameters at this site for the three selected critical environmental conditions are taken from the full scale VolturnUS project [44], harvested from over ten years of buoy data at a site off Monhegan Island, Maine [45], [46]. Details of these load cases are provided in Table 13 [43].

Table 13: Environmental conditions used for mooring design (*50-yr significant wave height conditioned upon rated wind speed)

Load Case	DLC 1.6	DLC 6.1	SLC
Conditions	Extreme Operating	Extreme Non-Operating	Survival Non-Operating
Wind Speed at Hub Height	11.4 m/s (rated)	40 (50-yr)	45 m/s (500-yr)
Turbulence Intensity	10%	10%	10%
Significant Wave Height	8.0 m (50-yr*)	10.2 (50-yr)	12 m (500-yr)
Peak Spectral Wave Period	12.7 sec	14.1 sec	15.3 sec
JONSWAP Gamma Factor	2	2.5	2.5
Current Speed	0.30 m/s	0.45 m/s	0.55 m/s

The wind speed in DLC 1.6 of 11.4 m/s is the rated wind speed of the NREL 5-MW reference turbine that produces peak thrust [35], as designated in American Bureau of

Shipping [41]. The turbulent wind field is generated with a Kaimal spectrum an 10% turbulence intensity via Turbsim [47]. Waves are generated with a JONSWAP spectrum, and wave heights are Rayleigh distributed [48]. Current is steady and equal at each FOWT. Six 1-hour simulations using different random seeds were completed for each combination of load case and WWC direction, as designated in the IEC design standards [60].

For each turbine, six co-directional WWC directions were analyzed during the design process, and these directions were specific to each turbine's mooring layout, aligned either directly with a mooring line or halfway between two mooring lines. Applying a WWC direction in which a mooring line is directly upwind is likely to produce peak tensions and minimum lay lengths for that line (see 1. and 3. of Section 4.3.2), and applying a WWC direction directly in between two mooring lines is likely to produce maximum platform offset (see 2. of Section 4.3.2). This full range of WWC directions from 0° - 360° is necessary due to the asymmetry of each turbine's mooring system: a turbine may have each of its 3 anchors at different depths, and in the single-line system each anchor may be at a different distance from the turbine.

Wind and waves were modeled as independent at each turbine, and wind wake effects were not considered. As a rule of thumb, wind wake effects can be neglected when the turbines are spaced more than 10 rotor diameters apart [49]. The 1386 m distance between turbines and use of the NREL 5-MW turbine with a 126 m rotor diameter results in a spacing of 11 rotor diameters apart, therefore this condition for non-inclusion of wind wake effects is satisfied. However, the real Hywind Project with the 6-MW turbines (154 m rotor diameter) has turbine spacing of 9 rotor diameters. The effect

of wind wakes relative to multiline anchor system forces is still an ongoing topic of investigation by the authors. The choice of independent wave fields at the turbines is justified by the author's previous studies, which reveal that spatial coherence of wave fields is insignificant for typical offshore wind turbine spacings. The insensitivity of multiline anchor forces to wave coherence was investigated specifically for the OC4-DeepCwind system in Fontana et al. (2017).

4.3.4 Soil Conditions and Anchor Design

Using some of the soil details provided in the Hywind Environmental Statement (2015), a two-layer soft clay soil profile was developed and utilized, as detailed in Table 14.

Table 14: Soft clay soil profile details used in anchor design

Depth	< 5 m	> 5 m
Soil Type	High plasticity silt	Low plasticity clay
Water Content	100%	40%
Unit Weight	14.3 kN/m^3	17.4 kN/m^3
Undrained strength at top of layer	1.4 kPa	6.4 kPa
Linear strength increase rate	0.92 kPa/m	1.61 kPa/m
Overconsolidation ratio	1	1
Undrained shear strength sensitivity	6	6

Suction caisson type anchors are designed for the mooring system, consistent with the installed Hywind Project. FAST simulations treat the anchor as a fixed point at the seabed surface, but a real suction caisson connects the mooring line and anchor through a reverse catenary geometry below the seabed. For the purposes of this study, the padeye is assumed to be at 2/3 of the caisson embedment depth and the method of Neubecker and Randolph is used to determine the reverse catenary geometry and reduction in mooring

line tension due to friction [75]. In addition, a soil-mooring line adhesion factor (α) of 0.7 is assumed.

After the components of the mooring line tension at the padeye are obtained, the caisson design is computed based on the outside diameter, embedment depth, and soil properties following the method of Murff and Hamilton (1993), Aubeny (Aubeny et al., 2003), and Aubeny and Murff (2005). This method is based on the upper bound plasticity and accounts for inclined loading. Furthermore, a capacity reduction of 5% is incorporated to account for vertical and horizontal misalignment. In this design process, the two-layer soil profile shown in Table 14 is represented by an equivalent single layer profile with linearly varying strength.

A safety factor of 1.5 is applied to the padeye demand, and the outside diameter and embedment depth of the caisson are selected such that an adequate safety factor is provided with as little excess capacity as possible [41]. In a final design check, self-weight penetration of the caisson is calculated followed by a comparison of suction needed to complete installation to suction that would cause plug heave failure. The installation check is completed with a safety factor of 1.5 (American Bureau of Shipping, 2015). The suction capacity required for installation is calculated as sum of the skin friction between the soil and the interior and exterior surfaces of the caisson and the bearing capacity along the circumference of the leading edge of the caisson. The effective length of the caisson to be used in load capacity estimates is taken as the physical length of the caisson minus the predicted plug heave [76].

4.4 Results and Comparison

The single-line system and the multiline system differ both in the spatial layout of the anchors and in the number of lines attached per anchor. Therefore, it is best to analyze the results in stages that single out one difference at a time, before analyzing the final systems. The first stage focuses only on differences in the spatial layouts, by comparing the 15 anchor designs of the single-line system and the 15 anchor designs for the single-line force components of the multiline system. The second stage focuses on differences due to multiple line attachments, by comparing the anchors designed for net multiline forces to anchors designed for the single-line contributing forces in the multiline system. The final stage is the most important analysis, comparing the 15 anchors in the single-line system and 9 anchors in the multiline system.

Before analyzing the mooring and anchor design results, there are several important characteristics of the floating systems that must first be discussed. The first characteristic is the nonlinearity of catenary mooring dynamics, which results in a high sensitivity of catenary mooring response to the small changes in spatial geometry between the single-line and multiline layout. For example, for a 100 m water depth and 800 m turbine-anchor distance in a static configuration, a decrease in mooring line length from 770 m to 765 m results in a lay length decrease from 388 m to 267 m and an anchor force increase from 1,206 kN to 3,277 kN. More details on the nonlinearity of catenary mooring response can be found in Barltrop (1998). The second characteristic is the sensitivity of the three mooring lines on a turbine to each other. In other words, the system response of a turbine's mooring system is a function of all three of its line

geometries and designs, therefore each individual line/anchor cannot be compared independently to its single-line or multiline counterpart

4.4.1 Mooring Lines

Given that the chain size and weight is kept constant across the single-line and multiline systems, the mooring designs are compared in terms of total mooring length and weight. Table 15 reveals that the two systems are similar to each other in this sense.

Table 15: Mooring design of single-line and multiline systems

	Single-line	Multiline
Chain size	130 mm	130 mm
Chain weight in air	338 kg/m	338 kg/m
Total Line length	11,310 m	11,541
Total Line weight	3,823 tonnes	3,901 tonnes

The multiline layout requires 2% more line length than the single line layout. This slightly larger total line length in the multiline system is a result of the slightly larger radial distances from turbine to anchor; the average radial distance from turbine to anchor in the multiline system (800 m) is proportionally 2% greater than the average radial distance from turbine to anchor in the single-line system (784 m). The difference in the average water depth at the anchors is negligible between the single-line and multiline systems and has no significant effect on the differences in total mooring weight. More precise details on the mooring design inputs and results can be found in Table 16.

4.4.2 Single-line values in the Single-line and Multiline Layouts

The 15 anchor designs of the single-line system and the 15 anchor designs of the single-line components of the multiline system are compared in Table 16, and the legend for interpreting these results is provided in Figure 43. The mean anchor weight for the single-line system (57 tonnes) is 4% lower than the mean anchor weight for the single-

line components of the multiline system (59 tonnes). This negligible difference between the single-line systems allows for a simpler comparison of the 15-anchor single-line system and 9-anchor multiline system in Section 4.4.4.

Table 16: Mooring design inputs and results. Note: "Multiline Config" describes single-line values of system arranged in multiline layout. The suction caissons were designed for L/D = 3 and wall thicknesses of t = D/144. This resulted in diameters (D) ranging from 4.8 – 5.6 m and embedment lengths (L) ranging from 14.3 - 16.7 m.

	Water Depth (m)		Radial Distance (m)		Line Length (m)		Max Force (kN)		Max Offset (m)		Anchor Weight (tonnes)	
Line/ Anch.	**Single-line Config**	**Multi-line Config**	**Single-line Config**	**Multi-line Config**	**Single-line Config**	**Multi-line Config**	**Single-line Config**	**Multi-line Config**	**Single-line Config**	**Multi-line Config**	**Single-line Config**	**Multi-line Config**
A111	112	112	733	800	713	770	5,410	6,263			44	51
A112	114	113	740	800	720	772	5,338	6,145	22	12	44	50
A113	117	117	875	800	838	775	5,121	5,905			42	48
A121	106	106	691	800	667	767	7,060	7,501			58	61
A122	108	107	743	800	713	769	6,932	7,413	15	12	57	61
A123	111	112	775	800	742	772	6,750	7,221			55	59
A131	100	100	783	800	750	765	8,241	8,126			67	66
A132	104	103	825	800	789	768	7,930	7,937	14	12	65	65
A133	106	106	787	800	759	770	7,851	7,782			64	64
A141	106	107	774	800	744	768	7,250	7,120			59	58
A142	111	109	809	800	777	769	6,972	7,056	13	12	57	58
A143	113	113	788	800	761	773	6,888	6,810			56	56
A151	102	103	777	800	749	767	7,940	7,901			65	65
A152	105	103	832	800	796	767	7,754	7,899	14	11	63	65
A153	107	107	824	800	792	770	7,620	7,695			62	63

Consistent with the general behavior of mooring systems, the deeper water anchors generally have smaller forces/anchors, and the shallower water anchors generally have larger forces/anchors due to the nature of restoring forces in the suspended lines [77].

4.4.3 Single-line values and net values in the Multiline Layout

The comparison of anchor weights between the single-line components of the multiline system and the net multiline system are shown in Figure 46. It can be seen that

the net multiline anchor weight is always lower than the maximum contributing single-line anchor weight. Since the anchors with more than one line attached have force componenents in opposite directions, force cancellation occurs, lowering the maximum anchor force value used in design. The most dramatice example of this effect in the 3-line anchor, where the anchor design weight for the net multiline force is 23% lower than the anchor design weight for the maximum contributing single-line force.

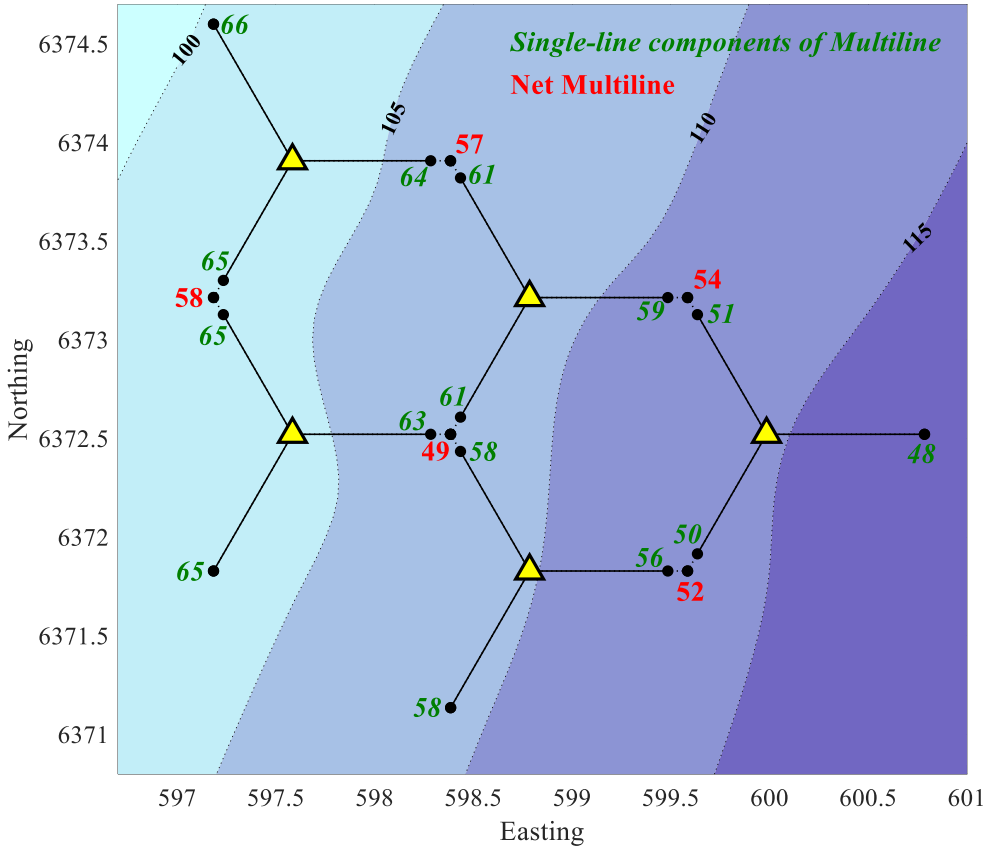

Figure 46: Anchor design weights for the single-line components of multiline layout and net multiline forces. Weights are in units of metric tonnes.

Although there are a limited number of anchors in the 5-turbine multiline farm from which conclusions can be drawn, it can be seen in Table 17 that the more lines are attached, the smaller the anchor required.

Table 17: Reduction in anchor size with addition of line attachments in multiline layout. *It should be noted that there is only one 3-line anchor in this configuration from which values are computed.

	1-line anchors	2-line anchors	3-line anchor*
Mean anchor weight (tonnes)	59	55	49
Average percent reduction in anchor weight, relative to anchor designed for average of contributing single-line forces	-	6%	20%
Average reduction in anchor weight, relative to anchor designed for maximum of contributing single-line forces	-	9%	23%

4.4.4 Single-line and Multiline Anchor Designs

The comparison between the 15 anchor weights in the single-line system, the 15 anchor weights of the single-line components of the multiline system, and the 9 anchor weights in the net multiline system is shown in Table 18 and Figure 47. This comparison is additionally summarized in Table 19.

Table 18: Comparison of anchor sizes for the single-line system, the single-line components of multiline system, and the net multiline system

Single-line Anchor Size (tonnes)			**Multiline Anchor Size (tonnes)**	
Single-line Anchor	**Single-line Configuration**	**Multiline Configuration**	**Multiline Configuration**	**Multiline Anchor**
A111	44	51	54	**A111_A123**
A123	55	59		
A112	44	50	52	**A112_A143**
A143	56	56		
A113	42	48	48	**A113**
A121	58	61	57	**A121_A133**
A133	64	64		
A141	59	58	49	**A141_A122_A153**
A122	57	61		
A153	62	63		
A131	67	66	66	**A131**
A132	65	65	58	**A132_A151**
A151	65	65		

A142	57	58	58	**A142**
A152	63	65	65	**A152**

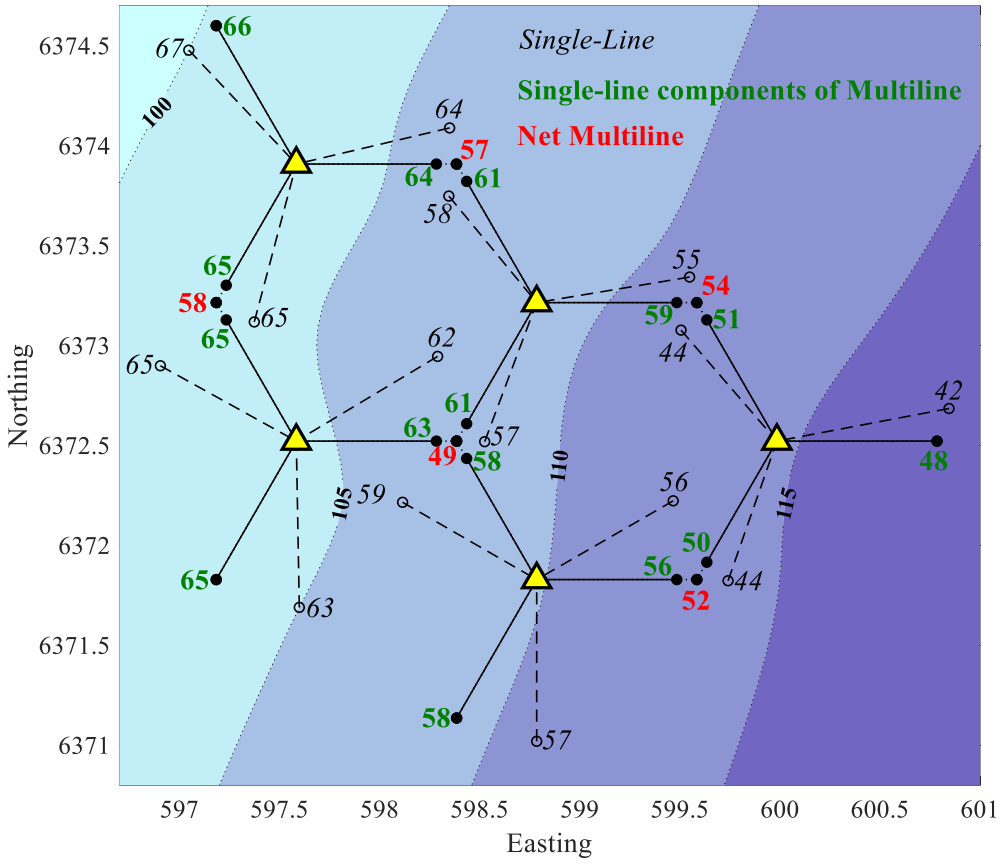

Figure 47: Anchor design weights for the single-line layout, single-line components of multiline layout, and net multiline forces. Weights are in units of metric tonnes.

Table 19: Anchor design results

	Single-line	**Multiline**
Number of 1-line anchors	15	4
Number of 2-line anchors	0	4
Number of 3-line anchors	0	1
Total number of anchors	15	9
Total Anchor Steel Weight	860 tonnes	507 tonnes

The anchors in the multiline system are slightly smaller than the anchors of the single-line system - the average anchor weight in multiline anchor system (56 tonnes) is 2% lower than the average anchor weight in the single-line system (57 tonnes). However, the total weight of the anchor system is drastically reduced in the multiline layout by 41%.

This reveals the most important conclusion of this section - the reduction in total anchor steel weight required for the multiline system results almost entirely from the reduction in number of anchors, while the slight decrease in anchor size due to force cancellation has an insignificant effect in comparison.

The mooring line weight of the multiline system is slightly higher than that of the single line system, but the reduction in anchor weight due to the multiline configuration results in a total system weight that is 6% lower than the single-line system. Although this reduction in steel weight is small, there may sizable reductions in other expenses related to the support structure. If it is assumed that the anchor installation and site investigation costs are proportional to the number of anchors, it may be suggested through extrapolation that a reduction in these costs approaching 40% may be realized for the multiline system as well. This assessment is supported by the standard for Support Structures of Offshore Wind Turbines states that for multiple foundations such as in a wind farm, the soil stratigraphy and range of soil strength properties shall be assessed per foundation location [78]. Furthermore, the recommended practice for Offshore Soil Mechanics and Geotechnical Engineering requires a minimum of one detailed geotechnical investigation at each anchor site, stating that at a final stage, the soil investigation should provide all necessary data for a detailed foundation design of a specific structure at the specific location [79].

4.4.5 Directionality of Multiline Anchor Force

This section seeks to understand how the directionality of the multiline anchor force is affected by the number of lines and by the water depth difference between the connected turbines. It also seeks to support previous findings on multiline anchor

directionality, which showed that the mean direction of the multiline anchor force is aligned with the WWC direction and that wave dominated load-cases result in larger standard deviation and range of force direction on a multiline anchor [23]. Anchors 113, 131, 142, and 152 are conventional single-line anchors within the multiline configuration, therefore they only experience force applied in one single direction and will not be further discussed in this section. The codirectional WWC directions referenced in the following figures and tables of this this section are based on the coordinate system of Figure 45.

First, the multiline anchor force direction is assessed relative to the number of line attachments. The four 2-line anchors in the multiline configuration have a range limited by the geometry of the line attachments. Assuming relatively small turbine displacements and no uplift, mooring lines are only able to apply tension in one direction, therefore the resultant 2-line anchor force direction is always within the 120° between the line attachments. The 3-line anchor in the system is the only anchor that may have force applied in any direction. This difference in the force direction range between the 2-line anchors and the 3-line anchor can be seen in Figure 48. While only the SLC load case with a 330° WWC direction is shown in Figure 48, this behavior is present in all load cases and WWC direction. In general, the 3-line anchor has a larger force directional range and smaller forces than the 2-lines anchors, and this characteristic is present across all load cases and WWC directions of this study.

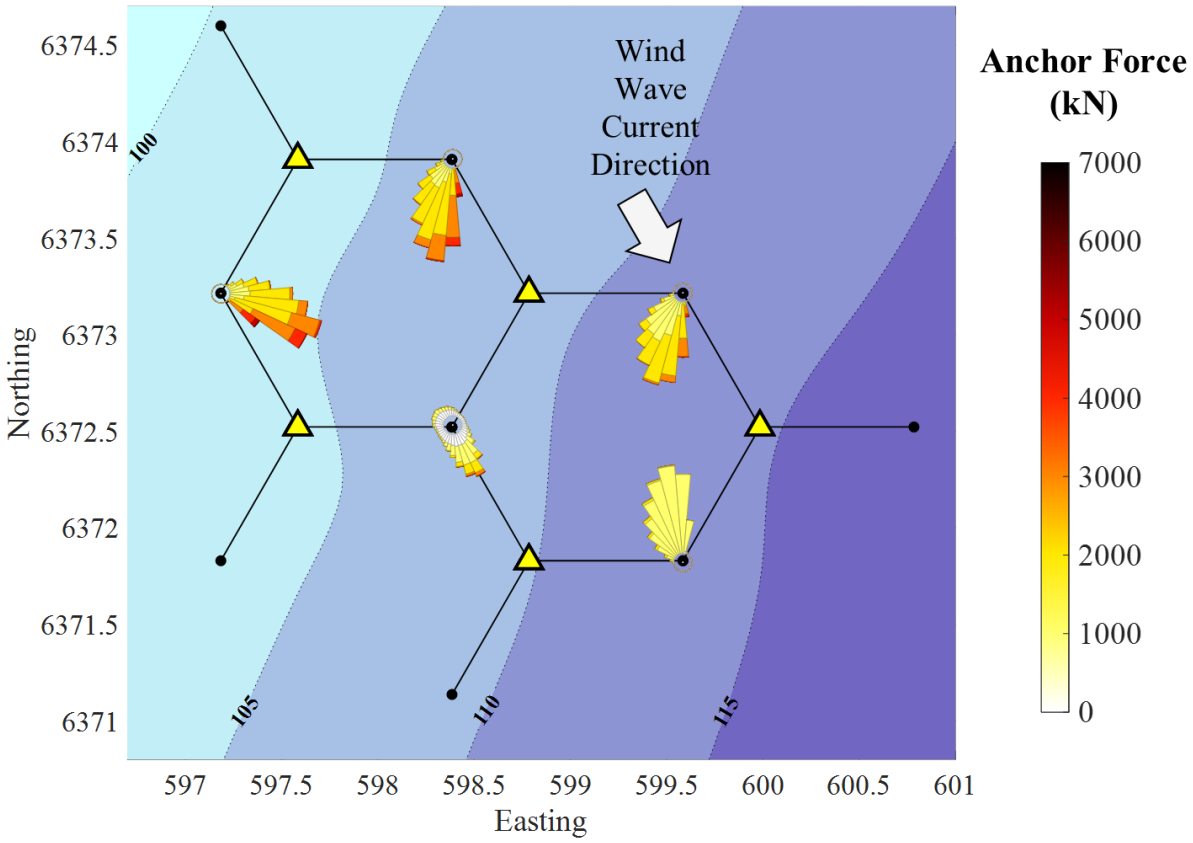

Figure 48: Directionality of multiline anchor forces for SLC load case with 330° WWC direction. Note that the length of each direction bin indicates the frequency of occurrence for the bin.

Since the 3-line anchor is the only anchor that can experience force in any direction, it is the best anchor to observe the alignment of the force direction relative to the WWC direction. Table 20 reveals that average direction of the 3-line anchor force exhibits significant alignment with the WWC direction, which is consistent with the results of Fontana et al. (2018). The average force direction is always within 35° of the WWC direction, and on average is 19° different than the WWC direction. The general alignment of the 3-line anchor force direction with the WWC direction can be understood by considering the flow of forces. All connected FOWTs have a force applied to them in the direction of the WWC, and the fixed-point anchors are the nodes resisting this force.

Therefore, the collective force applied to all connected FOWTs is applied to the multiline anchor in the same direction.

Table 20: Mean 3-line anchor force direction and difference from WWC direction across all load cases

		WWC Direction (°)					
		30	**90**	**150**	**210**	**270**	**330**
DLC 1.6	Mean Anchor Force Direction (°)	157	108	67	19	305	213
	Difference (°)	23	12	7	19	5	27
DLC 6.1	Mean Anchor Force Direction (°)	159	110	72	33	315	213
	Difference (°)	21	10	12	33	15	27
SLC	Mean Anchor Force Direction (°)	156	105	69	35	321	213
	Difference (°)	24	15	9	35	21	27

Even though the directional range of a 2-line anchor force is limited to 120°, the mean direction is still biased towards alignment with the WWC direction. This is because the line most directly upwind of the turbine typically experiences higher forces than the downwind line, and this higher force in the vector summation of the net multiline anchor force results in a directional bias towards that force contribution. This can be seen in Figure 48 and Figure 49.

The directional bias due to a higher contributing line tension is also exhibited in the context of water depth difference between the connected turbines. Since turbines in shallower water depths experience higher line and anchor tensions, there is also a slight bias of the multiline anchor force direction toward these shallower water turbines. This is most evident when the WWC direction is parallel to the water depth contours, as shown in Figure 49.

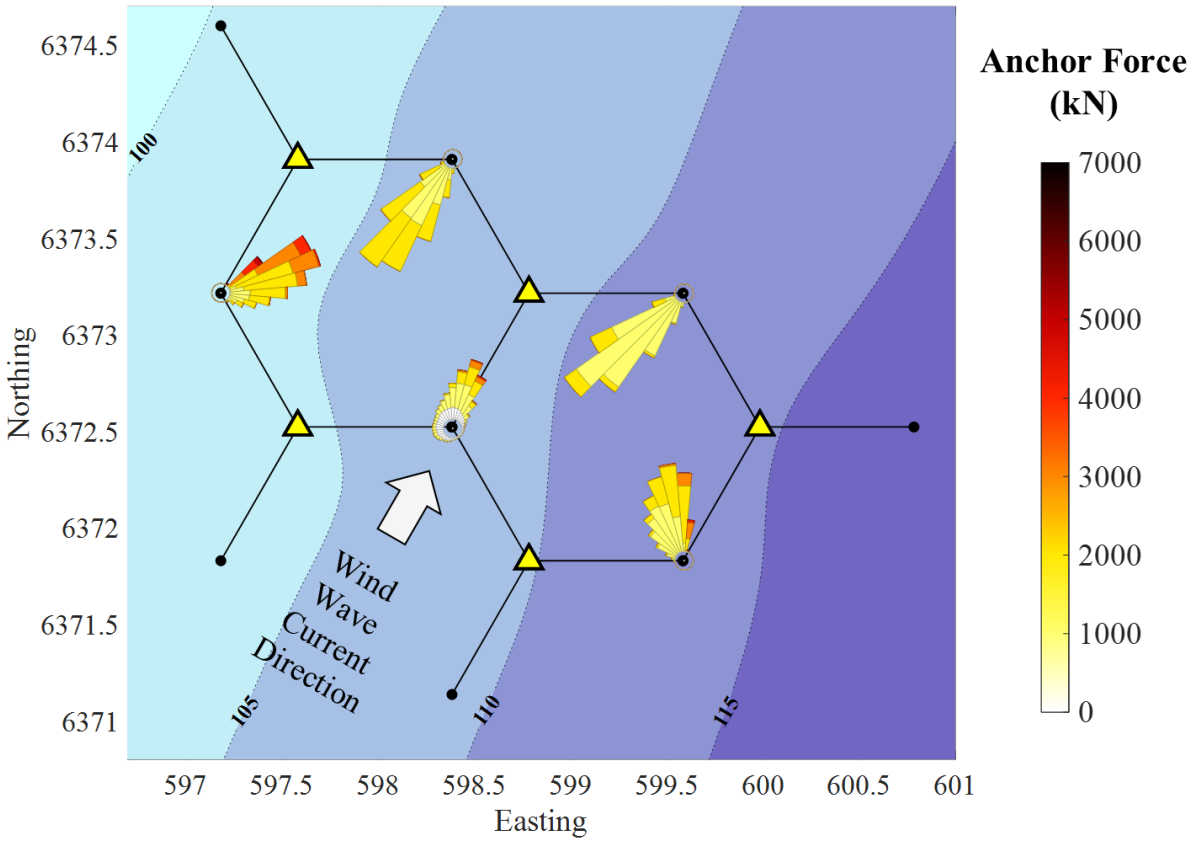

Figure 49: Directionality of multiline anchor forces for SLC load case with 210° WWC direction. Note that the length of each direction bin indicates the frequency of occurrence for the bin.

The range and standard deviation of the multiline anchor force direction increase as the environmental load case transitions from wind-dominated (DLC 1.6) to wave-dominated (SLC), consistent with the results found in Fontana et al. (2018). The standard deviation of the direction of the multiline anchor force is shown across all load cases in Table 21.

Table 21: Average standard deviation and range of direction of multiline anchor force across all WWC directions

	Standard Deviation (°)			Range (°)		
Multiline Anchor	**DLC 1.6**	**DLC 6.1**	**SLC**	**DLC 1.6**	**DLC 6.1**	**SLC**
111_123	10	14	17	71	90	100
112_143	11	14	18	74	90	101
121_133	11	14	17	74	93	101
122_141_153	36	52	53	360	360	360
132_151	11	15	18	76	93	101

This can also be seen by comparing the smaller ranges and larger frequency-of-occurrence maxima of DLC 1.6 in Figure 50, versus the larger ranges and smaller frequency-of-occurrence maxima of the SLC in Figure 49.

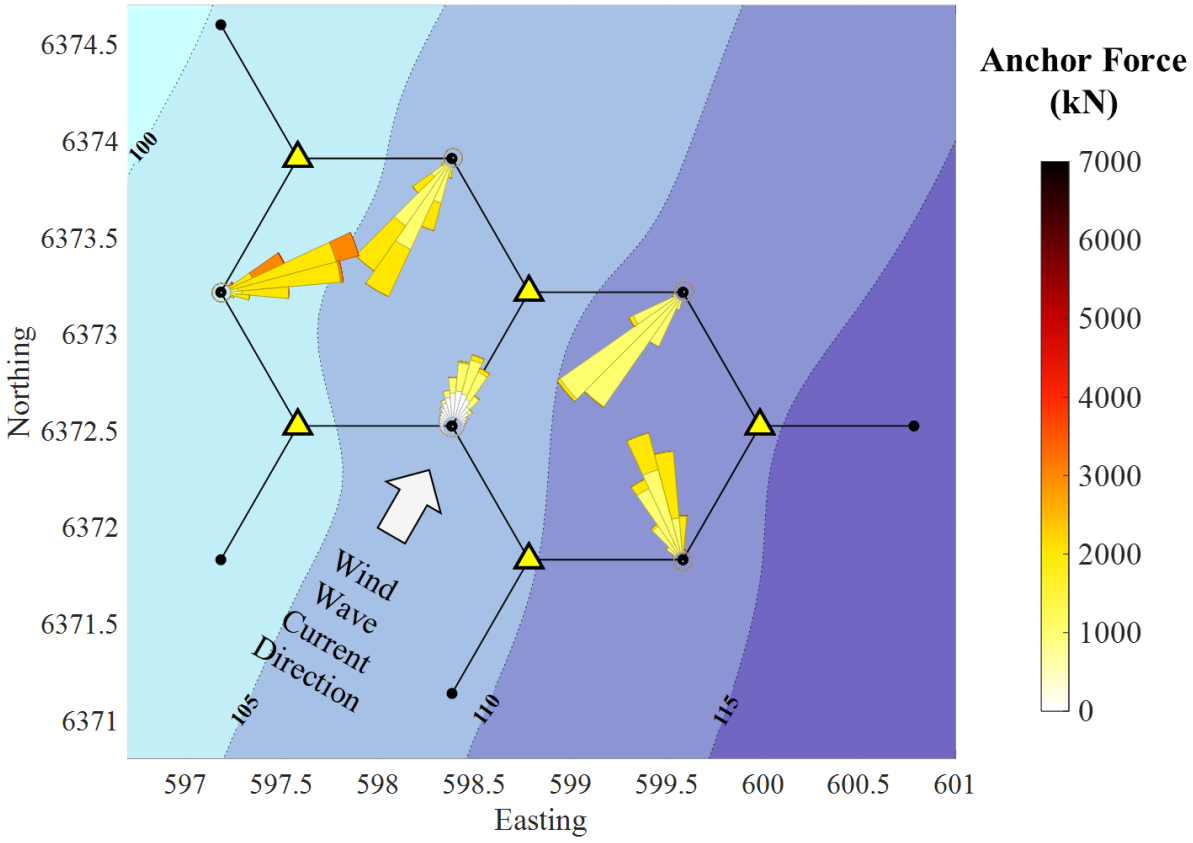

Figure 50: Directionality of multiline anchor forces for DLC 1.6 load case with 210° WWC direction. Note that the length of each direction bin indicates the frequency of occurrence for the bin.

This behavior can be understood by thinking about the loading of the FOWT platforms. Wind loading acts on the rotor and contributes primarily to mean platform position and anchor force. Wave loading acts on the platform and contributes primarily to the force cycles and maximum force. In other words, the turbulence of the wind is insignificant compared with the fluctuation of wave elevation, relative to anchor forces. Due to this

characteristic of the wave loading, the contributing line tensions have much larger fluctuations in cases that are wave dominated, and this larger variation in contributing line tensions results in the wider range in multiline anchor net force and direction.

4.5 Conclusions

In this study, a multiline anchor system is implemented in the context of an existing single-line floating offshore wind farm to examine the behavior and potential cost-saving benefits of the novel anchoring concept.

The modification of the mooring and anchor layout to create a multiline system was minimal, therefore the mooring system designs between the single-line system and multiline system were very similar – there was less than a 2% difference in mooring steel weight. However, this implementation of a multiline anchor mooring system reduced the number of anchors by 40% and the amount of anchor steel required by 41%, compared to the installed conventional single-line system. This reduction is the result of fewer anchors in multiline system (9) relative to the single-line system (15), while the slight decrease in average anchor size due to force cancellation in the multiline system has negligible effects in comparison. Even further cost savings may be realized in the installations and site investigations associated with the anchors. This could result in a proportional cost reduction approaching 40%, given that the number of anchor installations is equal to the number of anchors, and the that a detailed geotechnical site investigation is required at each anchor site [79]. Anchor installation and site investigation costs are not explored explicitly here, given that these costs fluctuate significantly as a product of vessel day rates, fuel costs, labor costs, and other factors. However, it can still be asserted that the combined reduction in steel, installations, and

site investigations required will result in significant cost savings in a floating offshore wind farm. This is an important conclusion to make, given that high cost of the floating wind development is a primary barrier in the industry [14].

Due to the multiple line attachments, the direction of the multiline anchor force has a range of 120° in the 2-line anchors and 360° in the 3-line anchor. In comparison, the forces on a single-line anchor come from one direction that has a range of less than 3° in this FOWT system. The mean direction of the multiline anchor force exhibits significant alignment with the WWC direction due to the flow of environmental forces down to the fixed anchor point. This characteristic most clearly displayed in the 3-line anchor, where the mean direction of the force is on average within 19° of the WWC direction. Furthermore, wave-dominated load cases (SLC) result in larger directional standard deviation and range of force on a multiline anchor than wind-dominated load cases (DLC 1.6), due to the differences in the governing environmental forces in these cases.

While the effect of decreased anchor size due to force cancellation was insignificant for the semisubmersible system used in this study, a spar platform may lead to a different, and better, conclusion in this context. This is due to the difference in platform and mooring dynamics between these two systems. Motion of semisubmersible platforms is dominated by offset (surge & heave), and large platform offset is tightly correlated with high anchor tension. In contrast, spar platform motion is dominated by rotation (pitch & roll), so anchor tensions are lower and upwind and downwind values are closer in magnitude [80]. For a multiline anchor in a spar-platform wind farm, this will also mean that the difference between contributing line tensions on a multiline anchor

will be smaller, leading to larger force cancellation and effectively smaller anchors that require less steel. Therefore, if a spar platform were to be used instead of a semisubmersible platform, the reduction in anchor steel due to smaller anchors may be quite significant, in addition to the reduction resulting from fewer number of anchors.

CHAPTER 5

CAPITAL COST ANALYSIS OF MULTILINE ANCHOR CONCEPT FOR FLOATING OFFSHORE WIND FARMS

5.1 Introduction

The exploration into the multiline anchor concept is driven by the goal of cost reduction in floating offshore wind farms. This chapter seeks to examine the benefit of implementing the multiline anchor concept in the context of capital expenditure (CAPEX) of the mooring and anchoring system, installation, and geotechnical site investigation. Given that the mooring and anchor dynamics and the associated system designs are highly sensitive to mooring geometry, the cost must be analyzed over a range of water depths and turbine spacings. The primary goals of this chapter are to analyze the cost reduction benefit of the multiline system relative to the single-line system for different spatial parameters and farm sizes, and to determine if any trends in the cost comparison exist over these parameters.

Catenary chain mooring systems are designed over a range of water depths and turbine spacings using the OC4-DeepCwind semisubmersible platform and Gulf of Maine metocean conditions. Cost models are presented, then applied to the different system designs to obtain anchor, mooring line, installation, and geotechnical site investigation costs. The difference between the cost of the single-line system and the multiline system is analyzed over a range of water depths, spacings, and farm sizes. Relationships between these parameters are then presented.

5.2 Mooring & Anchoring System Design

This section details the system models and design methods used to obtain mooring line lengths and weights over a range of spatial parameters.

5.2.1 Turbine & Platform Models and Simulation Software

The dynamics of the FOWT system are modeled with the National Renewable Energy Laboratory's FAST Code. FAST v8 is a comprehensive, fully-coupled aero-hydro-servo-elastic simulator capable of predicting motions and loads in the time domain [37], [38]. The NREL OC4-DeepCwind semisubmersible system used is appropriate for this study due to its suitability in any water depth. Furthermore, the OC4-DeepCwind platform employs the most commonly studied platform type (semisubmersible) in current FOWT technology/concepts [32], therefore it is a realistic choice for investigating the multiline concept in the context of a real project. Details on the OC4-DeepCwind system can be found in Robertson et al. (2014). The turbine chosen for this analysis is the National Renewable Energy Laboratory's (NREL) 5-MW reference turbine, which was developed to be representative of a typical utility-scale turbine and is widely used in the offshore wind energy research community [29].

5.2.2 Mooring Design Criteria

Mooring design for each combination of water depth and turbine spacing was carried out in general accordance with the American Bureau of Shipping standards [41]. The chain size and mooring line lengths were developed from a simplified mooring design regime, to prevent time-domain design in FAST from becoming prohibitive in computational expense. The mooring systems were designed for only the Ultimate Limit State, and were not evaluated for the Fatigue and Accidental Limit States. The three

critical design load cases selected to analyze the Ultimate Limit State are explained in the following section. Performance criteria to be met by the catenary mooring designs are governed by American Bureau of Shipping (2014) and are as follows:

1.) Average maximum line tension does not exceed the factored minimum breaking strength of the line (FS = 2.0 for DLC 1.6 and DLC 6.1, FS = 1.05 for SLC)
2.) Maximum platform offset does not exceed 10% of the turbine's water depth
3.) No vertical uplift force at the anchor

In 2.), the 10% water depth limit is chosen based the platform offset limits discussed in Campanile, Piscopo, & Scamardella (2018).

5.2.3 Environmental Conditions

Candidate mooring systems must be subjected to a range of environmental loading conditions to verify the adequacy of the designs. The Gulf of Maine conditions were used for this study, as this site possesses thorough environmental data. The wind, wave and current (WWC) parameters at this site for the three selected critical environmental conditions are taken from the full scale VolturnUS project [44], harvested from over ten years of buoy data at a site off Monhegan Island, Maine [45], [46]. Details of these load cases are provided in Table 22 [43]**.**

Table 22: Environmental conditions used for mooring design (*50-yr significant wave height conditioned upon rated wind speed)

Load Case	**DLC 1.6**	**DLC 6.1**	**SLC**
Conditions	Extreme Operating	Extreme Non-Operating	Survival Non-Operating
Wind Speed at Hub Height	11.4 m/s (rated)	40 (50-yr)	45 m/s (500-yr)
Turbulence Intensity	10%	10%	10%
Significant Wave Height	8.0 m (50-yr*)	10.2 (50-yr)	12 m (500-yr)
Peak Spectral Wave Period	12.7 sec	14.1 sec	15.3 sec
JONSWAP Gamma Factor	2	2.5	2.5

Current Speed	0.30 m/s	0.45 m/s	0.55 m/s

The wind speed in DLC 1.6 of 11.4 m/s is the rated wind speed of the NREL 5-MW reference turbine that produces peak thrust [35], as designated in American Bureau of Shipping [41]. The turbulent wind field is generated with a Kaimal spectrum and 10% turbulence intensity via Turbsim [47]. Waves are generated with a JONSWAP spectrum, and wave heights are Rayleigh distributed [48]. Current is steady and equal at each FOWT. Six 1-hour simulations using different random seeds were completed for each combination of load case and WWC direction, as designated in the IEC design standards [60].

For each turbine, two co-directional WWC directions were analyzed during the design process, aligned either directly with a mooring line or halfway between two mooring lines. Applying a WWC direction in which a mooring line is directly upwind is likely to produce peak tensions and minimum lay lengths for that line (see 1. and 3. of Section 5.2.2), and applying a WWC direction directly in between two mooring lines is likely to produce maximum platform offset (see 2. of Section 5.2.2). A range of WWC directions from 0-60° is adequate due to the three-fold symmetry of the support structure.

Wind and waves were modeled as independent at each turbine, and wind wake effects were not considered. The choice of independent wave fields at the turbines is justified by previous studies as detailed in Chapter 3, which reveal that spatial coherence of wave fields is insignificant for typical offshore wind turbine spacings. The effect of wind wakes relative to multiline anchor system forces is likely to affect the results, and is still an ongoing topic of investigation by the authors. Additional discussion of wind wake effects on the multiline anchor system can be found in Chapter 5.

5.2.4 Spatial and Design Parameters

Mooring and anchoring systems were designed for all combinations of water depth and turbine spacing listed in Table 23. The minimum water depth of 100 m is based on a report published by the European Wind Energy Association, which estimated that for a commercial scale wind farm equipped with 5 MW turbines and installed in water depths of 100m, the CAPEX and cost of energy for floating designs is similar to the CAPEX and cost of energy of farms using jackets or tripod foundations at 50m water depths [81]. The maximum water depth is based on the 2016 Offshore Wind Energy Resource Assessment report, which states that global floating offshore wind technology developers deemed 1,000 m depth was a reasonable cutoff for resource assessment using current technology and industry experience [82]. Turbine spacing ranges from 6 to 12 rotor diameters for the NREL 5 MW reference turbine. A minimum spacing of 500 m (4 rotor diameters) was attempted, which was the minimum spacing discovered in the review of installed offshore wind turbine spacings of Chapter 3. However, adequate mooring designs for this turbine spacing with the simplified design regime for could not be obtained without implementing more complex mooring solutions, such as clump weights. Therefore, the minimum spacing was increased to 750 m (6 rotor diameters). The maximum spacing of 1500 m was based on the patterning the default NREL OC4-DeepCwind semisubmersible system into a 3-line anchor geometry, which results in a turbine spacing of 1451 m. To restrict the mooring design process from becoming prohibitive in computational expense, a limited number of chain sizes were analyzed. The chain sizes studied still reflect the full range of realistic mooring chains [REF], but increments between mooring chain sizes are increased. Similarly, the mooring line

lengths were increased by increments of 10 m in each iterative step of the mooring design.

Table 23: Spatial input parameters and mooring line design parameters

Spatial Parameters	
Water Depths (m)	100, 250, 500, 750, 1000
Turbine Spacing (m)	750, 1000, 1250, 1500
Mooring Design Parameters	
Nominal Chain Diameters (mm)	40, 60, 81, 100, 120, 142, 162
Mooring Line Length Increments (m)	10

5.2.5 Mooring Design Results

The results of the mooring design are shown in Table 24.

Table 24. Mooring design results across all water depths and turbine spacings. Red shading indicates larger values, and green shading indicates smaller values. * Indicated cases where platform offset limit was increased to 15% instead of 10%

MOORING LINE LENGTH						
		Depth				
		100	250	500	750	1,000
Spacing	750	420*	500*	700	930	1,170
	1,000	560*	620	800	1,020	1,250
	1,250	700*	750	920	1,120	1,330
	1,500	840	890	1,030	1,220	1,430
CHAIN NOMINAL DIAMETER						
		Depth				
		100	250	500	750	1,000
Spacing	750	162*	162*	142	100	81
	1,000	162*	142	120	100	60
	1,250	162*	120	100	81	60
	1,500	142	100	100	81	40
WEIGHT PER MOORING LINE						
		Depth				
		100	250	500	750	1,000
Spacing	750	221*	263*	282	186	153
	1,000	294*	250	230	204	90
	1,250	368*	216	184	147	96
	1,500	339	178	206	160	46

It can be seen that for larger water depths and turbine spacings, longer line lengths with smaller chain sizes are suitable. This is due to the magnitude of the suspended line – as water depth and turbine spacing increases, the length of line suspended also increases, therefore smaller chain sizes are sufficient for developing the restoring force that provides stationkeeping of the mooring system. In contrast, in shallower water depths with smaller turbine spacings, the length of the suspended line decreases, therefore heavier chain is required to develop the necessary restoring force. Given that chain size is more influential over total line weight than chain length, it can been seen that there is a trend of larger weights per mooring line for the shallower water depths and closer turbine spacings. The deviation from this trend in the smallest water depths and turbine spacings is due to the deviation from consistent mooring criteria – in these cases, platform offset limits had to be increased slightly to 15% of water depth to obtain a satisfactory mooring design.

5.3 Cost Analysis

The following section details the cost models utilized for the anchors, moorings lines, installation, and geotechnical site investigation, and compares the costs between the single-line and multiline anchor systems. Given that the goal of this cost analysis is the comparison of the multiline system to the single line system for a range of the mooring geometries and farm sizes, the flexibility/breadth of the model is most important. The costs of steel, manufacturing, vessel day rates, vessel fuel, labor, and other components can fluctuate significantly across suppliers, companies, and over time. When interpreting the results of this section, more focus should be placed on the comparison between the costs, and less focus on the exact values themselves.

5.3.1 Cost Models

The cost analysis of the system carried out in accordance with Hall [83], which provides metrics for calculating the cost per anchor and mooring line based on the maximum steady state forces and tensions and the cost of anchor installation per anchor type [83]. A literature review was conducted to gather information about mooring costs across other research efforts, but the cost metrics provided in [83] are chosen for the majority of the cost analysis due to their flexibility across multiple mooring systems and anchor forces. It should be noted that the cost per geotechnical site investigation is taken separately from Bjerkseter et al. [84], as discussed later in this section.

Table 25. Cost models for FOWT stationkeeping system. Models for anchor and mooring line material are based on the maximum steady state anchor forces and line tensions. [83], [84]

		Material	Installation	Geotechnical Site Investigation
Anchors	Drag Embedment Anchor (DEA)	$100/kN/anchor	$5000/anchor	$83,000/anch site
	Suction Pile Anchor (SPA)	$150/kN/anchor	$11,000/anchor	
Mooring Lines	Chain	$0.42/kN/m	-	-

The metric of a geotechnical site investigation cost per each anchor site rather than a cost per farm size or area is supported by the standard for Support Structures of Offshore Wind Turbines, which states that for multiple foundations such as in a wind farm, the soil stratigraphy and range of soil strength properties shall be assessed per foundation location [78]. Furthermore, the recommended practice for Offshore Soil Mechanics and Geotechnical Engineering requires a minimum of one detailed geotechnical investigation at each anchor site, stating that at a final stage, the soil

investigation should provide all necessary data for a detailed foundation design of a specific structure at the specific location [79].

In real wind farm development, the cost of the geotechnical site investigation would not be a simple independent value as shown in Table 25, but rather a function of water depth, site conditions, pre-existing surveying data, and method of investigation. Deepwater geotechnical site investigation is a cost intensive activity that typically causes operators to evaluate trade-offs between project economics and the relative value of the information being gathered. Methods of geotechnical site investigation include box cores, piston cores, Jumbo Piston Cores (JPT), and Cone Penetration Tests (CPT) [85]. Increased water depth at a site will likely increase the cost per investigation, dependent upon winching speeds [85]. Investigation vessel and platform type will also influence cost - cost savings achieved through use of smaller, less well-equipped vessels may sometimes be more economical, but their cost savings can be outweighed by the additional expense of having to remobilize a specialized geophysical survey vessels [85].

5.3.2 Cost Analysis Results per Line and per Anchor

Costs per mooring line and per anchor are shown in Table 26. In a single-line configuration, it assumed that all turbines will utilize drag embedment anchors (DEAs), as they are typically the most cost-efficient anchor type, and are suitable in most soil types. In the multiline configuration, it is assumed that all turbines will utilize suction pile anchors (SPAs), as their axisymmetric strength makes them suitable for the multidirectional loading produced in the multiline configuration. Even though some of the perimeter anchors points in the multiline configuration experience only unidirectional loading, and therefore could be satisfied with a DEA, it is unlikely that multiple anchor

types would be used within the same floating wind farm. In the single-line configuration, all DEAs are designed for the maximum steady state anchor force, as detailed in [83]. In the multiline configuration, the perimeter anchors are designed for the maximum steady-state single-line force, and the interior anchors are designed for the maximum steady-state multiline force. Multiline anchor force is calculated as the vector sum of the contributing line tensions, as detailed in Chapter 2. In an effort to be conservative, the maximum steady state multiline anchor force is taken as the vector sum combination of the maximum of the highest contributing single-line force(s) and the minimum of the lowest contributing single-line force(s), as show in Figure 26a.

Table 26. Cost per mooring line and per anchor for single-line and multiline systems

		Mooring Lines			Anchors				
		Maximum Steady State Line Tension (kN)	Cost per meter line length ($k)	Cost per line ($k)	Maximum Steady State Anchor Force (kN)		Cost per Anchor ($k)		
					Single-line	Multi-line	Single-line (DEA)	Multi-line (SPA)	
Depth (m)	Spacing (m)							Perimeter	Interior
100	750	2,109	0.89	1,116	1,063	1,063	106	159	159
250		2,331	0.98	1,469	988	930	99	148	139
500		2,400	1.01	2,117	612	604	61	92	91
750		1,561	0.66	1,830	249	249	25	37	37
1,000		1,277	0.54	1,882	131	131	13	20	20
100	1,000	2,742	1.15	1,935	1,258	1,258	126	189	189
250		2,552	1.07	1,994	1,476	943	148	221	141
500		2,055	0.86	2,071	763	669	76	114	100
750		1,704	0.72	2,190	353	345	35	53	52
1,000		753	0.32	1,186	118	117	12	18	17
100	1,250	3,886	1.63	3,428	2,064	2,064	206	310	310
250		2,508	1.05	2,370	1,691	976	169	254	146
500		1,649	0.69	1,912	682	640	68	102	96
750		1,242	0.52	1,753	338	320	34	51	48
1,000		820	0.34	1,373	188	164	19	28	25
100	1,500	4,895	2.06	5,180	3,400	2,573	340	510	386

250		2,028	0.85	2,274	1,322	912	132	198	137
500		1,984	0.83	2,575	1,012	753	101	152	113
750		1,400	0.59	2,153	491	405	49	74	61
1,000		394	0.17	710	108	94	11	16	14

The cost per meter line length in Table 26 correlate very tightly with the steel weight per line in Table 24, which serves as a good check for the cost model.

5.3.3 Cost Analysis Results for a 100-turbine Commercial Scale Farm

To evaluate how costs change between the single-line and multiline system over a range of water depths and spacings, the farm size variable is held constant 100 turbines, and the results are presented in Table 27.

Table 27: Cost analysis of a 100-turbine commercial scale floating offshore wind farm. Red shading indicates larger values, and green shading indicates smaller values.

		Mooring Lines and Anchors		**Anchor Installation**		**Geotechnical Site Investigation**		**Total**		
Depth (m)	**Spacing (m)**	Single ($m)	Multi ($m)	Single ($m)	Multi ($m)	Single ($m)	Multi ($m)	Single ($m)	Multi ($m)	Reduction (%)
100	750	144	131	1.5	1.3	24.8	9.9	170	142	16
250		176	164	1.5	1.3	24.8	9.9	203	175	14
500		230	223	1.5	1.3	24.8	9.9	256	234	9
750		190	187	1.5	1.3	24.8	9.9	217	199	8
1,000		192	191	1.5	1.3	24.8	9.9	218	202	8
100	1,000	231	216	1.5	1.3	24.8	9.9	258	227	12
250		244	219	1.5	1.3	24.8	9.9	270	231	15
500		230	220	1.5	1.3	24.8	9.9	256	231	10
750		230	225	1.5	1.3	24.8	9.9	256	236	8
1,000		122	121	1.5	1.3	24.8	9.9	148	132	11
100	1,250	405	380	1.5	1.3	24.8	9.9	431	391	9
250		288	259	1.5	1.3	24.8	9.9	314	270	14
500		212	203	1.5	1.3	24.8	9.9	238	214	10
750		185	181	1.5	1.3	24.8	9.9	212	192	9
1,000		143	140	1.5	1.3	24.8	9.9	169	152	10

100	1,500	620	569	1.5	1.3	24.8	9.9	646	580	10
250		267	246	1.5	1.3	24.8	9.9	293	257	12
500		288	273	1.5	1.3	24.8	9.9	314	284	10
750		230	223	1.5	1.3	24.8	9.9	256	234	9
1,000		74	73	1.5	1.3	24.8	9.9	101	84	16

It can be observed that the steel costs of the mooring lines and anchors account for the largest portion of the mooring system capital cost, geotechnical site investigation for the second largest, and anchor installation the least. More details on the particular contribution of each cost component are shown in Table 28. The multiline concept decrease the percent contribution of the anchors and geotechnical site investigation.

Table 28: Average percentages of each cost component relative to total cost

	Single-line	**Multiline**
Anchors	9	6
Mooring Lines	79	89
Total Steel (Anchors + Mooring Lines)	88	94
Installation	1	1
Geotechnical Site Investigation	11	5

The strongest relationship found between the spatial parameters and the cost reduction is shown in Figure 51, which show that larger reductions in line and anchor cost are result from mooring system configuration with smaller ratios of water depth to spacing.

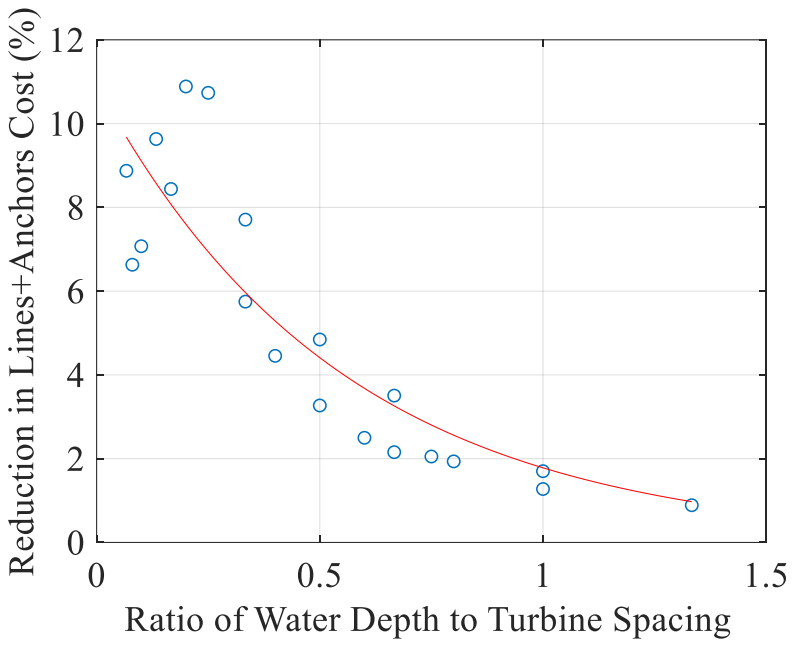

Figure 51: Relationship between depth:spacing ratio and cost reduction for lines+anchors

5.3.4 Cost Analysis Relative to Farm Size

Due the perimeter effects, or the ratio of edge anchors to interior anchors in a multiline configuration, the multiline concept results in larger cost benefits for larger farm sizes. More specifically, the reduction in total mooring & anchoring system capital cost due to the multiline concept always increases with increasing farm size. This is due to the decrease in the aforementioned perimeter effects, as shown in Figure 52. Perimeter anchors are defined as anchors at the edge of the farm that have less than 3 lines attached, while interior anchors are defined as multiline anchors within the farm that have 3-lines attached concentrically.

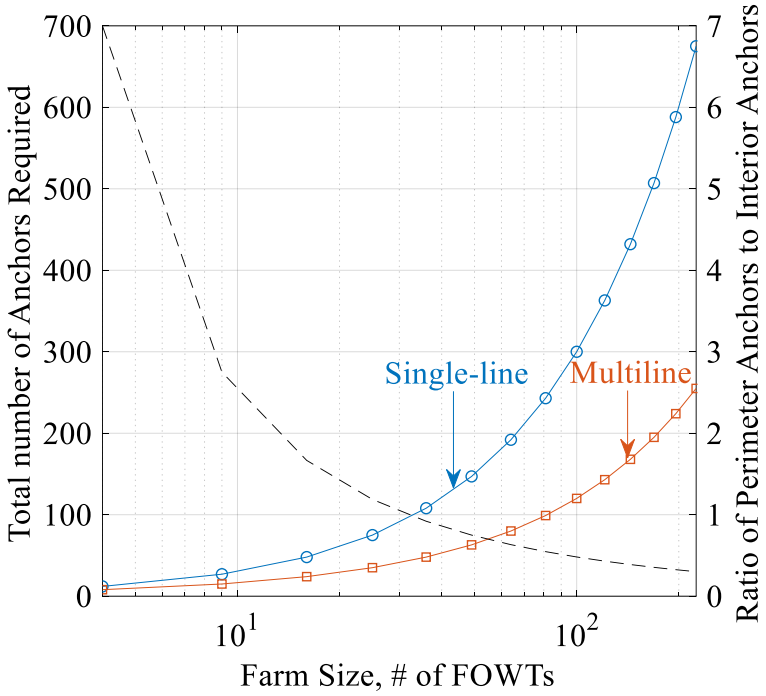

Figure 52: Number of single-line and multiline anchors relative to farm size

Cost models for anchor installation only account for the number and type of anchor, and the cost model for geotechnical site investigation only accounts for number of anchors. Therefore the single-line and multiline anchor installation and geotechnical site investigation costs calculated in this study are independent of the spatial parameters, allowing for the comparison of these costs between the single-line and multiline system relative to only farm size, as shown in Table 29.

Table 29: Cost of anchor installation and geotechnical site investigation for single-line and multiline systems relative to farm size

	Installation			Geotechnical Site Investigation		
Number of Turbines	**Single-line ($m)**	**Multiline ($m)**	**Reduction ($m)**	**Single-line ($m)**	**Multiline ($m)**	**Reduction (%)**
4	0.06	0.09	-47	0.99	0.66	33
9	0.14	0.17	-22	2.23	1.24	44
16	0.24	0.26	-10	3.97	1.99	50
25	0.38	0.39	-3	6.20	2.90	53
36	0.54	0.53	2	8.93	3.97	56
49	0.74	0.69	6	12.2	5.21	57

64	0.96	0.88	8	15.9	6.62	58
81	1.22	1.09	10	20.1	8.19	59
100	1.50	1.32	12	24.8	9.93	60
121	1.82	1.57	13	30.0	11.8	61
144	2.16	1.85	14	35.7	13.9	61
169	2.54	2.15	15	41.9	16.1	62
196	2.94	2.46	16	48.6	18.5	62
225	3.38	2.81	17	55.8	21.1	62

It can be seen that the multiline configuration results in higher installation costs than those of the single-line configuration for farm sizes smaller than 36 turbines. In these smaller farm sizes, the higher installation cost of the SPA in the multiline configuration versus the DEA in the single-line configuration outweighs the cost reduction due to fewer anchor sites. However, the multiline configuration always results in lower geotechnical site investigation costs than the single-line configuration. In both the installation and geotechnical site investigation costs, the cost reduction due to the multiline anchor concept increases rapidly at first with farm size, then tapers off as the perimeter effects diminish (see Ratio of Perimeter Anchors to Interior Anchors in Figure 52). It should be noted that in a real project, installation and geotechnical site investigation costs per anchor would likely not be independent of spatial parameters, as previously explained in Section 5.3.1.

5.4 Conclusions

This chapter presents a capital cost analysis of the materials, installation, and geotechnical site investigation for floating offshore wind farms utilizing conventional single-line and novel multiline anchor systems. Mooring systems are designed for FOWTs over a range of water depths ranging from 100 to 1000 m, and turbine spacings ranging from 750 to 1500 m, using the NREL 5 MW reference turbine and the OC4-

DeepCwind semisubmersible system. Results of the mooring design reveal that for larger water depths and turbine spacings, longer line lengths with smaller chain sizes are suitable, resulting in lighter line weights. Cost models for less expensive DEAs used in the single-line system and more expensive SPAs used in the multiline are presented, along with simple cost models for geotechnical site investigation.

Results of the cost analysis are first presented per line and per anchor for each combination of water and depth and spacing, revealing that the cost per mooring line is significantly more expensive than the cost per anchor. A cost analysis of a hypothetical 100-turbine commercial scale farm is then presented for the cost of the mooring lines, anchors, anchor installation, and geotechnical site investigation. This analysis shows that implementation of the multiline concept could result in a cost reduction of 8 - 16% relative to the single-line system. An exponential decay relationship exists between the ratio of water depth to turbine spacing and the cost reduction in the lines & anchors – as the depth:spacing ratio decreases, the cost reduction is maximized. Lastly, a cost analysis of anchor installation and geotechnical site investigation relative to farm size is presented, which shows that the multiline anchor concept typically reduces the cost of anchor installation and geotechnical site investigation relative to the single-line concept. The exception to this result is in installation costs in farm sizes smaller than 36 turbines, where the higher installation cost of the SPA in the multiline configuration versus the DEA in the single-line configuration outweighs the cost reduction due to fewer anchor sites.

CHAPTER 6

CONCLUSIONS AND FUTURE WORK

6.1 Conclusions

This thesis evaluates a novel multiline anchoring concept in which FOWTs share anchors, in an effort to lower FOWT support structure costs. The concept is investigated for potential implementation in a real floating offshore wind farm, and the research seeks to understand all behaviors and characteristics of such a system that may be relevant in a development context.

Chapter 2 models the OC4-semisubermsible system in a multiline configuration and compares the results of this analysis are compared to conventional single-line anchor system. It is shown that the implementation of the multiline anchor system would result in large reductions in the total number of anchors required—60% in the 3-line anchor system and 79% in the 6-line anchor system for a typical commercial scale 100-turbine floating offshore wind farm. The average maximum anchor force differs significantly for the multiline anchor compared with the single-line anchor, decreasing by 16% in the 3-line anchor and increasing by 20% in the 6-line anchor for DLC 1.6, and decreasing by 11% in the 3-line anchor and increasing by 10% in the 6-line anchor for the SLC. Therefore, the design strength of the multiline anchor would be different than its single-line counterpart.

It is also shown that a multiline anchor will be subjected to loading from any direction over the course of its design life, as the average direction of multiline anchor net force is aligned with the direction of the environmental load. Furthermore, force direction reversals within a single force cycle are present in extreme cases for the multiline anchor.

A variety of anchor types with axisymmetric strength exist that can perform appropriately under such multidirectional loading conditions and differ from drag anchors that are being considered for mooring of single-line FOWTs.

In Chapter 3, spatial characteristics of waves in the context of the multiline anchor are investigated. The goal was to determine if multiline anchor force dynamics are a function of spatial wave coherence, or if the treatment of wave fields as independent at each turbine provides adequate load characterizations. While regular waves fields in the multiline system showed the limits of what the difference in multiline anchor forces could be between these two models could be, the irregular wave fields applied to FOWTs in a multiline anchor system revealed no consistent trends that differentiated multiline anchor force dynamics generated by spatially independent versus coherent waves. Differences between the two wave loading models were insignificant – mean anchor force values differed by less than 1% and maximum anchor force values differed by less than 5% in the 3-line anchor system. A deeper investigation into spatial wave characteristics revealed that the correlation coefficient between wave elevation time histories at different points in space decays rapidly with distance between the points. Even for the maximum wave height studied (Hs = 12 m), the correlation length was less than 300 m.

The situation where wave coherence could potentially have an effect on multiline anchor force dynamics is one in which turbine spacing is less than or equal wave correlation length. It is almost certain that this situation is not feasible/possible for several reasons. First, in the context of turbine spacing, it is observed that spacing will likely not be less than 4 rotor diameters. This minimum spacing limit, coupled with the

limit of floating turbines not being less than 4 MW capacity and 120 m rotor diameter, means that the absolute minimum spacing of FOWTs is likely to be at about 500 m. In combination with the findings that significant wave heights must be unrealistically large (Hs > 25 m) to produce wave correlation lengths of this distance, it can be concluded that a situation will not exist in which waves will be significantly correlated at the connected platforms in multiline anchor systems for FOWTs.

In Chapter 4, a multiline anchor system is implemented in the context of an existing single-line floating offshore wind farm to examine the behavior and potential cost-saving benefits of the novel anchoring concept. The modification of the mooring and anchor layout to create a multiline system was minimal, therefore the mooring system designs between the single-line system and multiline system were very similar – there was less than a 2% difference in mooring steel weight. However, this implementation of a multiline anchor mooring system reduced the number of anchors by 40% and the amount of anchor steel required by 41%, compared to the installed conventional single-line system. This reduction is the result of fewer anchors in multiline system (9) relative to the single-line system (15), while the slight decrease in average anchor size due to force cancellation in the multiline system has negligible effects in comparison. Even further cost savings may be realized in the installations and site investigations associated with the anchors. This could result in a proportional cost reduction approaching 40%, given that the number of anchor installations is equal to the number of anchors, and the that a detailed geotechnical site investigation is required at each anchor site [78], [79].

Due to the multiple line attachments, the direction of the multiline anchor force has a range of 120° in the 2-line anchors and 360° in the 3-line anchor. In comparison, the forces on a single-line anchor come from one direction that has a range of less than 3° in this FOWT system. The mean direction of the multiline anchor force exhibits significant alignment with the WWC direction due to the flow of environmental forces down to the fixed anchor point. This characteristic most clearly displayed in the 3-line anchor, where the mean direction of the force is on average within 19° of the WWC direction. Furthermore, wave-dominated load cases (SLC) result in larger directional standard deviation and range of force on a multiline anchor than wind-dominated load cases (DLC 1.6), due to the differences in the governing environmental forces in these cases.

Chapter 5 presents a capital cost analysis of the materials, installation, and geotechnical site investigation for floating offshore wind farms utilizing conventional single-line and novel multiline anchor systems. Mooring systems are designed for FOWTs over a range of water depths ranging from 100 to 1000 m, and turbine spacings ranging from 750 to 1500 m, using the NREL 5 MW reference turbine and the OC4-DeepCwind semisubmersible system. Results of the mooring design reveal that for larger water depths and turbine spacings, longer line lengths with smaller chain sizes are suitable, resulting in lighter line weights. Cost models for less expensive DEAs used in the single-line system and more expensive SPAs used in the multiline are presented, along with simple cost models for geotechnical site investigation.

Results of the cost analysis are first presented per line and per anchor for each combination of water and depth and spacing, revealing that the cost per mooring line is

significantly more expensive than the cost per anchor. A cost analysis of a hypothetical 100-turbine commercial scale farm is then presented for the cost of the mooring lines, anchors, anchor installation, and geotechnical site investigation. This analysis shows that implementation of the multiline concept could result in a cost reduction of 8 - 16% relative to the single-line system. An exponential decay relationship exists between the ratio of water depth to turbine spacing and the cost reduction in the lines & anchors – as the depth:spacing ratio decreases, the cost reduction is maximized. Lastly, a cost analysis of anchor installation and geotechnical site investigation relative to farm size is presented, which shows that the multiline anchor concept typically reduces the cost of anchor installation and geotechnical site investigation relative to the single-line concept. The exception to this result is in installation costs in farm sizes smaller than 36 turbines, where the higher installation cost of the SPA in the multiline configuration versus the DEA in the single-line configuration outweighs the cost reduction due to fewer anchor sites.

6.2 Future Work

The primary goal of the future work is to expand the investigation of the multiline anchor system across different mooring systems, platform types, anchor types, and spatial parameters. Furthermore, the effect of the wind wakes relative to the multiline concept must be investigated, over a range of turbines spacings and farm size.

6.2.1 Wind Wake Effects and Wind Spatial Coherence

Wind wakes result in lower speeds and higher turbulence in the wind fields downwind of the turbine, as shown in Figure 53 [49]. In a typical single-line floating offshore wind farm, turbine spacing is chosen to be large enough such that wind wake

effects on adjacent turbines are minimized and therefore power production maximized. In an interconnected multiline anchor system, additional consideration must be made regarding the effect of wind wakes on the multiline anchor force dynamics.

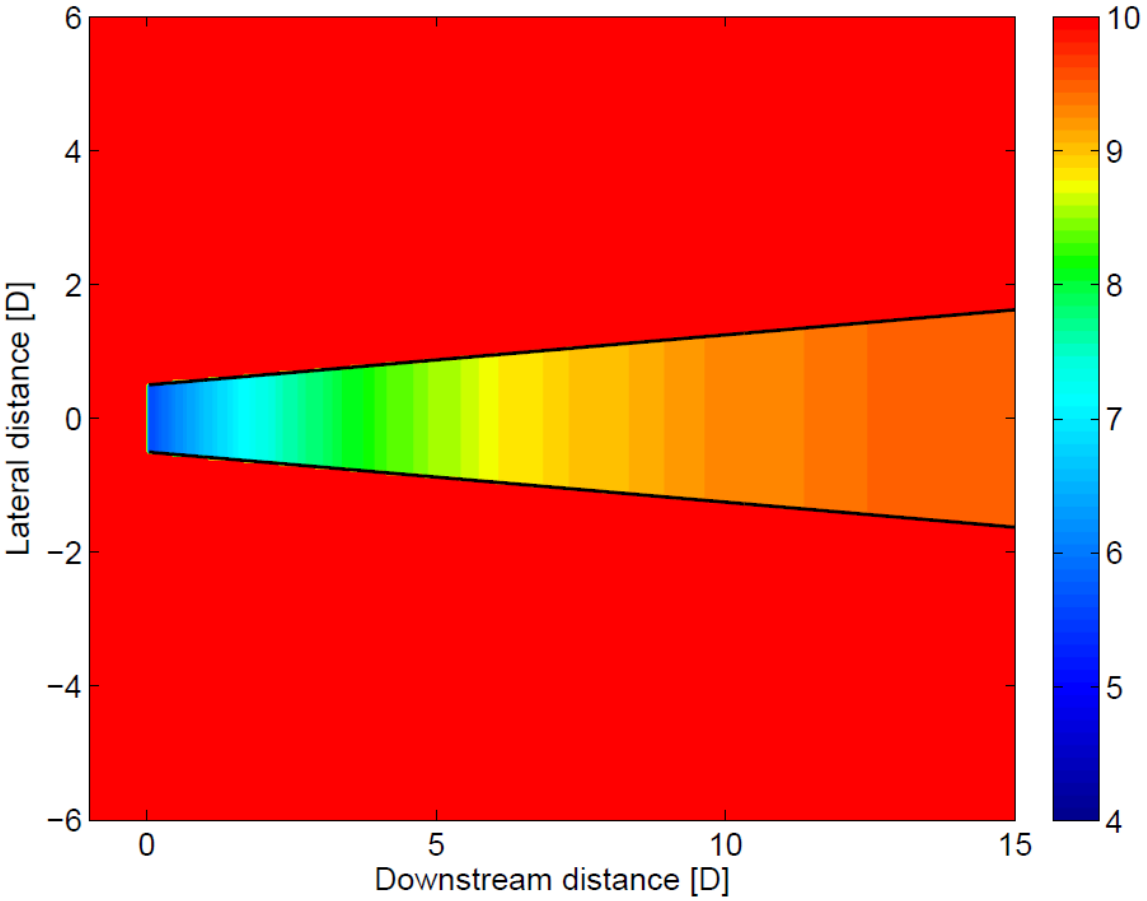

Figure 53: Wake behind a turbine (Jensen model). D = rotor diameter. [49]

In previous work on the multiline concept, wind wake effects were neglected, and wind was treated as independent at each turbine. This allowed the multiline system to be analyzed just based on the number of lines connected, and multiline anchor force dynamics were assumed to be the same regardless of where the multiline anchor was located within the farm. The incorporation of wind wake effects would decrease the wind speed experienced by the turbines downwind, which would decrease tension in the upwind lines, and increase tension in the downwind lines. Therefore each multiline

anchor would need to be analyzed for specific locations, as the wind characteristics of the connected turbines would be different depending on the multiline anchor's placement within the farm. Wake adding would need to be calculated due to overlapping wind wakes, as detailed in [49]. A range of kinematic wake models in varying precision and complexity are available, including the Jensen model, Larsen model, and the Frandsen analytical model. The Jensen model as shown in Figure 53 would be suitable for this study due to its combination of simplicity and accuracy. The Jensen model only computes the change in mean wind speed, however this is acceptable for multiline anchor force modeling given that anchor forces of FOWTs are insensitive to wind turbulence.

Wind wakes are expected to have the largest effect in conditions where the turbine is operational, as this produces the largest thrust on the rotor, and in effect largest mean platform offset and upwind line tension. The relationship between wind speed and rotor thrust for operational conditions can be seen in Figure 54. It is expected that net multiline anchor forces will decrease with the inclusion of wake effects. This is because decreased thrust on the turbines due to wind wake effects brings the turbines closer to their initial static positions, where all contributing tensions are equal and the net multiline anchor tension equals zero.

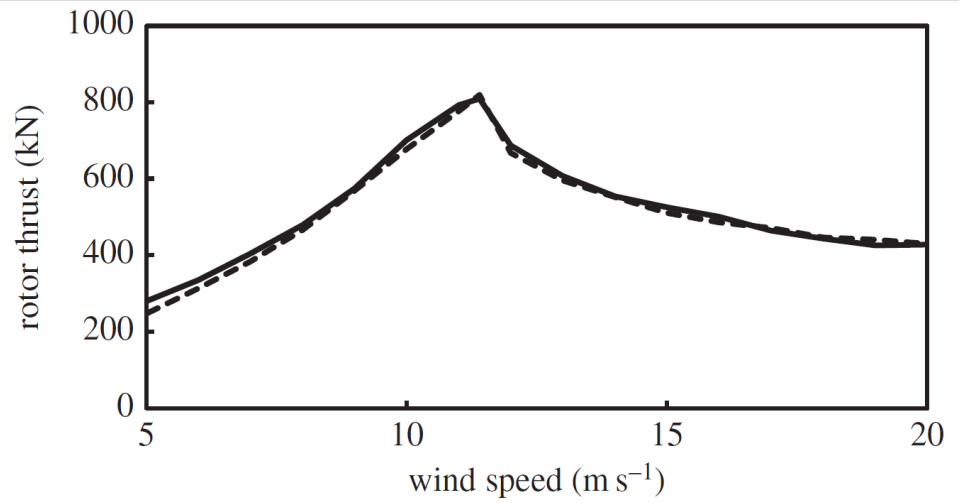

Figure 54: Rotor thrust curve of 5 MW reference wind turbine calculation data from the FAST simulator (solid) and Free Vortex Wake model (dashed) [50]

The numerical modelling of wind wakes effects will only account for the change in mean wind speed at each turbine, not the specific spatial coherence of the wind field s was studied for waves in Chapter 3. The idea of spatial wind coherence relative to multiline anchor force dynamics was entertained, but preliminary literature suggests that similar results to those obtained in the wave coherence study would be obtained, as the relationship between wind fields at two different points decays quickly with distance [86]. Furthermore, unlike wave forces on the large floating platforms, anchor forces of FOWTs are insensitive to wind turbulence, therefore any coherence between wind fields at adjacent turbines would almost certainly not be translated to the anchors. It should be noted that the concept of spatial wind coherence over the length of a wind field is distinctly different than wind wake effects changing the mean wind speed at each turbine.

6.2.2 Spar Buoy Type Platform

Only the semisubmersible platform was studied in this work thus far, and the spar buoy platform may lead to difference results. The semisubmersible system resulted in fairly insignificant effects on anchor size due to force cancellation, but the spar platform

may lead to a better conclusion in this context. This is due to the difference in platform and mooring dynamics between these two systems. Motion of semisubmersible platforms is dominated by offset (surge & heave), and large platform offset is tightly correlated with high anchor tension. In contrast, spar platform motion is dominated by rotation (pitch & roll), so anchor tensions are lower, and upwind and downwind values are closer in magnitude [80].

For a multiline anchor in a spar-platform wind farm, this will also mean that the difference between contributing line tensions on a multiline anchor will be smaller, leading to larger force cancellation and effectively smaller anchors that require less steel. Therefore, if a spar platform were to be used instead of a semisubmersible platform, the reduction in anchor steel due to smaller anchors may be quite significant, in addition to the reduction resulting from fewer number of anchors. Given that mean multiline anchor forces will be lower, there may also be a higher occurrence of multiline anchor force direction reversal.

6.2.3 Effect of Multiple Line Attachments on Anchor Performance

The connection of multiple mooring lines to a single anchor must also be examined. Conventional anchors typically have one mooring line attached, and therefore only one padeye. The increased number of padeyes per anchor in the multiline anchor system may affect the anchor's capacity to resist mooring line loads. Trenching of the mooring lines is also a noted issue in catenary mooring systems, and the effect of multiple trenches surrounding the same anchor must examined for potentially lowered capacity or accelerated degradation.

6.2.4 Effect of Anchor Placement

In an interconnected multiline anchor system, the effects of anchor placement accuracy must be examined to determine the effect on system dynamics. Due to the nonlinearity of mooring system dynamics, mooring and anchoring forces are highly sensitive to changes in mooring geometry. This sensitivity is shown in Figure 55 below.

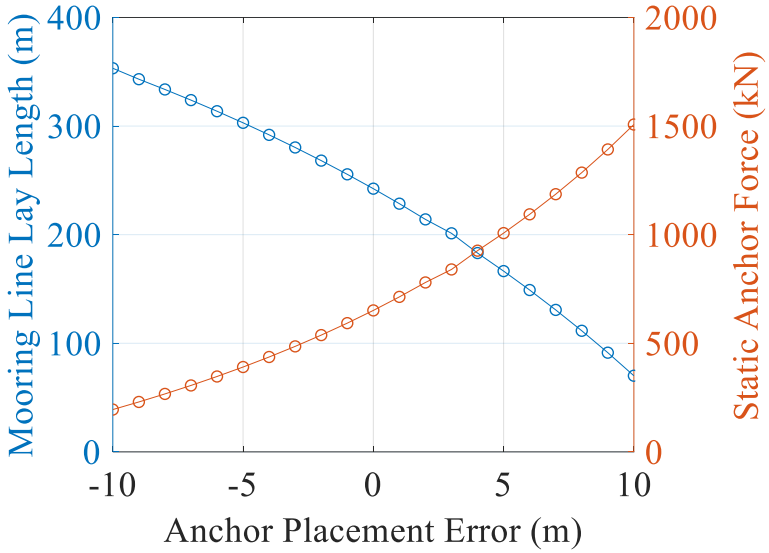

Figure 55: Effect of anchor placement error on mooring line lay length and static anchor force

Driven piles and suction caissons can be placed with a high degree of accuracy. Placement of drag embedment anchors and vertically loaded plate anchors, however, is an unpredictable function of non-homogeneous soil conditions, therefore actual placement may be significantly different from intended placement. Winching systems at the fairlead may be able to partially correct the dynamic effects of this inaccuracy by adjusting line lengths. However, the use of winching systems at every fairlead can be cost prohibitive. Anchor placement accuracy should be examined for its effect on multiline anchor force dynamics in different mooring systems, in cost trade-offs between winching systems and incorrect anchor placement. This study would be important for vertically

loaded plate anchors used as multiline anchors in soft clay, and in the drag embedment anchors used in the load ring concept discussed in the following section.

6.2.5 Load Ring Concept

Previous work has focused on anchors with axisymmetric strength like piles and suction caissons for the multiline concept, as they are naturally suited for the multidirectional loading present in the multiline system. However, most offshore floating systems utilize drag embedment anchors, as their high strength to weight ratio and low installation costs make them more cost efficient than piles and suction caissons. Drag embedment anchors are limited in their omnidirectional capacity, but a load ring concept may allow for the use of less expensive drag embedment anchors in the multiline system, as shown in Figure 56.

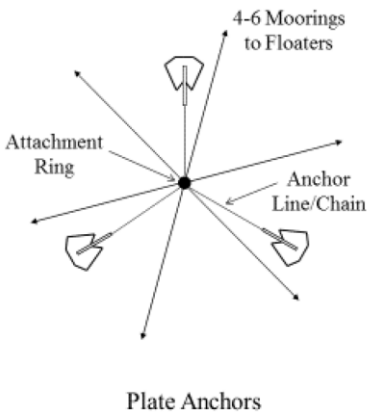

Figure 56: Load ring concept for plate anchors [29]

In this configuration, the central connecting point could still transfer the loads to the 3 drag embedment anchors without producing significant out-of-plane loading on the anchors. Load rings currently come in the form of mooring triangles or quad plates, as shown in Figure 57, which can connect 3 or 4 lines, respectively. It should be noted that the use of a load ring concept would only be economical if more than 4 lines were

attached to each anchor point. In future work, the load ring concept should be examined for its force dynamics and cost benefit potential.

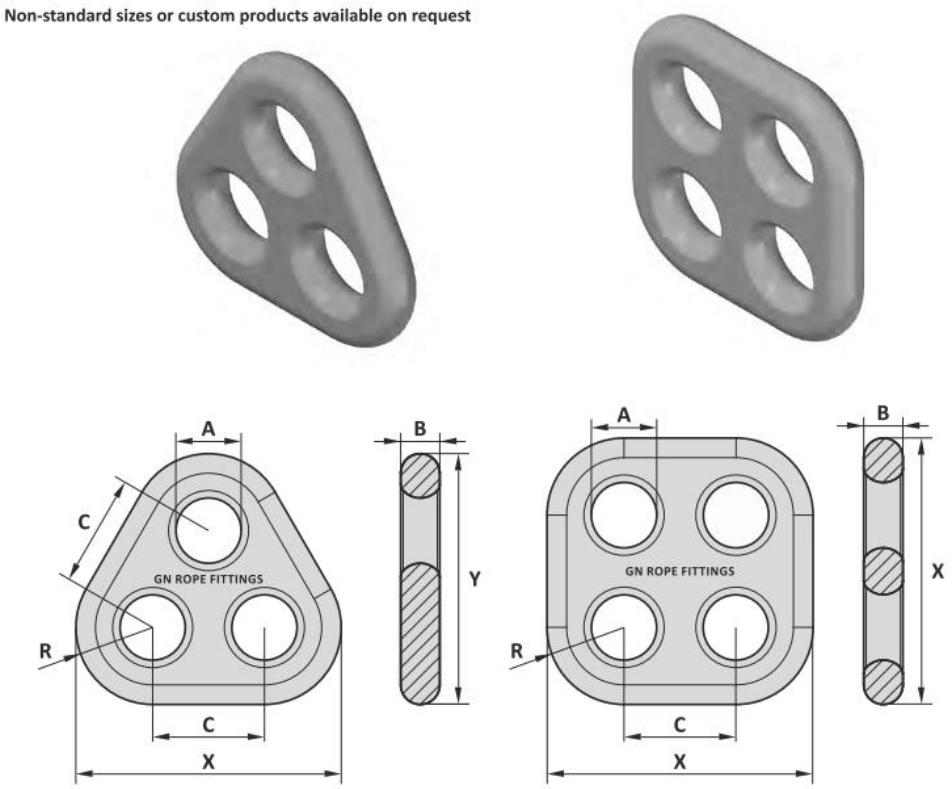

Figure 57: Mooring triangle and quad plate [87]

6.2.6 Trends in Force Dynamics with Spatial Parameters

As previously discussed, mooring line and anchor force dynamics are highly sensitive to mooring configuration. Therefore exploration into multiline anchor net force behavior with changes to spatial parameters, namely turbine spacing and water depth, must be evaluated. Partial examination of this topic has been completed in the cost analysis work in Chapter 5, but more details on the results are required. The mooring designs completed in Chapter 5 should be analyzed for trends in force dynamics relative to spatial parameters, such as mean, maximum, and standard deviation of the forces,

cyclic behavior, and force direction mean, standard deviation, and reversal. The goal of this work would be to determine if any trends exist in the multiline anchor force characteristics exist relative to the spatial parameters of water depth and turbine spacing.

6.2.7 Taut and Semi-Taut Mooring Systems

Catenary systems were studied in all previous multiline anchor analysis, given their prevalence in both planned and operating floating offshore wind concepts. However, semi-taut and taut mooring systems are used in a number of FOWT concepts and should be analyzed in the context of the multiline anchor system. While the horizontal components of the multiple connected mooring lines will still result in force cancellation, the vertical components of these lines will be additive. Therefore, the multiline anchors in taut and semi-taut mooring systems may see either increases or reductions in force, depending if the additive nature of the vertical components outweighed the cancelling nature of the horizontal components.

As discusses in Chapter 5, single-line catenary mooring systems typically utilize drag embedment anchors due to their high strength to weight ratio and cost efficiency, but due to their omnidirectional capacity, the corresponding multiline systems had to use more expensive piles and caissons for their axisymmetric capacity. Single-line semi taut and taut mooring systems are likely to use piles and suctions caisson type anchors already, due to their capacity to resist vertical forces. As a result, the implementation of the multiline anchor concept in taut and semi-taut mooring systems may result in larger reductions in anchor costs, if not outweighed by the larger anchor designs required for the additive vertical force components.

CHAPTER 7

SENSITIVITY OF THE DYNAMIC RESPONSE OF MONOPILE-SUPPORTED OFFSHORE WIND TURBINES TO STRUCTURAL AND FOUNDATION DAMPING

7.1 Introduction

The growing demand for renewable energy sources has led to the construction of many onshore wind farms in the U.S. In 2013, these farms accounted for 4.5% of the nation's annual electricity usage [6]. The U.S. Department of Energy has declared a national goal of generating 20% of the nation's electricity from renewable sources by 2030 and has stated that the least expensive way to achieve this goal includes significant development of offshore wind farms [6]. Offshore wind farms have several advantages compared to onshore wind farms including the potential to install larger turbines with higher capacities in locations with stronger and steadier winds and closer proximity to electricity demand centers. While these benefits are important, there are also many additional challenges compared to onshore wind, one of which is the presence of wave loading which can have significant power spectral density at frequencies near the natural frequency of the OWT system. Moreover, it is noted that the foundation of a typical offshore wind turbine is relatively more expensive, accounting for 27% of the initial capital costs as compared to a typical onshore foundation which accounts for 16% [88]. The relative expense of the support structure underscores the importance of minimizing structural weight to reduce both material and constructions costs. However, design must satisfy resonance avoidance requirements in addition to strength and stiffness requirements [89]. Damping is a primary factor in counteracting load amplification due to resonance,

therefore it is important to reliably estimate the magnitudes of each source of damping in the system. Of these sources, it is arguable that the least is known about foundation damping, which originates from the interaction of the foundation and the soil. Examples in the literature suggest that foundation damping can contribute up to 1.5% of critical damping [90]. Despite the significance of this source of damping, current design guidelines do not provide a method for estimating it and it is often neglected in structural design, which may result in higher than necessary costs for the support structure.

7.2 Problem Statement

The purpose of this study is to estimate the effect of foundation damping on structural demands for a wide range of wind, wave, and operating conditions. Quantifying the significance of this effect is an important step in the decision of whether design specifications should allow inclusion of foundation damping in load analysis and whether developers and designers should invest in experimental and analytical methods to estimate the magnitude of foundation damping for a particular site and structure.

Total system damping consists of multiple sources, including aerodynamic damping, hydrodynamic damping, structural damping, foundation damping, and sometimes tuned mass damping (TMD). For linear modal damping, the total system damping ratio can be defined as the summation of damping from each source,

$$\zeta_1 = \zeta_{structural} + \zeta_{TMD} + \zeta_{aero} + \zeta_{hydro} + \zeta_{foundation} \quad \textbf{(16)}$$

where ζ_1 is the total system damping ratio for the first bending mode, $\zeta_{structural}$ is the hysteretic damping ratio for the structural material, ζ_{TMD} is the oscillating tuned mass damping ratio, ζ_{aero} is the aerodynamic damping ratio, ζ_{hydro} is the wave making radiation and viscous hydrodynamic damping ratio, and $\zeta_{foundation}$ is the foundation damping ratio

[91]. Of these sources, foundation damping properties are particularly difficult to estimate due to the non-uniformity of soil, its complex nonlinear behavior under even moderate loading, and the difficulty of obtaining detailed site characterization data. Carswell et al. (2015) investigated the significance of foundation damping on monopile-supported OWTs subjected to extreme storm loading using a linear elastic two-dimensional finite element model. This chapter investigates how consideration of foundation damping though an increase in the overall structural damping affects both load maxima and fatigue damage accumulation for an example monopile-supported OWT.

7.3 Methods

This investigation is structured as a parameter study with the total system damping ratio ζ_1 being the varied parameter and the peak structural demand and fatigue damage being the response quantities of interest. By formulating the problem as a parameter study it is possible to identify and illustrate trends in the effect of damping on dynamic response and to provide guidance for further, more detailed investigation of foundation damping effects. Here, an example monopile-supported OWT is analyzed dynamically for peak mudline bending moment and fatigue damage accumulation for wind and wave conditions ranging from mild to extreme and for damping ratios that cover the range of plausible contributions from the foundation system. In this section, details are provided about the structural model and software employed by this study and the input and outputs considered.

7.3.1 Models and Software

7.3.1.1 Simulation Software

OWT behavior is analyzed for a 5 MW reference turbine using the National Renewable Energy Laboratory's (NREL) open-source wind turbine simulation software FAST [38],

which is a dynamic nonlinear analysis program that can model structural loads caused by the stochastic environment (wind and waves) and mechanical load effects from turbine operation. Details about modeling assumptions in FAST are available in the software documentation, but the software features that are particularly relevant to this study are summarized here:

1. Stochastic time and spatially varying three-dimensional wind fields.
2. Calculation of aerodynamic forces using blade element momentum theory.
3. Stochastic linear irregular wave time histories.
4. Calculation of hydrodynamic forces using the Morison equation.
5. Four degree of freedom modal analysis of the monopile/tower support structure including P-Δ effect.

7.3.1.2 Reference Turbine

The NREL 5 MW reference turbine is used for the OWT model due to its prevalence in the field of offshore wind energy research. This turbine is promulgated for use by the research community and is reflective of the properties of a generic utility-scale turbine [35]. Properties of the turbine are provided in Table 1 and Figure 1. A monopile-supported foundation is considered because it best represents current practice – a majority (65%) of installed OWTs utilize monopile-type foundations, and it is anticipated that they will continue to dominate the industry [93].

Table 30: Gross properties for the NREL 5 MW reference offshore wind turbine [35].

Property	Value/description
Rating	5 MW
Rotor Orientation, Configuration	Upwind, 3 Blades
Control	Variable Speed, Collective Pitch
Rotor, Hub Diameter	126 m, 3 m
Hub Height	90 m
Cut-In, Rated, Cut-Out Wind Speed	3 m/s, 11.4 m/s, 25 m/s
Rotor Mass	110,000 kg
Nacelle Mass	240,000 kg
Tower Mass	347,460 kg
Coordinate Location of Overall Center of Mass	(-0.2 m, 0.0 m, 64.0 m)
Natural frequency	0.27 Hz

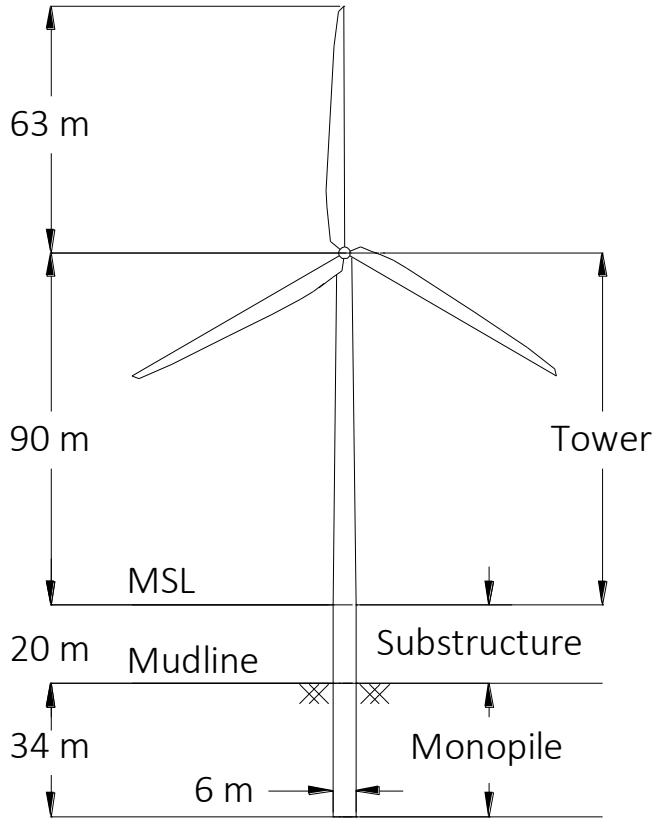

Figure 58: Schematic of the NREL 5MW with fixed bottom and supported by a monopile foundation [92]. MSL = Mean Sea Level.

Monopiles can be constructed in shallow water depths up to ~30 m [9]. The water depth considered for this study is 20 meters, a depth reflective of potential east coast installation

locations [9] and comparable to many other publications that consider the NREL 5MW reference offshore turbine.

7.3.1.3 Approximation of foundation damping by structural damping

Foundation damping is a dynamic property of the support conditions resulting from soil structure interaction. It is dependent on the strength and stiffness of the support and surrounding soil, and can be described as the mechanism in which energy is dissipated when cyclic motion in the soil takes place. FAST does not include the capability to model soil nonlinearity which is the source of foundation damping, therefore foundation damping is modeled with equivalent modal damping and added to the structural damping input value. In reality, foundation damping is applied as a distributed force below the mudline and is dependent on many more factors than just velocity, so this simplification results in a loss of frequency and amplitude dependence that appears in detailed geotechnical modeling of foundation dynamics. However, modeling the role of foundation damping in the dynamic response of an OWT through an increase in the total structural damping modeled in FAST allows for efficient simulation of OWT response in this parameter study. In addition, this simplification is reasonable because the emphasis of this study is placed on effects of the increase in system damping due to increased foundation damping, not on the foundation damping values themselves.

The structural damping value in FAST is inputted directly by the user, while hydrodynamic damping (ζ_{hydro}) and aerodynamic damping (ζ_{aero}) values are generated through dynamic analyses in FAST. Tuned mass damping (ζ_{TMD}) is 0% because the NREL 5MW reference offshore turbine does not include a tuned mass damper. Structural damping in FAST is modeled with implementation of simplified Rayleigh damping by the

designation of four damping ratios corresponding to the 1st and 2nd fore-aft (FA) modes and the 1st and 2nd side-side (SS) modes. The model includes a structural damping ratio set equal to a constant value of 1.0%, which is a standard value for the NREL 5 MW OWT supported by a steel tower and monopile [35] and represents the inherent damping of the structural material. The literature on the magnitude of foundation damping determined via free vibration and log decrement analyses suggests that it can provide a contribution of 0.17%-0.28% of critical damping when estimated numerically [92] and 0.25%-1.5% when back-calculated experimentally [90], [94]. It is noted that these estimates of foundation damping contribution are highly sensitive to modeling assumptions and experimental conditions, meaning that true foundation damping contributions could be different due to variation in soil properties and many other factors. This range of foundation damping values stated the literature has already been converted equivalent modal damping, therefore a range of foundation damping ratios inputs between 0% and 2% added to the structural damping value are analyzed in this study.

Numerical experiments by the authors have indicated that, due to complexities in the way the tower mode shapes and the added mass of the rotor-nacelle-assemble are considered in FAST, the target structural damping ratios specified in the FAST input files are not realized when the resulting model is exercised in a free vibration analysis. Rather, the model exhibits substantially less damping than is specified in the input files. Figure 59 shows the relationship between the input structural damping ratio and that calculated using the log decrement method applied to the tower-top displacement in a free vibration analysis executed with no external wind or wave loading and with the rotor and blades parked and feathered. The figure shows that the effective structural damping in the model is

approximately 30%-40% of that specified in the input file. Even though the model includes additional damping due to the explicit modeling of aerodynamic and hydrodynamic forces which resist structural motion, these additional sources are expected to be minimal since the rotor and blades are parked and feathered and since there is no external wind or wave loading.

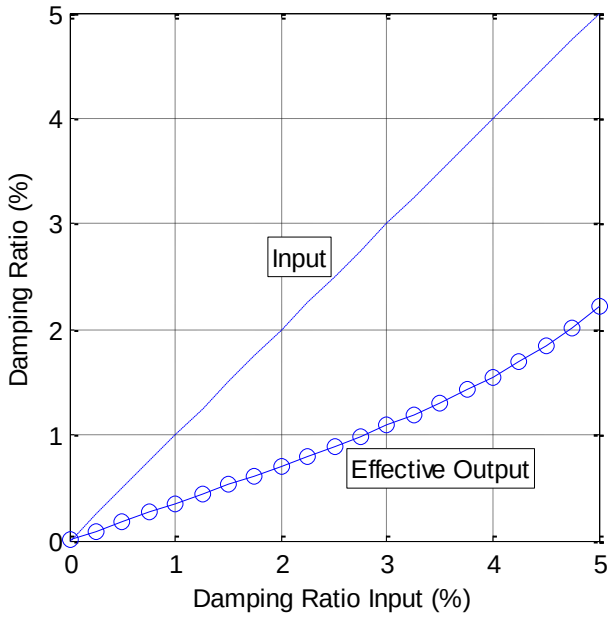

Figure 59: Inconsistencies in FAST between the damping ratio specified as input and that calculated based on a log decrement analysis of the tower top displacement subjected to free vibration.

Therefore, to account for this inconsistency and still model the full range of foundation damping between 0 and 2%, a range of structural damping ratios between 1% (i.e., structural damping only) and 5% (i.e., 1% structural damping plus approximately two times the maximum foundation damping of 2%) is specified as input into the FAST analyses.

7.3.2 Summary of Input Parameters

A summary of input parameters considered in this study is provided in Table 31. The first three rows in the table provide the range of damping ratio, wind speed, and wave

height selected for the parameter study while the remaining rows give parameters that are held constant across all simulations.

Table 31: Summary of FAST input parameters.

Parameter	Value/Description
Damping ratios	1%, 2%, 3%, 4%, 5%
Wind speeds, V	3 m/s, 11.4 m/s, 25 m/s, 30 m/s
Significant wave heights, H_s	0 m, 2 m, 4 m, 6 m, 8 m
Water depth	20 m
Platform model	Fixed bottom offshore
Wind turbulence model	IEC Kaimal
Turbulence intensity	11%
Incident wave kinematics model	JONSWAP/Pierson-Moskowitz spectrum (linear irregular)
Wind-wave alignment	Co-directional

Selected wind speeds are chosen because they correspond to important operational states for the NREL 5 MW turbine: the cut-in speed (3 m/s) is the minimum speed at which the turbine operates, the rated speed (11.4 m/s) is the wind speed at peak power generation, and the cut-out speed (25 m/s) is the maximum speed at which the turbine operates. The 30 m/s wind speed is included in the study to examine non-operating conditions when the turbine is parked (blade movement restricted by brake) and blades are feathered. A turbulence intensity of 11% is chosen because it is reflective of typical offshore conditions and is commonly used in OWT research.

The lower limit of significant wave height range (0 m) is chosen to analyze the case of no wave loading, while the upper limit of the significant wave height range (8 m) is chosen based on breaking wave criteria, where H/d = 0.78 is generally considered to define the onset of breaking waves [95]. For the 20 m water depth in this research, the corresponding breaking wave height is 15.6 m, which becomes the limiting maximum value of wave height. Maximum wave height is defined by $1.86H_s$ [96], therefore the

significant wave height for the onset of breaking waves in 20 m water depth is approximately 8 m.

Wave period is calculated according to IEC standard 61400, given by:

$$\mathbf{11.1} \times \sqrt{\frac{H_s}{g}} \leq \boldsymbol{T} \leq \mathbf{14.3} \times \sqrt{\frac{H_s}{g}} \qquad \textbf{(17)}$$

where T is the wave period, H_s is the significant wave height, and g is gravity [60]. The lower limit factor of 11.1 is used in this study to maximize the wave power spectral density associated with the natural frequency of the structure (0.27 Hz). This models the wave loading within this range that is expected to cause the largest loads and to have the most waves impacting the structure in a given time, thereby maximizing fatigue damage estimates. These calculated values of wave periods are used for the peak spectral period inputs in FAST.

Six 1-hour simulations are completed for each input value of damping ratio - 1, 2, 3, 4, and 5% - and for each combination of wind speed and wave height in accordance with IEC standards [60]. Each of the 6 simulations uses a different set of seeds to initialize the random number generators which initiate the stochastic wind and wave histories. The same 6 sets of seeds are used for each damping ratio and for each combination of wind speed and wave height to remove estimation variability from the comparison of dynamic response across wind, wave, and damping conditions. For each combination of wind speed and wave height conditions, 36 simulations are carried out (5 damping ratios and 6 seed sets), resulting in a total of 600 1-hr simulations in FAST.

7.3.3 Maximum Load Definition

For simplicity, the maximum load considered in this study is the resultant mudline bending moment, calculated by combining the fore-aft (FA) and side-side (SS) moments

provided in the FAST output. In particular, resultant moment time histories are generated by calculating the vector sum of the FA and SS moment output values from FAST at every time instant, as shown in Figure 3.

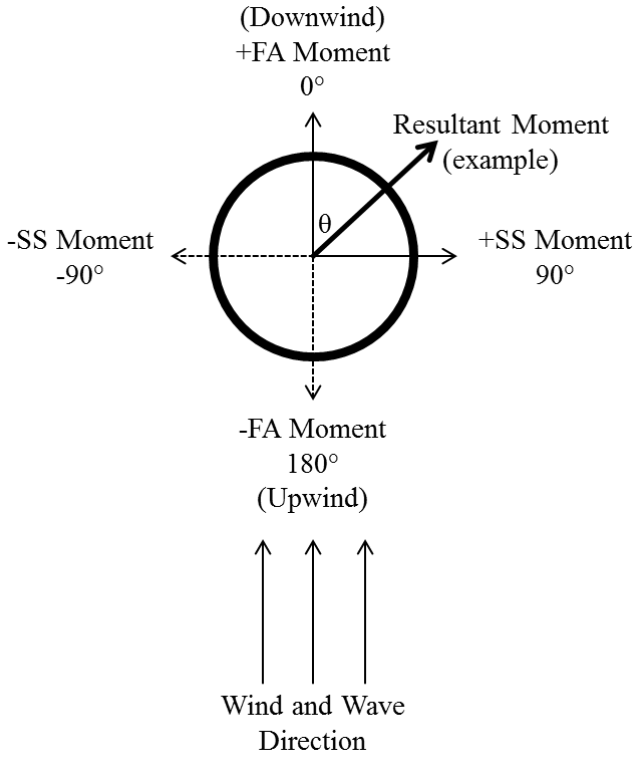

Figure 60: Top view of monopile cross-section at the mudline showing the fore-aft (FA) and side-to-side (SS) direction and an example direction of the resultant moment.

For each combination of wind speed, wave height, and damping ratio, the maximum resultant moment is calculated for each of the 6 independent simulations (corresponding to different random number seeds) and the peak response is taken to be the average of those

6 maxima. This average is typically used in industry and provides a more stable estimator of the extreme loads than would the maximum of a single simulation.

7.3.4 Fatigue Damage

The second portion of the research investigates the effects of damping on fatigue damage accumulation in the cross-section located at the mudline of the monopile. Fatigue damage is calculated by selecting a material stress-lifetime (S-N) curve that best models the turbine's cross-section at the mudline [97], generating combined bending/axial stress time histories from FAST output for circumferential orientations spaced at 5 degree increments around the base, executing rainflow cycle counting, applying the Goodman correction for mean stress effects [98], and using the Palmgren-Miner rule [97] to compute the fatigue damage during the one hour simulations described above. This fatigue analysis gives estimates of the accumulated fatigue damage that occurs during a one hour simulation under specified wind speed, wave height, and damping ratio and provides guidance on how foundation damping may mitigate fatigue damage over a wide range of environmental conditions.

Fatigue damage analysis is performed following the Recommended Practice DNV-RP-C203 [97], which is valid for examining fatigue damage in the high cycle region with stress values up to 550 MPa (DNV 2005). The use of this practice is appropriate here given the high number of cycles associated with the environmental loading on OWTs and the stress magnitudes calculated by FAST. The DNV Recommended Practice states that accumulated fatigue damage may be calculated based on the stress-life fatigue approach under the assumption of linear cumulative damage (Palmgren-Miner rule ,Veritas 2005), which states that,

$$\boldsymbol{D = \sum_{i=1}^{k} \frac{n_i}{N_i} \leq \eta} \qquad \textbf{(18)}$$

where D is accumulated fatigue damage, k is the number of stress range blocks, n_i is the number of stress cycles in stress range block i, N_i is the number of cycles to failure at stress range corresponding to block i, and η is the usage factor (DNV 2005).

7.3.4.1 Selection of a Stress-Life Curve

The S-N curve considered here is the C1 curve for offshore steel structures in seawater with cathodic protection [97]. This curve is appropriate for the tubular steel pipe connecting the turbine to the foundation at the mudline, assuming the connection is a two-sided circumferential butt weld dressed flush [97]. The curve is governed by

$$\boldsymbol{logN = log\bar{a} - mlog\Delta\sigma} \qquad \textbf{(19)}$$

where N is the predicted number of cycles to failure for stress range $\Delta\sigma$, $log\,\bar{a}$ is the intercept between the log N-axis and the S-N curve, m is the negative inverse slope of the S-N curve, and $\Delta\sigma$ is stress range. For the C1 curve in the range $N \leq 10^6$ cycles, the values for $log\,\bar{a}$ and m are 12.0 and 3.0 respectively. For $N > 10^6$ cycles, the values for $log\,\bar{a}$ and m are 16.1 and 5.0, respectively. The design S-N curve is based on the mean-minus-two-standard-deviation curve for relevant experimental data, and is therefore is associated with a 97.7% probability of survival (DNV 2005). As shown in this curve, larger amplitude stresses correspond to shorter lifespans due to their nonlinearly larger effect on fatigue damage accumulation.

7.3.4.2 Stress Time History

The total stress in the base at any time instant, σ_{total}, is calculated by the sum of the bending stress and axial stress,

$$\boldsymbol{\sigma_{total}(t,\theta) = \sigma_b(t,\theta) + \sigma_n} \qquad \textbf{(20)}$$

where σ_b is the bending stress caused by the resultant bending moment, t is time, θ is the angle from the fore-aft downwind direction as shown in Figure 60 and σ_n is the constant axial stress (15.1 MPa) due to the self-weight of the combined rotor nacelle assembly (RNA), tower, and monopile. Note that the axial stress induced by gravity is considered to be time invariant and constant around the circumference of the monopile, and that this assumption neglects nonlinear effects and the small bending moment and resulting stress induced by the small eccentricity between the RNA center of mass and the centerline of the tower. The resultant bending stress is calculated at 5° increments around the base of the turbine. It is necessary to calculate individual stress time histories at incremental points because damage varies with circumferential orientation around the base. Relevant properties of the monopile's tubular steel pipe at the mudline are summarized in Table 32.

Table 32: Base properties of NREL 5-MW turbine used for stress calculations [35]

Turbine Base Property	Value
Outer diameter	6 m
Wall thickness	0.027 m
Moment of inertia	2.26 m^4
Cross sectional area	0.507 m^2
Self-weight at base	7.64 MN

7.3.4.3 Rainflow Counting and Mean Stress Effects

Due to the high variability of the turbulent winds and irregular waves modeled in FAST, the total stress time histories computed display a large range in cycle amplitude. The MATLAB rainflow counting function, *rainflow*, is used to extract cycle counts, amplitudes, and means from each stress time history.

Most cycles in the operating cases have nonzero mean stresses because of the nonzero average thrust acting on the rotor. The C1 S-N curve from Recommended Practice C203 is generated based on fully reversed stress cycles with zero mean stress. To consider

mean stress effects in the prediction of fatigue damage, the Goodman relationship [98] is used, which states

$$\frac{\sigma_a}{\sigma'_e} + \frac{\sigma_m}{\sigma_u} = 1 \qquad (21)$$

where σ_a is the stress amplitude, σ_m is the mean stress, σ_u is the ultimate strength of the steel (450 MPa [96]), and σ'_e is effective stress amplitude. The Goodman effective stress amplitude, σ'_e, is the equivalent stress amplitude for fully reversed zero mean stress criteria. The results from the rainflow counting are sorted by both amplitude and mean (20 by 20 binning, as recommended by DNV (2005)), and the Goodman correction is applied to each bin.

7.3.4.4 Average maximum fatigue damage

After pairs of effective stress amplitude and cycle count are calculated for each of the simulation runs, these pairs are used as input to the Palmgren-Miner equation to calculate the fatigue damage accumulated during the simulation. Purely compressive stress cycles are generally not considered to contribute to fatigue damage. Therefore, when computing the effective stress, if the sum of the mean stress and stress amplitude of the bin is negative (i.e., if the bin's stress cycle range is entirely compressive), those cycles are not included in the Palmgren-Miner fatigue damage accumulation calculation. Effective stress amplitudes are doubled to find the effective stress range for use in the S-N curve, which is defined in terms of stress range rather than amplitude. This modified Palmgren-Miner damage equation states,

$$D = \sum_{i,j=1}^{k} \frac{n_{ij}}{N_{ij}} \leq \eta \qquad (22)$$

where n_{ij} is the number of stress cycles at amplitude i and mean stress j, and N_{ij} is the number of cycles to failure for the Goodman effective stress range at amplitude i and mean

stress *j*. Stress concentration factors (SCF) that may act to increase stresses are neglected here since the emphasis is on comparison between fatigue damage at different damping ratios and environmental conditions, rather than on the absolute value of that fatigue damage. The same process of averaging the 6 one-hour simulations is used to find the average values of *D* at each 5° increment. For each combination of wind speed, wave height, and damping ratio, only the circumferential orientation of maximum damage and the associated damage value is used for comparison between cases to evaluate effects of increased damping.

7.4 Results

As expected, increased damping is found to decrease the average maximum resultant mudline moment and the average maximum damage accumulation in all combinations of wind speed and wave height. In the following subsections detailed descriptions of these effects are given for the maximum resultant moment and fatigue damage cases.

7.4.1 Effects of increased damping on maximum mudline moment

Increased damping decreases the amplitude of the resultant moment in all cases, as demonstrated by a sample resultant mudline moment time history shown in Figure 61.

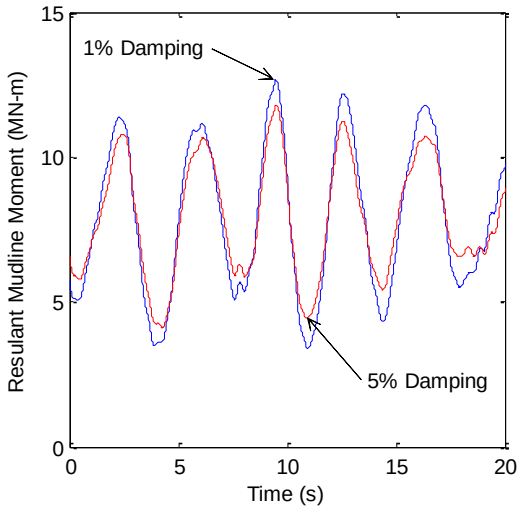

Figure 61: The effect of increasing damping from 1% to 5% on the resultant mudline moment for a wind speed of 3 m/s, a significant wave height of 2 m, and operational conditions.

The maximum values of resultant moment for each case are shown in Table 33, as calculated by averaging the maxima for the 6 distinct seeds. The shading in the table indicates magnitude, as detailed in the scale provided; the smallest moments are shaded green, and the largest moments are shaded red. The largest estimate for the resultant moment at the mudline is 132 MN-m, which is about one-half of the yield moment, 260 MN-m, of the cross-section of the monopile at the mudline. This moment was estimated for all considered damping ratios for the rated wind speed (11.4 m/s, the operational spend when the average rotor thrust is largest) and the significant wave height of 8 m.

Table 33: Average maximum values from six one hour-simulations for the resultant mudline moment, MN-m, for various combinations of damping ratio, wind speed, wave height and operational conditions.

Smallest Moment — **Largest Moment**

11.5 MN-m **67 MN-m** **132.2 MN-m**

		Damping Ratio, %				
		1	2	3	4	5
		Wind Speed 3 m/s (cut-in; operational)				
Significant Wave Height, m	0	11.7	11.6	11.6	11.5	11.5
	2	26.3	25.9	25.6	25.4	25.2
	4	34.6	34.2	34.0	33.8	33.7
	6	49.9	49.4	49.1	48.8	48.5
	8	63.4	63.4	63.4	63.4	63.4
		Wind Speed 11.4 m/s (rated; operational)				
Significant Wave Height, m	0	95.6	95.1	94.8	94.5	94.3
	2	102.1	101.6	101.3	101.0	100.7
	4	109.2	108.9	108.6	108.3	108.1
	6	116.2	115.9	115.7	115.5	115.3
	8	132.2	132.2	132.2	132.2	132.2
		Wind Speed 25 m/s (cut-out; operational)				
Significant Wave Height, m	0	70.6	69.7	69.0	68.5	68.1
	2	74.0	73.4	72.9	72.4	71.9
	4	77.0	76.0	75.4	75.0	74.6
	6	80.9	80.4	80.1	79.9	79.6
	8	93.9	93.4	93.0	92.8	92.6
		Wind Speed 30 m/s (parked and feathered; non-operational)				
Significant Wave Height, m	0	31.3	30.2	29.4	28.5	28.0
	2	35.3	32.8	31.3	30.2	29.2
	4	40.9	39.1	37.0	35.5	34.5
	6	53.0	50.3	48.7	47.8	47.0
	8	63.2	61.3	60.8	60.5	60.3

The effect of increasing damping is evaluated by calculating the percent reduction in the maximum value as compared to the value calculated for a damping ratio of 1%, as shown in Table 34. Bolded values highlight the maximum reductions for each wind speed case, and the darkness of the red and green shading indicates the magnitude of the moment and percent reduction values, respectively.

Table 34: Percent reduction in resultant moment as compared to value at 1% damping ratio for various combinations of damping ratio, wind speed, wave height and operational conditions.

		Damping Ratio, %				
		1	2	3	4	5
		Resultant Moment, MN-m	Percent Reduction			
Wind Speed 3 m/s (cut-in; operational)						
Significant Wave Height, m	0	11.7	0.7%	1.3%	1.8%	2.2%
	2	26.3	**1.4%**	**2.5%**	**3.4%**	**4.2%**
	4	34.6	1.1%	1.8%	2.2%	2.5%
	6	49.9	0.8%	1.5%	2.1%	2.7%
	8	63.4	0.0%	0.0%	0.0%	0.0%
Wind Speed 11.4 m/s (rated; operational)						
Significant Wave Height, m	0	95.6	**0.5%**	**0.8%**	**1.1%**	**1.4%**
	2	102.1	0.4%	0.8%	1.1%	1.3%
	4	109.2	0.3%	0.6%	0.8%	1.0%
	6	116.2	0.2%	0.4%	0.6%	0.8%
	8	132.2	0.0%	0.0%	0.0%	0.0%
Wind Speed 25 m/s (cut-out; operational)						
Significant Wave Height, m	0	70.6	**1.3%**	**2.3%**	**3.0%**	**3.6%**
	2	74.0	0.9%	1.6%	2.2%	2.8%
	4	77.0	1.2%	2.1%	2.6%	3.1%
	6	80.9	0.5%	0.9%	1.2%	1.6%
	8	93.9	0.5%	0.9%	1.2%	1.4%
Wind Speed 30 m/s (parked and feathered; non-operational)						
Significant Wave Height, m	0	31.3	3.3%	6.1%	8.8%	10.5%
	2	35.3	**7.2%**	**11.3%**	**14.5%**	**17.3%**
	4	40.9	4.5%	9.7%	13.2%	15.6%
	6	53.0	5.1%	8.0%	9.8%	11.2%
	8	63.2	2.9%	3.7%	4.2%	4.5%

For the operational cases (wind speeds 3 m/s, 11.4 m/s, and 25 m/s), the increase in damping ratio has a small effect on moment reduction. For the non-operational cases (wind

speed 30 m/s), the increase in damping ratio has up to a 17% reduction in moment. This difference in load reduction between the operational and non-operational cases is explained by aerodynamic damping. In the operational cases, where the resultant moment at any time instant is approximately in the FA downwind direction (Figure 60), the aerodynamic damping in the fore-aft direction generated by the spinning blades provides a significant amount of the system's total damping, therefore changes in foundation damping have a small effect. As a point of comparison, the fore-aft aerodynamic damping ratio for the 1.5MW NREL reference turbine has been estimated to be between 3.7% and 5.4% of critical during operational conditions [99]. In parked and feathered cases, the lack the of aerodynamic damping allows for foundation damping to account for a greater portion of the total system damping, therefore changes in foundation damping have a larger effect on the loading.

The nature of aerodynamic damping also explains why, amongst the operating cases, the 3 m/s case sees the largest percent reduction as compared to the 11.4 and 25 m/s cases. Aerodynamic damping contribution is dependent on the characteristics of the wind; for lower wind speeds like 3 m/s, less aerodynamic damping in the fore-aft direction is present, allowing foundation damping to play a stronger role in total system damping. The most aerodynamic damping is present in the fore-aft direction for the 11.4 and 25 m/s wind speed cases, therefore the resultant moment in these cases undergoes the least effect from changes in foundation damping. Magnitudes of fore-aft aerodynamic damping for different wind speeds and operational conditions can be determined via the methods described in Valamanesh and Myers (2014).

The reduction in moment due to increased damping does not vary linearly with wave height. The maximum reductions in moment occur for the 0 or 2 m significant wave height cases for all wind speeds. This is due to the wave conditions in these cases having significant power spectral density at frequencies near the turbine's natural frequency and blade passing frequencies. The NREL 5MW fixed bottom offshore monopile reference turbine in 20 m of water depth has a natural frequency f_n of 0.27 Hz, as determined from free vibration simulations in FAST (Carswell). The 1P and 3P blade passing frequencies, f_{1P} and f_{3P}, of the NREL 5MW are 0.20 and 0.34, respectively [100]. The wave period used for the peak spectral period input for each significant wave height is determined via eqn (2), and the associated frequency is the inverse of this value as shown in Table 35.

Table 35: Peak spectral loading frequencies for each significant wave height and the ratio of these frequencies to the NREL 5MW natural, 1P, and 3P frequencies.

Significant Wave Height, (m)	Peak Spectral Wave Loading Frequency, f_{wave} (Hz)	Frequency Ratios		
		f_{wave}/f_n	f_{wave}/f_{1P}	f_{wave}/f_{3P}
0	∞	∞	∞	∞
2	0.20	0.74	1.00	0.59
4	0.14	0.52	0.71	0.41
6	0.12	0.43	0.58	0.34
8	0.10	0.37	0.50	0.29

A frequency ratio of 1.0 corresponds to conditions in which the wave loading has a peak spectral frequency equivalent to the turbine's natural frequency or blade passing frequency. The turbine's natural frequency (0.27 Hz), 1P frequency (0.20 Hz), and 3P frequency (0.33 Hz) all fall between the peak spectral wave loading frequencies at 0 m (∞ Hz) and 2 m (0.20 Hz), which generates the most load amplification compared to other significant wave height cases. Since dynamic response of a system is most sensitive to damping near the

resonant frequency [101], the effects of increased damping are most significant in cases where loading experiences the most amplification, when frequency ratios are closest to 1.0.

7.4.2 Effects of increased damping on fatigue damage accumulation

Increased damping decreases the fatigue damage accumulation in all combinations of wind speed and significant wave height. This is consistent with the reductions in mudline moment results described in the previous section, since damage is a function of moment and the resulting stress values.

7.4.2.1 Rainflow counting and 2D binning of total stress cycle amplitudes and means

The stochastic nature of the environmental loading from the turbulent winds and irregular waves results in significant randomness within a stress time history and significant variability between nominally identical simulations. Figure 5 shows this in total stress time history samples for nominally identical simulations.

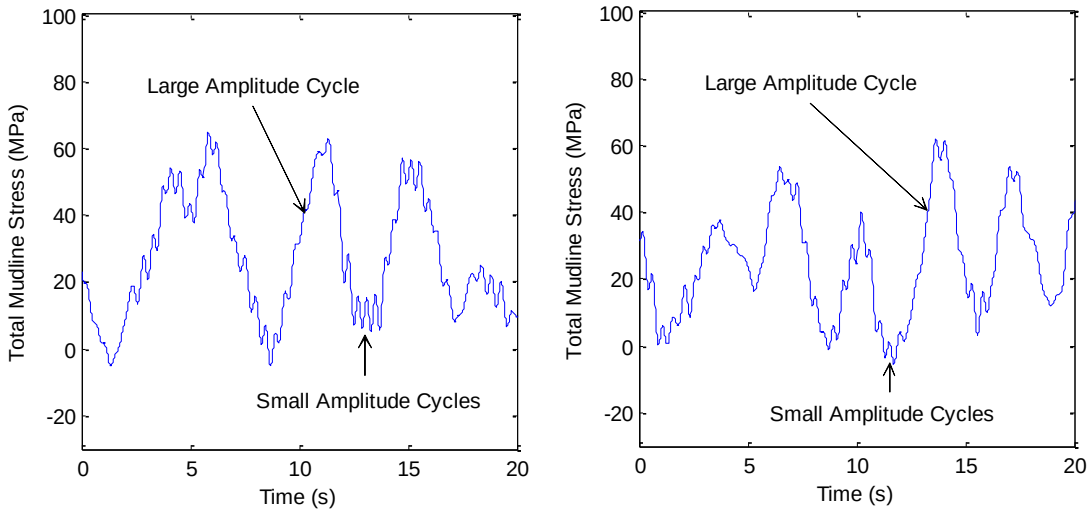

Figure 62: Variations in total stress cycle amplitude for a wind speed of 25 m/s (operational), a significant wave height of 8 m, and a damping ratio of 1% for Seed 1 (a) and Seed 2 (b)

The rainflow counting process described previously is used to decompose each stress time history into an amplitude and mean for every stress cycle. It is found that most cycles located in the FA upwind circumferential orientation on the cross-section (180° see Figure 60) for the operating cases have nonzero mean stresses, due to the presence of the non-zero thrust acting in the fore-aft direction. An example of the presence of non-zero mean stresses is shown in Figure 63.

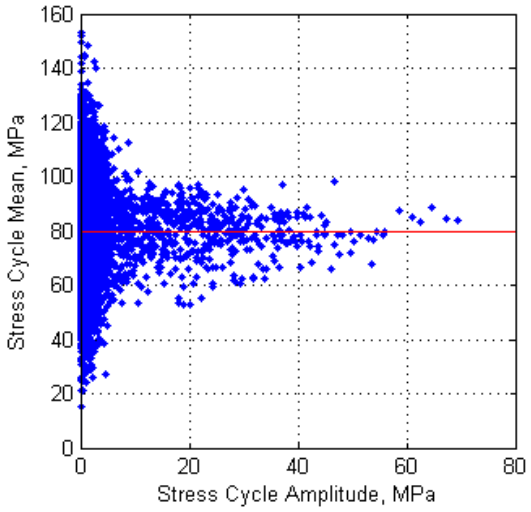

Figure 63: Total stress cycle amplitude versus stress cycle mean from rainflow counting for wind a speed of 11.4 m/s (operational), a significant wave height of 8 m, a damping ratio 1%, and 180° FA upwind circumferential orientation on the mudline cross-section of the monopile (see Figure 60) to show need for incorporation of mean stress effects.

This non-zero mean stress results from the interaction between the wind and blades when the turbine is operational; parked and feathered conditions exhibit mean stresses close to zero. Figure 63 shows a selected case in which maximum loading occurs (wind speed 11.4 m/s, significant wave height 8 m, damping ratio 1%), therefore the mean stress is significantly larger than the stress amplitude. The variations in total stress from wind turbulence and wave irregularity is minimal compared to the large constant blade-wind

interaction stress inherent in peak power production conditions. An example of 2D binning used to analyze the extracted total stress cycle amplitudes and means is shown in Figure 64.

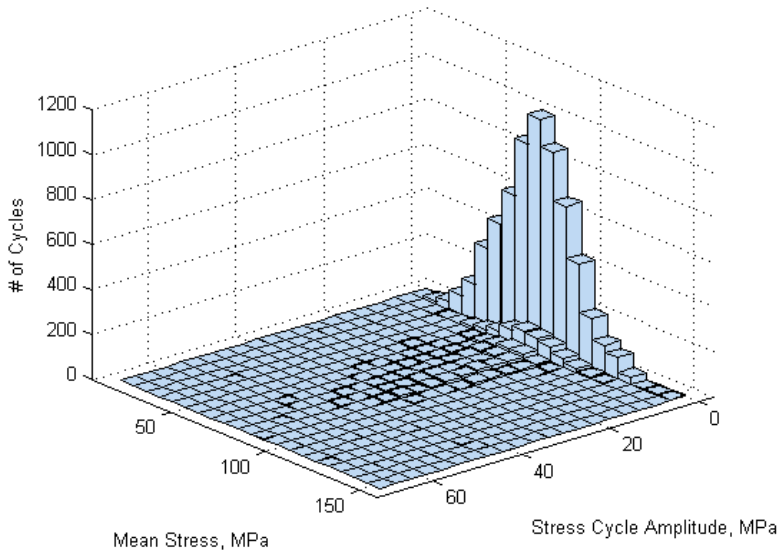

Figure 64: 2D Binning histogram of total stress amplitude bins, mean stress bins, and number of cycles in the bin for a wind speed of 11.4 m/s, a significant wave height of 8 m, a damping ratio of 1%, and 180° FA upwind circumferential orientation on the mudline cross-section of the monopile (see Figure 60).

In operating cases, the mean total stress in the FA upwind circumferential orientation remained approximately the same across all wave heights. The mean stress results reflect values shown in Table 33, as mean bending stress is a closely related to moment – the rated wind speed cases have the highest magnitude mean bending stresses (~95 MPa) and the cut-in have the lowest (~10 MPa). In parked and feathered cases, the mean FA upwind bending stress magnitude are more sensitive to wave loading due to the lack of blade-wind interaction (~8 MPa at 0 m wave height to ~16 MPa at 8 m wave height).

7.4.2.2 Damage accumulation for the circumferential orientation with maximum damage

The circumferential orientation of maximum damage can be seen in Table 36. A diagram showing the orientation of the angle measure is shown in Figure 60. All of the results in this section are provided for the circumferential orientation with maximum damage.

Table 36: Circumferential orientation of maximum damage on the mudline cross-section of the monopile. Angle reference point is provided in Figure 60.

		Wind Speed, m/s			
		3	**11.4**	**25**	**30**
Significant Wave Height, m	**0**	180°	180°	-170°	90°
	2	180°	180°	-175°	90°
	4	180°	180°	-175°	165°
	6	180°	180°	-175°	180°
	8	180°	180°	-175°	180°

In the cut-in, rated, and cut-out wind speed cases, the FA upwind circumferential orientation (180°) is generally found to accumulate the most damage because this circumferential orientation experiences the highest mean tensile stress. Due to the blade-wind interaction, the turbine is always bending downwind in operating cases, creating the highest tensile bending stress in the FA upwind circumferential orientation and the highest compressive stresses in the FA downwind circumferential orientation (0°, see Figure *60*), as shown in Figure 65. The circumferential orientation of maximum damage favors -170° and -175° in the cut-out wind speed case due to the lack of symmetry of the blades, which becomes a more pronounced effect at high wind speed.

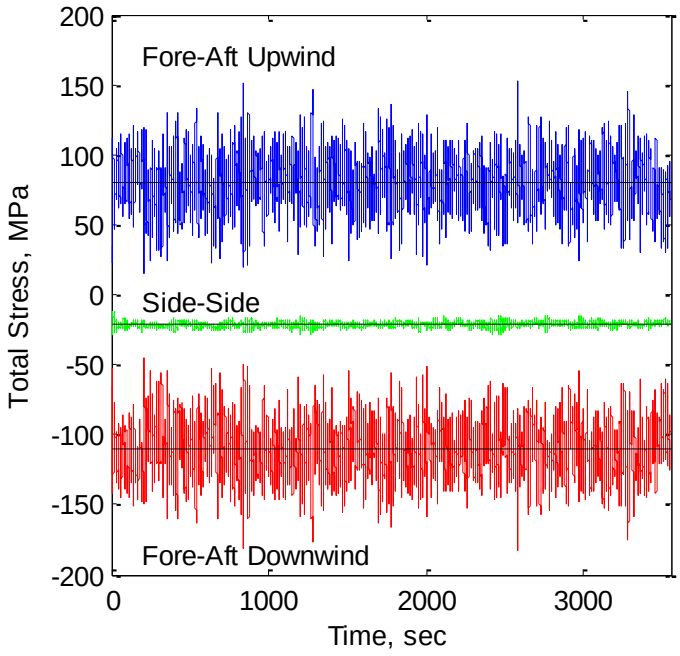

Figure 65: Total stress time histories and means of fore-aft upwind (180°), side-side (90°), and fore-aft downwind (0°) for a wind speed of 11.4 m/s, a significant wave height of 8 m, and a damping ratio of 5%.

The lack of symmetry about zero stress in Figure 65 is due to the constant axial compressive stress and approximately constant bending stress resulting from the overturning moment acting on the rotor. Since the additional compressive axial stress acts equally in all circumferential orientations around the base, the bending stress wind and wave loading governs the circumferential orientation of maximum fatigue damage values. Additionally, entirely compressive stress cycles such as those experienced in the FA downwind circumferential orientation are not considered in the Palmgren-Miner model to contribute to fatigue damage.

In the parked and feathered cases with significant wave height equal to 0 and 2 m, the SS circumferential orientation (90°) is found to accumulate the most damage, though it should be noted that the absolute levels of damage in these cases are low due to the low

wave heights. When the blades are feathered, this orientation reduces aerodynamic drag in the FA direction, while increasing drag in the SS direction, as shown in Figure 66.

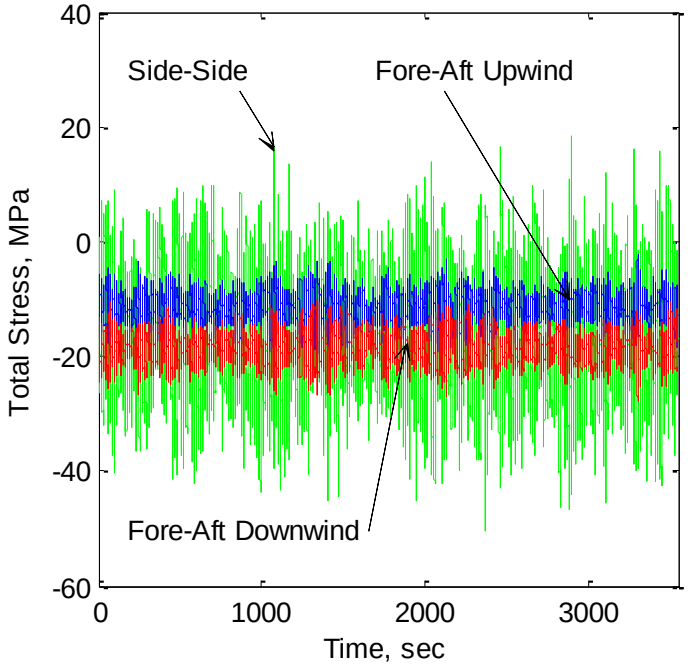

Figure 66: Total stress time histories of fore-aft upwind (180°), side-side (90°), and fore-aft downwind (0°) for a wind speed of 30 m/s, zero significant wave, and a damping ratio of 5%.

As wave height transitions from 0 m (as shown in Figure 66) to 8 m, the dominant source of stress shifts from aerodynamic loads in the SS direction to wave loading in the FA direction. This explains why the FA upwind circumferential orientation sees the most damage in higher wave height cases for parked and feathered conditions as shown in Table 36.

Damage accumulations based on the Palmgren-Miner rule for a 1-hour period are provided in Table 37, as calculated by averaging the 1-hour damage accumulation for the 6 distinct seeds at the circumferential orientation corresponding to maximum damage (see Table 36). The shading in the table indicates damage magnitude, as detailed in the scale

provided; the smallest damage values are shaded green, and the largest damage values are shaded red. This research is focused on the effects of damping on offshore wind turbine dynamics and fatigue, therefore the 1-hour damage values are generated for comparison purposes to evaluate the reduction in damage with increased damping. These damage values cannot be compared to a usage factor, η, as specified in the Recommended Practice C203 because the usage factor is specific to a 20 year lifespan of the turbine.

Table 37: Average damage accumulations based on the Palmgren-Miner rule for a 1-hour period in the location of maximum damage for several combinations of wind speed, significant wave height and damping ratio.

Least damage — Most damage

1.1e-11 | 3.4e-05 | 1.4e-04

		Damping Ratio, %				
		1	2	3	4	5
		Wind Speed 3 m/s (cut-in; operational)				
Significant Wave Height, m	0	2.0e-11	1.5e-11	1.7e-11	1.4e-11	1.1e-11
	2	5.2e-07	4.7e-07	4.3e-07	4.0e-07	3.7e-07
	4	3.4e-06	3.2e-06	3.0e-06	2.8e-06	2.7e-06
	6	1.3e-05	1.3e-05	1.2e-05	1.2e-05	1.2e-05
	8	3.6e-05	3.5e-05	3.3e-05	3.3e-05	3.2e-05
		Wind Speed 11.4 m/s (rated; operational)				
Significant Wave Height, m	0	9.4e-06	8.9e-06	8.5e-06	8.1e-06	7.8e-06
	2	2.2e-05	2.1e-05	2.0e-05	1.9e-05	1.9e-05
	4	4.5e-05	4.3e-05	4.1e-05	4.0e-05	3.9e-05
	6	8.0e-05	7.7e-05	7.4e-05	7.3e-05	7.1e-05
	8	1.4e-04	1.3e-04	1.3e-04	1.3e-04	1.3e-04
		Wind Speed 25 m/s (cut-out; operational)				
Significant Wave Height, m	0	2.0e-05	1.8e-05	1.6e-05	1.5e-05	1.4e-05
	2	3.1e-05	2.8e-05	2.6e-05	2.4e-05	2.3e-05
	4	5.1e-05	4.7e-05	4.5e-05	4.3e-05	4.1e-05
	6	8.1e-05	7.6e-05	7.2e-05	6.9e-05	6.6e-05
	8	1.3e-04	1.2e-04	1.1e-04	1.1e-04	1.1e-04

Significant Wave Height, m	Wind Speed 30 m/s (parked and feathered; operational)				
0	5.5e-06	4.5e-06	3.8e-06	3.3e-06	2.8e-06
2	5.6e-06	4.6e-06	3.9e-06	3.3e-06	2.8e-06
4	1.4e-05	8.6e-06	6.3e-06	5.1e-06	4.3e-06
6	3.7e-05	2.4e-05	2.0e-05	1.7e-05	1.5e-05
8	7.7e-05	5.5e-05	4.6e-05	4.1e-05	3.8e-05

When interpreting the results in Table 37, it is important to note that fatigue damage does not vary linearly with stress amplitude because the S-N curve is nonlinear, therefore the relationship between damping magnitude and damage is also nonlinear. The effect of increased damping on fatigue damage is evaluated by calculating the percent reduction in damage as compared to the damage at 1% damping ratio. The results are shown in Table 38. Bolded values highlight the maximum reductions for each wind speed case, and the darkness of the red and green shading indicates the magnitude of the damage and percent reductions, respectively.

Table 38: Percent reduction in average one-hour damage accumulation for several combinations of wind speed, significant wave height and damping ratio as compared to damage for a 1% damping ratio.

		Damping Ratio, %				
		1	2	3	4	5
		Damage	Percent Reduction			
		Wind Speed 3 m/s (cut-in; operational)				
Significant Wave Height, m	0	2.0e-11	**24%**	15%	**30%**	**47%**
	2	5.2e-07	11%	**18%**	24%	29%
	4	3.4e-06	8%	14%	18%	21%
	6	1.3e-05	4%	8%	12%	14%
	8	3.6e-05	3%	7%	10%	12%
		Wind Speed 11.4 m/s (rated; operational)				
Significant Wave Height, m	0	9.4e-06	**6%**	**10%**	**14%**	**17%**
	2	2.2e-05	5%	9%	12%	16%
	4	4.5e-05	4%	8%	10%	13%
	6	8.0e-05	3%	6%	8%	10%
	8	1.4e-04	2%	5%	6%	7%
		Wind Speed 25 m/s (cut-out; operational)				
Significant Wave Height, m	0	2.0e-05	**11%**	**20%**	**26%**	**31%**
	2	3.1e-05	10%	17%	23%	28%
	4	5.1e-05	7%	11%	16%	20%
	6	8.1e-05	6%	11%	15%	19%
	8	1.3e-04	5%	10%	13%	15%
		Wind Speed 30 m/s (parked and feathered; non-operational)				
Significant Wave Height, m	0	5.5e-06	18%	31%	40%	49%
	2	5.6e-06	18%	31%	41%	50%
	4	1.4e-05	**38%**	**55%**	**64%**	**69%**
	6	3.7e-05	33%	46%	54%	59%
	8	7.7e-05	28%	40%	46%	50%

Fatigue damage results parallel resultant mudline moment results in that the greatest effect of increased damping is seen in the parked and feathered cases (up to 69% reduction), and the least effect is seen the operating cases. This is again explained by the lack of

aerodynamic damping in the parked and feathered cases, which allows for foundation damping to account for a larger fraction of total system damping. Although similar numbers of stress cycles are acting on the turbine for each damping ratio input value, the magnitude of these stress cycles is reduced with increased damping, similar to the effects shown in Figure 61. This reduced cycle amplitude translates to a greater cycles-to-failure value, N_i, in the Palmgren-Miner eqn (3), which lowers the damage value. For all operational cases, the maximum reduction in damage occurs for significant wave heights of 0 and 2 m, conditions for which FA loading governs fatigue. This is in the same way due to the closeness in FA peak spectral wave loading frequency values to the turbine's natural and blade pass frequency values, as explained in previous sections. For non-operational cases with significant wave heights of 0 and 2 m, loading in the SS direction governs fatigue damage, as seen in Figure 66. Since wave loading is considered in the FA direction only, the loading in the SS direction is not sensitive to the frequency content of the waves, which are the main drive of dynamic effects. Therefore, in the SS direction, the increased damping does not have as much of an effect on the reduction in fatigue damage. In the case where the significant wave height is 4 m, the loading in the FA direction from the waves begins to dominate over the loading in the SS direction from wind turbulence, and this loading is influenced significantly by dynamic effects, and the results are therefore more sensitive to changes in damping. Compared to the cases where the significant wave height is equal to 6 and 8 m, the peak spectral frequency of the 4 m waves is closer to the natural frequency of the turbine (see Table 35), therefore it experiences the most sensitivity to changes in the damping ratio.

7.4.3 Damage contribution from stress amplitude percentiles

Given that increasing damping reduces load amplitude, it is important to analyze how damage is accumulated relative to stress amplitude. Because of the non-linearity of the S-N curve, where small changes in stress amplitude can translate to large changes in fatigue life, increased damping reduces fatigue damage by greater percentages than for the resultant moment. The importance of this relationship is illustrated by calculating the relative contributions to total damage associated with different stress amplitudes percentiles as shown in Table 39. These results are specific to the circumferential orientation calculated to have maximum damage for each combination of wind speed and significant wave height, and reflect average contributions across all wind speeds, wave heights, and damping ratios. The results in the table show how high amplitude stresses have a significantly greater contribution to damage than low amplitude stresses and further shows the significance of decreasing stress amplitude by increasing damping; a small decrease in stress amplitude can translate to a large decrease in damage and large increase in fatigue life.

Table 39: Average contribution of top percentiles of stress amplitude to accumulated fatigue damage for all combinations of wind speed, wave height and damping ratio.

Stress Amplitudes	Percent contribution to Total Damage	Ratio of Stress Amplitude Percentile to Damage Contribution
Top 10%	18%	1.8
Top 20%	30%	1.5
Top 30%	48%	1.6
Top 40%	66%	1.6
Top 50%	82%	1.6

7.5 Conclusion

Increased damping decreases both the resultant mudline moment and the accumulation of fatigue damage in every combination of wind, wave, and operating conditions considered here. Resultant moments experience reductions up to 4.2% in the operating cases and up to 17.3% in the parked and feathered cases with a damping ratio increase from 1%-5%. Fatigue damage accumulation experiences reductions up to 47% in the operating cases and up to 69% in the parked and feathered cases with a damping ratio increase from 1%-5%. Greater damage reduction was experienced in the parked and feathered cases due to the lack of aerodynamic damping from the spinning blades, which allowed for foundation damping to account for a greater portion of total system damping. The larger reductions in moment and damage for the parked and feathered cases are important for storm and hurricane events. The primary reason why the prediction of fatigue damage is more sensitive to damping ratio than the resultant moment is because fatigue damage is a function of fatigue life, and the relationship between stress (which is proportional to moment) and fatigue life is nonlinear.

Only co-directional wind and waves were considered, but a similar parameter study including misalignment may demonstrate foundation damping's role in demand reduction even more strongly; misaligned wave loading would not be reduced by aerodynamic damping, so increased foundation damping would have a greater effect on total system damping similarly to the parked and feathered conditions presented in this study. It is also recommended that this research be extended to turbine lifetime simulations so that the comparison of damage values to the usage factor is possible.

By taking into account foundation damping in offshore wind turbine design guidelines, design demands in terms of both ultimate and fatigue loads can be reduced. This concept is an important factor in attacking the high capital cost barrier that hinders development of offshore wind in the United States. If it can be properly incorporated into design, it's possible that more efficient and less expensive turbines can be constructed.

BIBLIOGRAPHY

[1] US Department of Energy, "2017 Offshore Wind Technologies Market Update," 2018.

[2] State of New Jersey, "Governor Murphy Signs Executive Order to Promote Offshore Wind Energy," *Office of the Governor*, 2018. [Online]. Available: https://nj.gov/governor/news/news/562018/approved/20180131a_eo.shtml.

[3] Commonwealth of Massachusetts, *House, No. 4568*, no. 4568. 2016, pp. 1–37.

[4] N. Ucci, "Governor's 1,000 by '20 Clean Energy Goal," *State of Rhode Island Office of Energy Resources*, 2018. [Online]. Available: http://www.energy.ri.gov/renewable-energy/governor-clean-energy-goal.php.

[5] New York State, "Governor Cuomo Announces Plan Directing the Procurement of Approximately 800 Megawatts of Offshore Wind to Jumpstart Industry," *Off. Gov.*, pp. 1–5, 2018.

[6] U.S. Department of Energy, "Wind Vision: A New Era for Wind Power in the United States," 2015.

[7] U.S. Department of Energy, "Offshore Wind Technologies Market Report," 2016.

[8] U.S. Department of Energy, "National Offshore Wind Strategy," 2016.

[9] W. Musial and B. Ram, "Large-Scale Offshore Wind Power in the United States: Assessment of Opportunities and Barriers," 2010.

[10] W. E. de Vries, B. Schmidt, D. Matha, and F. Vorpahl, "Support Structure Concepts for Deep Water Sites," 2016.

[11] WindEurope, "Floating Offshore Wind Vision Statement," 2017.

[12] American Petroleum Institute, "Recommended Practice for Design and Analysis of Stationkeeping Systems for Floating Structures," 2005.

[13] Vryhof, *Anchor manual: the guide to anchoring*. 2010.

[14] International Renewable Energy Agency, "Floating Foundations: A Game Changer for Offshore Wind Power," 2016.

[15] C. Mone, M. Hand, M. Bolinger, J. Rand, D. Heimiller, and J. Ho, "Cost of Wind Energy Review," 2015.

[16] M. Goldschmidt and M. Muskulus, "Coupled mooring systems for floating wind

farms," *Energy Procedia*, vol. 80, no. December, pp. 255–262, 2015.

[17] P. Connolly and M. Hall, "Comparison of pilot-scale floating offshore wind farms with shared moorings," *Ocean Eng.*, vol. 171, no. August 2018, pp. 172–180, 2019.

[18] M. Hall and P. Connolly, "Coupled Dynamics Modelling of a Floating Wind Farm With Shared Mooring Lines," in *ASME 2018 37th International Conference on Ocean, Offshore and Arctic Engineering*, 2018, vol. 10, pp. 10–11.

[19] M. Brommundt, L. Krause, K. Merz, and M. Muskulus, "Mooring system optimization for floating wind turbines using frequency domain analysis," *Energy Procedia*, vol. 24, no. January, pp. 289–296, 2012.

[20] I. Fylling and P. A. Berthelsen, "WINDOPT- An optimization tool for floating support structures for deep water wind turbines," *Proc. ASME Int. Conf. Ocean. Offshore Artic Eng. OMAE*, no. January 2011, pp. 1–10, 2011.

[21] A. C. Pillai, P. R. Thies, and L. Johanning, "Multi-Objective Optimization of Mooring Systems for Offshore Renewable Energy," in *EWTEC*, 2017, pp. 1–8.

[22] S. Ozmutlu, "Anchor and Mooring Line Cost Estimates." 2017.

[23] C. M. Fontana *et al.*, "Multiline anchor force dynamics in floating offshore wind turbines," *Wind Energy*, no. October 2017, pp. 1–14, 2018.

[24] C. M. Fontana *et al.*, "Spatial Wave Coherence in Multiline Anchor Systems for Floating Offshore Wind Turbines," in *International Conference on Structural Safety & Reliability*, 2017.

[25] C. M. Fontana *et al.*, "Multiline Anchors for the OC4 Semisubmersible Floating System," in *International Society of Offshore and Polar Engineers*, 2017, pp. 499–506.

[26] C. M. Fontana, S. R. Arwade, D. J. DeGroot, A. T. Myers, M. Landon, and C. Aubeny, "Efficient Multiline Anchor Systems for Floating Offshore Wind Turbines," in *OMAE*, 2016.

[27] S. T. Hallowell *et al.*, "System reliability of fl oating offshore wind farms with multiline anchors," *Ocean Eng.*, 2018.

[28] S. T. Hallowell *et al.*, "Reliability of mooring lines and shared anchors of floating offshore wind turbines," in *Proceedings of the International Offshore and Polar Engineering Conference*, 2017.

[29] B. D. Diaz *et al.*, "Multiline Anchors for Floating Offshore Wind Towers," in

OCEANS, 2016.

[30] M. Burns, M. L. Maynard, and W. G. Davids, “Centrifuge modelling of suction caissons under orthogonal double line loading,” *Int. Conf. Phys. Model. Geotech.*, pp. 465–471, 2014.

[31] J. Chung, “Physical Modeling of Suction Caissons Loaded in Two Orthogonal Directions for Efficient Mooring of Offshore Wind Platforms,” University of Maine, 2012.

[32] Carbon Trust, “Floating Offshore Wind: Market and Technology Review,” 2015.

[33] A. Robertson *et al.*, “Definition of the Semisubmersible Floating System for Phase II of OC4,” 2014.

[34] A. J. Coulling, A. J. Goupee, A. N. Robertson, J. M. Jonkman, and H. J. Dagher, “Validation of a FAST semi-submersible floating wind turbine numerical model with DeepCwind test data,” *J. Renew. Sustain. Energy*, vol. 5, no. 023116, 2013.

[35] J. M. Jonkman, S. Butterfield, W. Musial, and G. Scott, “Definition of a 5-MW reference wind turbine for offshore system development,” 2009.

[36] Statoil, “Hywind Scotland Pilot Park: Environmental Statement,” 2015.

[37] B. Jonkman and J. Jonkman, “FAST v8.16.00a-bjj,” 2016.

[38] J. M. Jonkman and M. L. Buhl Jr., “FAST User’s Guide,” 2005.

[39] M. Hall, “MoorDyn User’s Guide,” 2017.

[40] M. Hall and A. Goupee, “Validation of a lumped-mass mooring line model with DeepCwind semisubmersible model test data,” *Ocean Eng.*, vol. 104, pp. 590–603, 2015.

[41] American Bureau of Shipping, “Guide for Building and Classing Floating Offshore Wind Turbine Installations,” 2014.

[42] D. O. Thomas and G. E. Hearn, “Deepwater Mooring Line Dynamics With Emphasis on Seabed Interference Effects,” in *Offshore Technology Conference*, 1994.

[43] A. M. Viselli, A. J. Goupee, and H. J. Dagher, “Model Test of a 1:8 Scale Floating Wind Turbine Offshore in the Gulf of Maine,” *J. Offshore Mech. Arct. Eng.*, vol. 137, 2015.

[44] A. M. Viselli, A. J. Goupee, H. J. Dagher, and C. K. Allen, “Design and model

confirmation of the intermediate scale VolturnUS floating wind turbine subjected to its extreme design conditions offshore Maine," *Wind Energy*, vol. 19, no. September 2015, pp. 1161–1177, 2016.

[45] N. R. Pettigrew *et al.*, "The Gulf of Maine Ocean Observing System: Generic Lessons Learned in the First Seven Years of Operation (2001-2008)," *Mar. Technol. Soc. J.*, vol. 42, no. 3, pp. 91–102, 2008.

[46] University of Maine, "Mooring E0130: Central Maine Shelf, Gulf of Maine Moored Buoy Program, Physical Oceanography Group, School of Marine Sciences," 2013. [Online]. Available: http://gyre.umeoce.maine.edu/buoyhome.php.

[47] B. J. Jonkman and L. Kilcher, "TurbSim User's Guide: Version 1.06.00," *Natl. Renew. Energy Lab.*, 2012.

[48] J. M. Jonkman, A. N. Robertson, and G. J. Hayman, "HydroDyn User's Guide and Theory Manual," 2015.

[49] D. J. Renkema, "Validation of wind turbine wake models," Master's Thesis, Delft University of Technology, 2007.

[50] B. F. Xu, T. G. Wang, Y. Yuan, and J. F. Cao, "Unsteady aerodynamic analysis for offshore floating wind turbines under different wind conditions," vol. February, p. 373(2035), 2015.

[51] K. H. Andersen, "Cyclic soil parameters for offshore foundation design," in *International Symposium on Frontiers in Offshore Geotechnics*, 2015.

[52] A. L. Latifah and E. Van Groesen, "Coherence and Predictability of Extreme Events in Irregular Waves," *Nonlinear Process. Geophys.*, vol. 19, pp. 199–213, 2012.

[53] B. Alvise, B. Francesco, B. Filippo, C. Sandro, and S. Mauro, "Space-Time Extreme Wind Waves: Analysis and Prediction of Shape and Height," *Ocean Model.*, vol. 113, pp. 201–216, 2017.

[54] L. Shemer and A. Sergeeva, "An Experimental Study of Spatial Evolution of Statistical Parameters in a Unidirectional Narrow-Banded Random Wavefield," *Geophys. Res.*, vol. 114, no. January 2009, 2009.

[55] A. Sergeeva and A. Slunyaev, "Rogue waves , rogue events and extreme wave kinematics in spatio-temporal fields of simulated sea states," *Nat. Hazard Earth Syst. Sci.*, vol. 13, pp. 1759–1771, 2013.

[56] P. Balitsky, G. V. Fernandez, V. Stratigaki, and P. Troch, "Assessing the Impact

on Power Production of WEC array separation distance in a wave farm using one-way coupling of a BEM solver and a wave propagation model," in *12th European Wave and Tidal Energy Conference*, 2017, pp. 1–10.

[57] A. N. Robertson *et al.*, "Summary Of Conclusions And Recommendations Drawn From The Deepcwind Scaled Floating Offshore Wind System Test Campaign," in *ASME 2013 32nd International Conference on Ocean, Offshore and Arctic Engineering*, 2013, no. July.

[58] M. Hall, "MoorDyn User's Guide," 2017.

[59] DNV, "DNV-RP-C205 Environmental conditions and environmental loads," 2007.

[60] IEC 61400-3, "Design Requirements for Offshore Wind Turbines," 2009.

[61] A. J. Coulling, A. J. Goupee, A. N. Robertson, and J. M. Jonkman, "Importance of Second-Order Difference-Frequency Wave-Diffraction Forces in the Validation of a Fast Semi- Submersible Floating Wind Turbine Model," in *ASME 32nd International Conference on Ocean, Offshore and Artic Engineering*, 2013, no. June.

[62] P. Agarwal and L. Manuel, "Incorporating Irregular Nonlinear Waves in Coupled Simulation of Offshore Wind Turbines," in *48th AIAA Aerospace Sciences Meeting Including the New Horizons Forum and Aerospace Exposition*, 2010, no. January.

[63] T. Sarpkaya and M. Isaacson, *Mechanics of wave forces on offshore structures*. Van Nostrand Reinhold Co., 1981.

[64] A. Spyroudi, "Cost Modelling Analysis of Floating Wind Technologies: Assessing the Potential of TLPWIND," 2016.

[65] 4C Offshore, "Global Offshore Wind Farms Database," 2018. [Online]. Available: http://www.4coffshore.com/windfarms/. [Accessed: 11-Apr-2018].

[66] Statoil, "The development of Hywind Scotland Pilot Park," 2016. [Online]. Available: http://marine.gov.scot/datafiles/lot/hywind/Pre-application_consultation_report. [Accessed: 01-Jan-2017].

[67] London Array Operations and Maintenance Base, "London Array Operations and Maintenance."

[68] Nordsee One GmbH, "Nordee One Wind Farm Layout," 2017. [Online]. Available: http://www.nordseeone.com/wind-farm/wind-farm-layout.html.

[69] Ormonde Development, "Ormonde Project Environmental Impact Asssessment,"

2005.

[70] K. Peire, H. Nonneman, and E. Bosschem, “Gravity Base Foundations for the Thornton Bank Offshore Wind Farm,” *Terra Aqua*, no. 115, pp. 19–29, 2009.

[71] Statoil, “Hywind Pilot Park , the world’s first floating wind farm,” 2016. [Online]. Available: https://www.dovregroup.com/news/facts/hywind-pilot-park.html.

[72] Mathworks, “Curve Fitting Toolbox User’s Guide (R2018).” 2018.

[73] M. Masciola, “MAP++ Documentation,” 2015.

[74] A. Campanile, V. Piscopo, and A. Scamardella, “Mooring design and selection for floating offshore wind turbines on intermediate and deep water depths,” *Ocean Eng.*, vol. 148, no. July 2017, pp. 349–360, 2018.

[75] S. R. Neubecker and M. F. Randolph, “Profile and Frictional Capacity of Embedded Anchor Chains,” *Geotech. Eng.*, vol. 121, no. November, pp. 797–803, 1995.

[76] K. H. Andersen *et al.*, “Suction Anchors for Deepwater Applications,” in *1st International Symposium on Frontiers in Offshore Geotechnics*, 2005.

[77] N. D. . Barltrop, “Floating Structures: A Guide for Design and Analysis,” in *Volume II, Chapter 9*, The Centre for Marine and Petroleum Technology Publication., 1998.

[78] DNVGL, “DNVGL-ST-0126 Support structures for wind turbines,” 2016.

[79] DNV GL, “DNVGL-RP-C212 Offshore soil mechanics and geotechnical engineering,” 2017.

[80] A. N. Robertson and J. M. Jonkman, “Loads Analysis of Several Offshore Floating Wind Turbine Concepts,” in *International Society of Offshore and Polar Engineers 2011 Conference*, 2011, vol. 8, no. October, pp. 443–450.

[81] European Wind Energy Association, “Deep water: The next step for offshore wind energy,” 2013.

[82] W. Musial *et al.*, “2016 Offshore Wind Energy Resource Assessment for the United States,” 2016.

[83] M. T. J. Hall, “Mooring Line Modelling and Design Optimization of Floating Offshore Wind Turbines,” *Vasa*, 2010.

[84] C. Bjerkseter and A. Ågotnes, “Levelised cost of energy for offshore floating wind

turbine concepts," 2013.

[85] "Offshore Site Investigation and Geotechnics," in *Offshore Site Investigation and Geotechnics*, 2015, no. May.

[86] E. Simley and L. Y. Pao, "A Longitudinal Spatial Coherence Model for Wind Evolution based on Large-Eddy Simulation," in *American Control Conference*, 2015, pp. 3708–3714.

[87] Grofsmederij Nieuwkoop BV, *GN Rope Fittings Catalog*. 2015.

[88] IRENA, "Renewable Energy Technologies: Cost Analysis Series," 2012.

[89] a. T. Myers, S. R. Arwade, V. Valamanesh, S. Hallowell, and W. Carswell, "Strength, stiffness, resonance and the design of offshore wind turbine monopiles," *Eng. Struct.*, vol. 100, pp. 332–341, 2015.

[90] W. G. Versteijlen, a. V. Metrikine, H. J. S., and W. E. de Vries, "Estimation of the vibration decrement of an offshore wind turbine support structure caused by its interaction with soil," *Proc. EWEA Offshore Conf.*, 2011.

[91] M. Damgaard and J. Andersen, "Natural frequency and damping estimation of an offshore wind turbine structure," in *Proceedings of the Twenty-second (2012) International Offshore and Polar Engineering Conference*, 2012, vol. 4, pp. 300–307.

[92] W. Carswell *et al.*, "Foundation damping and the dynamics of offshore wind turbine monopiles," *Renew. Energy*, vol. 80, pp. 724–736, 2015.

[93] A. Macaskill and P. Mitchell, "Offshore wind-an overview," *Wiley Interdiscip. Rev. Energy Environ.*, vol. 2, no. 4, pp. 374–383, 2013.

[94] R. Shirzadeh, C. Devriendt, M. a. Bidakhvidi, and P. Guillaume, "Experimental and computational damping estimation of an offshore wind turbine on a monopile foundation," *J. Wind Eng. Ind. Aerodyn.*, vol. 120, pp. 96–106, 2013.

[95] P. K. Stansby, T. J. Stallard, and L. C. Devaney, "Breaking wave loads on monopiles for offshore wind turbines and estimation of extreme overturning moment," *IET Renew. Power Gener.*, vol. 7, no. 5, pp. 514–520, Sep. 2013.

[96] DNV, "DNV-OS-J101 Design of Offshore Wind Turbine Structures," 2013.

[97] DNV, "DNV-RP-C203 Fatigue design of offshore steel structures," 2010.

[98] J. F. Manwell, J. G. McGowan, and A. L. Rogers, *Wind Energy Explained: Theory, Design and Application*. 2002.

[99] V. Valamanesh and A. Myers, “Aerodynamic Damping and Seismic Response of Horizontal Axis Wind Turbine Towers,” *J. Struct. Eng.*, pp. 1–9, 2014.

[100] American Bureau of Shipping, “Design Standards for Offshore Wind Farms,” 2011.

[101] A. K. Chopra, *Dynamics of Structures*, 3rd ed., no. 1. 1992.